Year : 2021

Combining gravimetry, passive seismology and rock physical properties to constrain intra-crustal structures : the Ivrea Geophysical Body and the Gotthard Base Tunnel

Scarponi Matteo

UNIL | Université de Lausanne

Faculté des géosciences et de l'environnement
Institut des sciences de la Terre

Combining gravimetry, passive seismology and rock physical properties to constrain intra-crustal structures : the Ivrea Geophysical Body and the Gotthard Base Tunnel

Thèse de doctorat

présentée à la Faculté des géosciences et de l'environnement de l'Université de Lausanne par

Matteo Scarponi

titulaire d'un Master en physique de la Terre à l'Université de Bologna

Jury

Prof. György Hetényi	Directeur de thèse	Université de Lausanne
Prof. Klaus Holliger	Expert interne	Université de Lausanne
Prof. Claudia Piromallo	Experte externe	INGV Rome
Prof. Hans-Jürgen Götze	Expert externe	University of Kiel
Prof. Christian Kull	Président du jury	Université de Lausanne

Lausanne, 2021

UNIL | Université de Lausanne
Faculté des géosciences et de l'environnement
bâtiment Géopolis bureau 4631

IMPRIMATUR

Vu le rapport présenté par le jury d'examen, composé de

Président de la séance publique :	M. le Professeur Christian Kull
Président du colloque :	M. le Professeur Christian Kull
Directeur de thèse :	M. le Professeur György Hetényi
Expert interne :	M. le Professeur Klaus Holliger
Experte externe :	Mme la Professeure Claudia Piromallo
Expert externe :	M. le Professeur Hans-Jürgen Götze

Le Doyen de la Faculté des géosciences et de l'environnement autorise l'impression de la thèse de

Monsieur Matteo SCARPONI

Titulaire d'un

Laurea Magistrale In Fisica Del Sistema Terra

de l'Università degli Studi di Bologna

intitulée

Combining gravimetry, passive seismology and rock's physical properties to constrain intra-crustal structures: the Ivrea geophysical body and the Gotthard base tunnel

Lausanne, le 2 septembre 2021

Pour le Doyen de la Faculté des géosciences et de l'environnement

Professeur Christian Kull

Acknowledgements

Firstly and foremost, I would like to thank my supervisor Prof. György Hetényi for giving me the opportunity of pursuing this PhD and for trusting me. I want to thank him for being a guide and a mentor, whom I could discuss with in many occasions. This work would not have been possible without him.

Importantly, I would like to thank all the members of my thesis committee, for taking the time and the energies for reviewing my work, providing me with an occasion of personal and professional growth.

I would like to thank many colleagues who gave precious contributions, making this work possible. For this, I thank Jarka Plomerová, Stefano Solarino, Théo Berthet, Ludovic Baron and Urs Marti, both for the numerous scientific discussions and the experience they shared with me on the field, during the seismic and gravity campaigns. I want to thank Ludovic also for the efforts he made to set up all the gravity field instruments, together with Petr Jedlička, Josef Kotek and Ludek Vecsey for the seismic counterpart. I also thank Othmar Münthener, Alberto Zanetti, Mattia Pistone, Benoît Petri, Andrew Greenwood, Paola Manzotti, Luca Ziberna and Klaus Holliger for their great support and for the numerous fruitful discussions we had during these years around Ivrea (both geographically and scientifically).

I would like to thank many colleagues and friends I met during these years at the university, with whom I shared scientific discussions, fieldwork efforts, trips to conferences and many other memorable moments inside and outside the office. I thank Shiba, Leonardo, Matteo, Sergio, Celso, Konstantinos, Josh, Gelare and all the ones I met during these four years, to whom I am grateful.

I would like to thank all the friends I met during my time in Lausanne. They were many and it is impossible to list all of them here, but I am grateful to everyone. I thank Senan, Benoit and Pascal for making me feel part of a community of sport and friendship, and all the friends I met on the volleyball and beachvolley field such as Alberto, Andrea, Daniele and all the friends of the M3 Pully. I thank Ilias, Cecile, Pablo, Roxane, Margherita for all the aperos and time we shared. I thank all the friends with whom I am sharing a long beautiful series of cenette, for

Acknowledgements

Abstract

The structure of the Alpine orogen is complex, and many areas present an imaging gap between regional geophysical and local geological information. In the frame of this thesis, I have performed joint investigations, collecting new gravity and passive seismic data and combining them with surface geological observations and rock sample laboratory analysis, to provide higher-resolution images and models of an intra-crustal and a shallow Alpine structure. I targeted the Ivrea Geophysical Body (IGB) and the Gotthard Base Tunnel (GBT), as they provide ideal areas for testing the resolution limits of passive geophysical investigations and addressing pending structural questions as well. The IGB, considered as a sliver of Adriatic lower lithosphere, located at unusually shallow depths along the inner arc of the Western Alps, is associated with well-known density and seismic velocity anomalies. Aiming at refining the IGB structure and its relationship with the geological Ivrea-Verbano Zone (IVZ) outcropping at the surface, I collected 207 new relative gravity data and I installed 10 broadband seismic stations which operated for 27 months. In a first, 3D gravity study, I compiled a surface rock-density map and used it to define a density-corrected gravity anomaly named Niggli anomaly. Modelling the Niggli anomaly allowed to address more properly the IGB structure at depth, the latter being modelled as a 3D, single density-contrast interface beneath the entire IVZ. From this, I obtained $400 \pm 100 \ kg \cdot m^{-3}$ as optimal density contrast, and a ~ 20 km-wide protruding structure reaching as shallow as 1 ± 1 km depth below sea level. Petrological considerations allow to suggest ultramafic and mantle peridotite rocks as most likely components for the IGB. In a second, refined 2D study, the seismic data was also included to constrain the IGB model along the Val Sesia cross-section. A joint inversion was designed, exploiting seismic receiver functions and gravity anomalies, following an iterative inversion scheme to constrain the geometry and physical properties of the IGB. An optimal density contrast between 200 and $400 \ kg \cdot m^{-3}$ was obtained, with shallow segments 1-3 km depth below sea level, and in agreement with rock physical properties indicated by previous studies. For the final study, along the GBT, I acquired 80 new relative gravity data points at the surface and used 77 points measured in the tunnel to test and constrain the geological model established during tunnel construction. To this end, I developed an iterative scheme with fully 3D, density-dependent gravity terrain-adaptation corrections, to then consistently compare the observations with the synthetics from the 2D geology-based density model. Density data models for various lithologies were compiled from the SAPHYR rock physics database. The results show that in situ rock densities provide a better fit to the observed gravity data, and that the geological structure of GBT proposed earlier can be reasonably fit with surface and tunnel geophysical

Abstract

data.

Résumé

La structure de la chaîne alpine est complexe, et de nombreuses zones présentent une lacune de résolution entre les informations géophysiques à l'échelle régionale et les informations géologiques à l'échelle locale. Dans le cadre de cette thèse, j'ai récolté et analysé de nouvelles données gravimétriques et de sismique passive. Les données ont été analysées en combinaison avec des observations géologiques de surface et des analyses de laboratoire d'échantillons de roches, pour fournir des images et des modèles à plus haute résolution de la croûte terrestre alpine, à faible et moyenne profondeur. Je me suis concentré sur le Corps d'Ivrée (IGB) et sur le Tunnel de Base du Saint-Gothard (GBT), car ils représentent des zones idéales pour tester les limites de résolution de la géophysique passive, et pour répondre à des questions structurales d'intérêt. L'IGB, considéré comme une écaille de lithosphère inférieure de la plaque Adriatique situé à faible profondeur le long de l'arc intérieur des Alpes occidentales, est associé à des fortes anomalies de densité et de vitesse sismique. Dans le but d'affiner la structure de l'IGB et sa relation avec la zone géologique d'Ivrea-Verbano (IVZ), j'ai mesuré 207 nouveaux points gravimétriques, et j'ai installé 10 stations sismologiques large-bande pour 27 mois. Dans une première étude gravimétrique 3D, j'ai compilé une carte de densité de roches de surface, pour ensuite l'utiliser à définir une anomalie gravimétrique corrigée, nommé anomalie gravimétrique de Niggli. La modélisation de cette anomalie a permis de mieux décrire la structure de l'IGB en profondeur, cette dernière étant modélisée comme une interface de contraste de densité en 3D sous l'IVZ. A l'issue de cette modélisation, j'ai obtenu un contraste de densité optimal de $400 \pm 100 \ kg \cdot m^{-3}$, et une structure incrustée de ~ 20 km de large, à une profondeur aussi faible que 1 ± 1 km sous le niveau de la mer. Des considérations pétrologiques permettent de suggérer des roches ultra-mafiques et de péridotite du manteau comme les composantes les plus probables de l'IGB. Dans une deuxième étude en 2D, les données sismiques ont été incluses pour affiner le modèle de l'IGB le long du profil Val Sesia. Une inversion conjointe des données sismiques et gravimétriques a été conçue, suivant une approche itérative pour contraindre la géométrie et les propriétés physiques de l'IGB. Un contraste de densité optimal entre 200 et $400 \ kg \cdot m^{-3}$ a été obtenu, avec des segments à faible profondeur atteignant 1 à 3 km sous le niveau de la mer, et en accord avec les propriétés physiques des roches indiquées par des études précédentes. Pour l'étude finale, le long du GBT, j'ai collecté 80 nouveaux points gravimétriques, et utilisé 77 points mesurés dans le tunnel pour tester et contraindre le modèle géologique établi lors de la construction du tunnel. À cette fin, j'ai développé un schéma itératif avec des corrections et adaptations gravimétrique de terrain entièrement en 3D et en fonction de la densité, pour ensuite comparer de manière cohérente

Résumé

les observations avec les résultats provenant du modèle de densité 2D basé sur la géologie. Des modèles de densité pour diverses lithologies ont été compilés à partir du catalogue de physique de roches SAPHYR. Les résultats montrent que les densités de roche in situ expliquent mieux les données gravimétriques, et que la structure du modèle géologique du GBT proposé précédemment peut être raisonnablement décrite avec des données géophysique de surface et du tunnel.

Contents

Contents

List of Figures

List of Figures

List of Tables

1 Introduction

The Alps feature a remarkable level of complexity at a variety of spatial and time scales. This complexity ranges from the multi-stage dynamics of the tectonic plates which built the orogen, to almost-unique local features which relate to different steps of the formation history of the Alpine chain. In this chapter, a short introduction to the Alpine framework is given (section 1.1), with a subsequent focus on the main study area (section 1.2), the main targets for the works presented in this thesis (sections 1.3 and 1.4) and the overall scientific motivation (section 1.5).

1.1   The Alpine orogen

The European Alps represent a collisional orogenic belt, originated by the convergence of the European and the African plates. The Alps are characterised by an extremely complex structure, both at the surface and at depth, together with pronounced along-strike variations and an arcuate shape, connecting the Apennines to the Carpathians and the Dinarides. The Periadriatic Line, a former and major Alpine fault system, runs through the Alps in a West-East fashion and constitutes a main boundary between the main geographical and tectonic Alpine units (Schmid et al., 1989): the Western and Central Alps on one side and the Southern Alps on the other. Further to the East, the Eastern Alps constitute an additional element of complexity in the Alpine structure, presenting different tectonic settings (e.g., Schmid and Kissling, 2000; Schmid et al., 2008), and switches in the subduction polarity with respect to the Western part (e.g., Handy et al., 2015). This remarkable along-strike variation shows how complicated it is to describe the Alpine orogen as a unique and continuous system, which is also reflected in its Alpine foreland, ranging from the Jura Mountains in the West to the Pannonian Basin in the East (Figure 1.1).
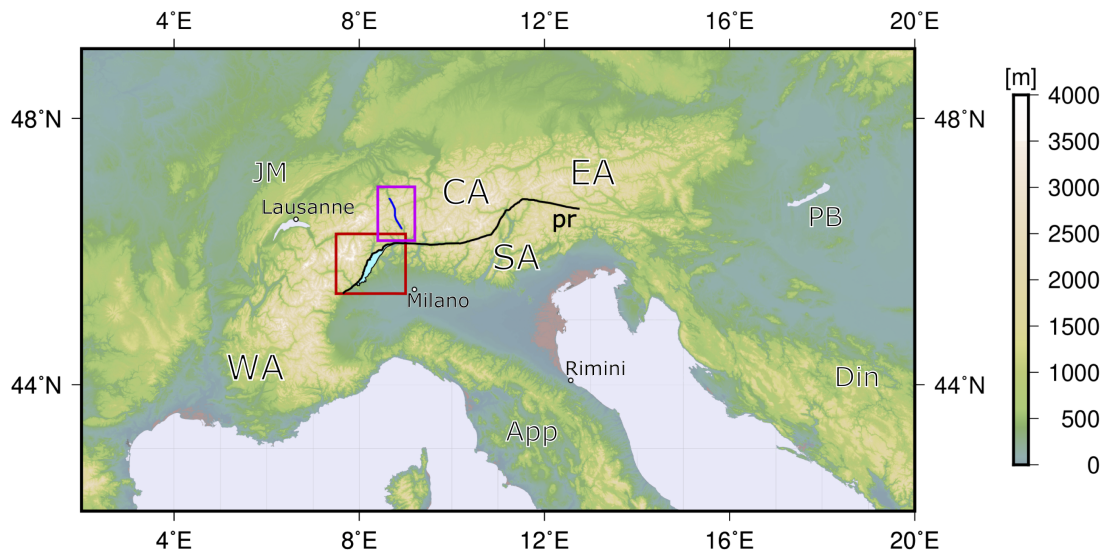
Figure 1.1 – A topographic view of the Alpine domain and the associated main geographical domains. The black line indicates the surface expression of the former major Periadriatic fault system, representing the western and northern boundary of the Southern Alps. The red square indicates the main area of interest for the studies discussed in chapter 3 and chapter 4 of this thesis, focusing on the Ivrea-Verbano Zone (cyan shape in figure). The magenta square indicates the main area of interest for the study discussed in chapter 5, focusing on the Gotthard Base Tunnel (blue line in figure). "WA" indicates Western Alps, "CA" Central Alps, "SA" Southern Alps, "EA" Eastern Alps, "pr" Periadriatic Line, "App" Apennines, "Din" Dinarides, "JM" Jura Mountains, "PB" Pannonian Basin.

The current tectonic and geological complexities are due to both orogen formation mechanisms and pre-Alpine events as well, which contributed to the formation of important inherited structures and rock complexes. Relative to the orogen formation, the Europe-Africa plate convergence became of primary importance in the late Cretaceus (85 Ma), involving the Adriatic micro-plate (or simply Adria) as one of the key actors in the orogenic collision, with the Periadriatic fault system marking the boundary between the European margin and the indenting African-Adriatic plate system. The Cretaceus paleogeographic setting presented Adria separated from the European margin by the so-called Alpine Tethys (e.g., Stampfli et al., 2001): a former ocean, formed by the Piemont-Liguria and Valais sections, which opened between the late-Triassic and the Jurassic Mesozoic times (200-175 Ma). The Alpine Tethys subsequently subducted (e.g., Handy et al., 2010), leaving nappe stacks exposed along the south-western European margin (Figure 1.2). With Adria thrusting against Europe along a N-NW direction, the European plate featured a southward subduction (e.g., Ceriani et al., 2001; Lippitsch et al., 2003), and in the late Cenozoic (35 Ma to present) the Western Alpine orogen developed both the elevation and the peculiar arcuate shape (e.g., Handy et al., 2015). In the most recent phases of the orogenic process, i.e. in the post-20 Ma to present, the Adriatic plate has been associated with a counter-clockwise rotation roughly around the location of Ivrea,

indenting the Eastern Alps from the South, thereby favouring there the conditions for some of the strongest earthquakes in the European history (e.g., Le Breton et al., 2017; Handy et al., 2015).

Prior to the Jurassic rifting and the Cretaceus convergence, the continental crust had been already significantly modified by pre-Alpine late Carboniferous and Permian magmatic events. In fact, following the collapse of the Variscan orogeny (300 Ma), a previously-thickenned continental crust underwent a progressive thinning, characterised by extensional tectonics and an increase of the continental geotherm (e.g., Petri et al., 2017). This extensional regime featured an intense magmatic activity (Quick et al., 2009), with magmatic Moho underplating and crustal intrusion of mantle-derived mafic and ultramafic magmas. These magmatic events lead to the production of crustal melts and high-temperature (HT) metamorphism, which has been well documented in the Southern Alps (e.g., Petri et al., 2017). The exact temporal and spatial relationship between tectonic extension, magmatism and metamorphism associated with the so-called "Permian event" are still debated. However, the continental crust underwent a major structural and compositional re-organisation during this time; the crust was subsequently brought close to (or even exhumed at) the surface during the Mesozoic rifting (e.g., Petri et al., 2019) and later involved in the orogenic collision between the European margin and the Adriatic plate. Significant portions of the Permian-derived crustal structures and mafic complexes are today exposed at the surface in the Ivrea-Verbano zone (IVZ, Figure 1.2, section 1.2), which is the focus study area for part the works presented in this thesis (chapters 3 and 4), and constitutes an almost-unique open-air laboratory for the study of the deep continental crust (e.g., Pistone et al., 2020).

1.2 The Ivrea-Verbano zone

The Ivrea-Verbano zone represents one of the major geological and tectonic complexes of the Southern Alps. The IVZ is located at the western end of the Southern Alps, bounded to the South by the adjacent Serie-dei-Laghi complex and the subsequent Po Plain, and to the North by the Insubric Line (IL, i.e. the western end of the Periadriatic Line). The IL is a mainly vertical to sub-vertical feature, separating the IVZ from the north-western Penninic nappes area (e.g., Berger et al., 2012; Schmid et al., 1989; Schmid et al., 1987), and corresponds to the western continuation of the Periadriatic fault system. The IVZ has been mapped and investigated by many authors (e.g., Schmid et al., 2004; Brack et al., 2010), and it exposes at its surface lower to middle crustal composition rocks, together with mafic complexes of Permian magmatic origin (Petri et al., 2019; Figure 1.2). The exposed crustal structure was most likely exhumed and horizontally tilted during the Jurassic rifting and the subsequent Alpine collision (Siegesmund et al., 2008). The IVZ emplacement (i.e. exhumation and final steepening) during the Alpine orogeny did not significantly alter its own structure (Zingg et al., 1990), and the IVZ is today identified as a nearly-complete cross-section of the continental crust (e.g., Fountain, 1976; Quick et al., 1995). The signature of pre-Alpine inherited crustal structures from the Permian extension and the Jurassic rifting is visible at the IVZ surface, with two main recorded features:

the Cossato-Mergozzo-Brissago (CMB) line and the Pogallo line (PL).

The CMB represents a high-temperature shear-zone which was active during the Permian magmatism (e.g. Snoke et al., 1999), while the PL is a pre-Alpine fault, active during Mesozoic extensional regime (e.g., Zingg, 1983). A number of laboratory analyses have been carried on IVZ outcrop samples, showing physical rock properties, such as high densities (up to 3300 $kg \cdot m^{-3}$) and seismic velocities (v_P up to 7-8 $km \cdot s^{-1}$), which are typical of the upper mantle and lower continental crust (e.g., Khazanehdari et al., 2000; Zappone and Kissling, 2021).

A significant geophysical interest is devoted to the crustal structure beneath the Ivrea-Verbano zone, which is associated with well-known and much longer gravity and seismic anomalies, extending along the whole inner arc of the Western Alps, and bounded to the North-West by the IL. We refer to this geophysical anomaly as the Ivrea geophysical body (IGB, section 1.3). As it will be further explained in the subsequent paragraphs, fundamental questions on the structural relationship between the IGB and the IVZ are pending and require a new series of intra-crustal high-resolution geophysical investigations to be undertaken, primarily to bridge the gap in the spatial scales between the geology observed at the surface, and the source of the geophysical anomalies at depth.
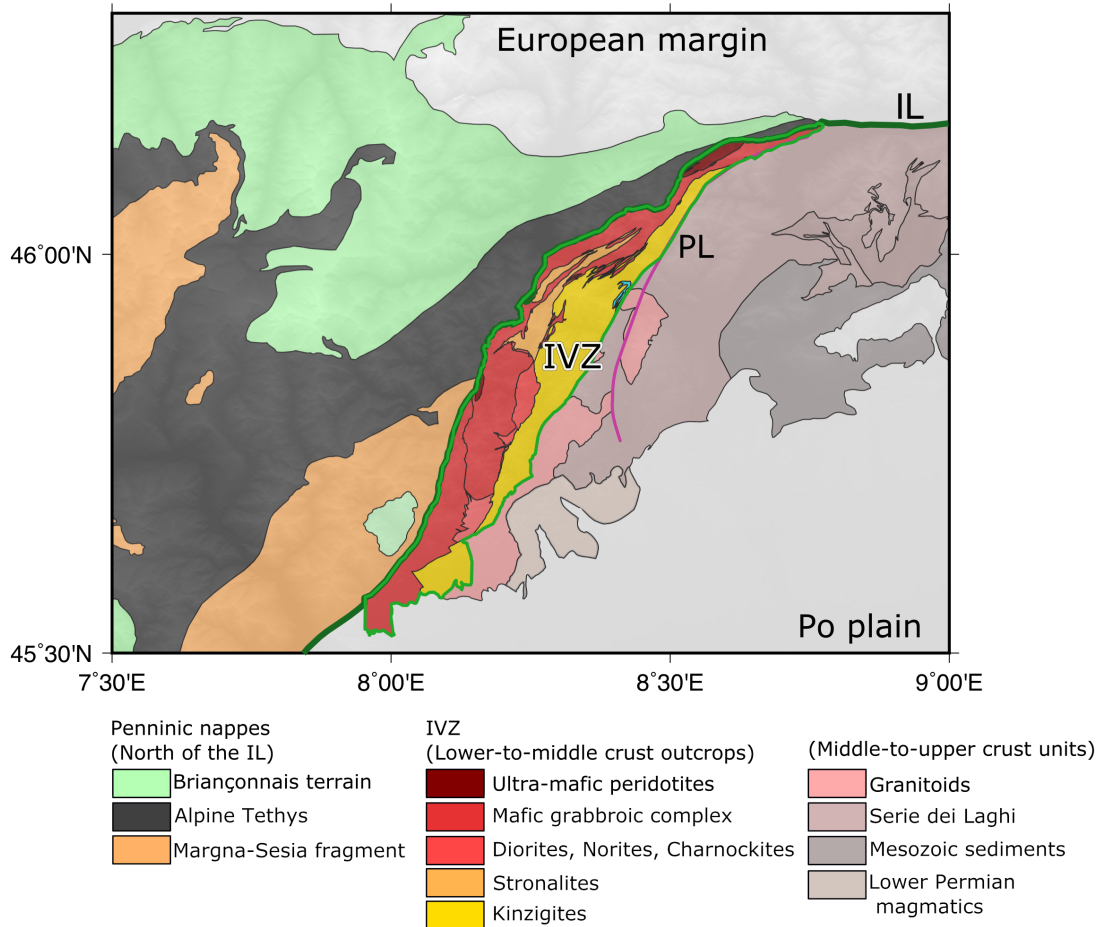
Figure 1.2 – A tectonic map for the Ivrea-Verbano zone (IVZ, light green contour) and the surrounding regions, modified from Schmid et al. (2004); Brack et al. (2010) and Petri et al. (2019). The main geological units of interest are pointed out in the legend, together with the main tectonic surface features as drawn in figure. "IL" (dark green line) represents the Insubric Line, i.e. the western-most segment of the Periadriatic Line, separating the IVZ from the Penninic and Austro-alpine nappes to the North-West. "PL" (purple line) represents the Pogallo Line, i.e. the surface expression of an inherited crustal architecture associated with the Jurassic rifting.

1.3 Ivrea Geophysical Body

The Ivrea geophysical body represents a well-known and pronounced gravity and seismic anomaly, associated with the crustal structure along the inner arc of the Western Alps. The IGB is nowadays regarded as a sliver of Adriatic lower lithosphere (e.g., Schmid et al., 2017), emplaced at anomalously shallow depths in the Alpine collision. The IGB has been the subject of a long history of petrological, geophysical and geological investigations, which addressed the crustal structure of the Western Alps at various spatial and time scales. While a number of gravity maps were produced by various authors, with a general agreement on the main features

of the IGB gravity high (e.g., Vecchia, 1968; Kissling et al., 1984; Rey et al., 1990; Marson et al., 1994), the work of Niggli (1946) represents the first historical contribution on the correlation between the IGB positive gravity anomaly and the lower crustal outcrops exposed in the IVZ. In his work, a NNW-SSE gravity profile across the Alps shows the IGB positive gravity anomaly in sharp contrast with respect to the negative background, characterizing the thickened Alpine crust.

The IGB was first imaged in the late '60s, by means of refraction seismics (Berckhemer, 1968). This type of active seismic investigation makes use of refracted seismic waves, usually generated by artificial sources (e.g., explosions, vibrating mechanical sources), which can travel at the interface between two layers presenting a seismic velocity contrast. Information on the layer thickness and the velocity profile are obtained, with a sensitivity for increasing velocities with depth. By combining active seismics and gravity anomaly data Berckhemer provided a first 2D model of the IGB, along a West-East profile crossing the IVZ, which became rather iconic and often referred to as the "Bird's head" in the literature (Figure 1.3).
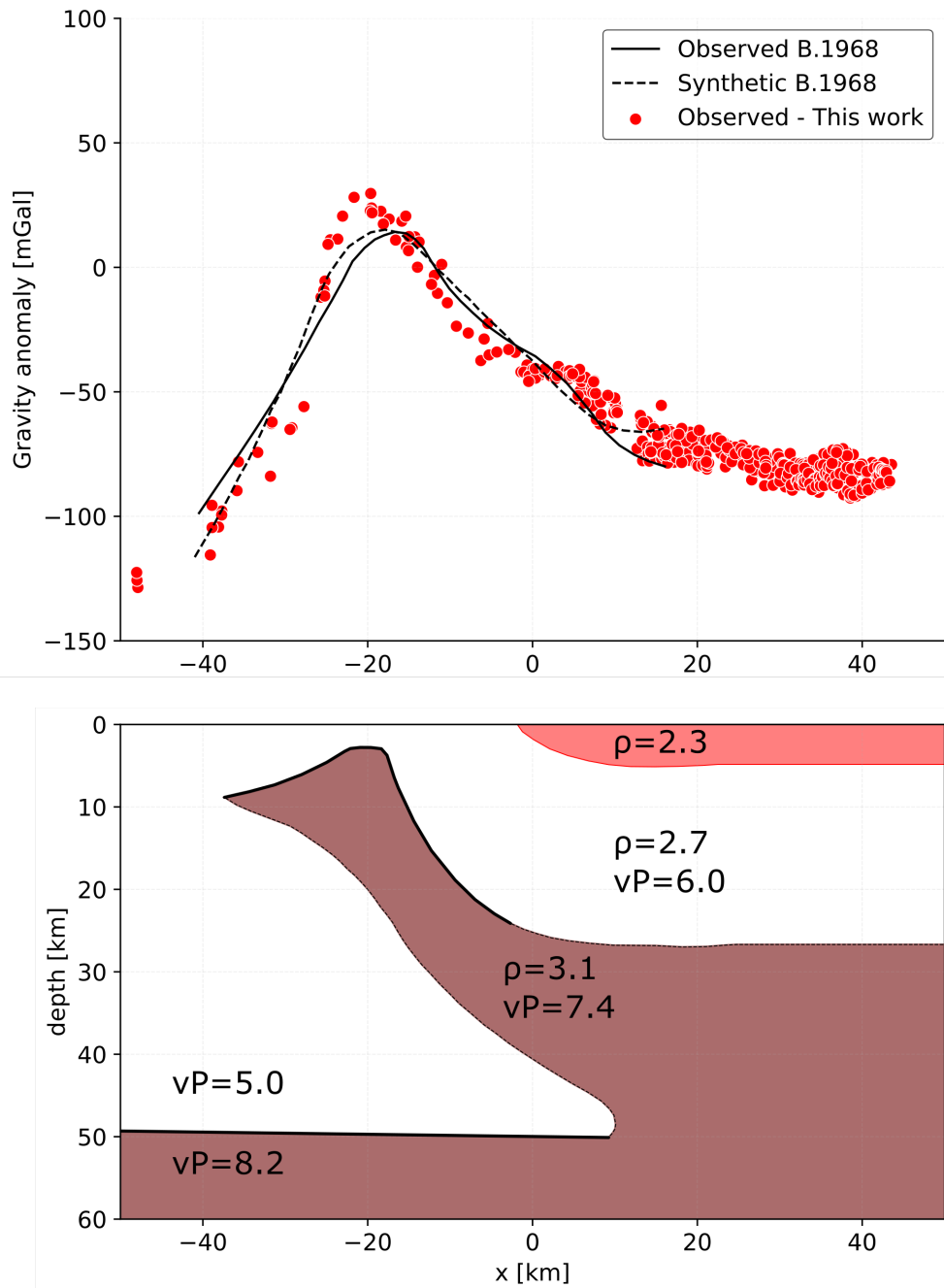
Figure 1.3 – The first refraction seismics and gravity model for the IGB by Berckhemer (1968). (a) The observed and synthetic gravity anomaly data along the Ivrea-Verbano zone profile from the work of Berckhemer (1968), digitised and compared to the gravity anomaly measured in the frame of this thesis. While Berckhemer's model captures well the regional field, further local variations are revealed by the new surveys. (b) The iconic model proposed by Berckhemer to fit gravity and seismic observations, which is often referred to as the "Bird's head" in the literature. In figure, the density ρ is indicated in $g \cdot cm^{-3}$ and the v_P seismic velocity in $km \cdot s^{-1}$.

Berckhemer's model should be considered as a brilliant interpretation of some of the first refraction seismic data available at the time, which presented non-negligible noise in the shallowest model sections and provided structural information averaged over long distances (the shooting point was Lac Nègre at the Italo-French border, ca. 200 km to the S-SW with respect to the IVZ). Although we now know that the crustal structure is more complex than a 2D model, it is Berckhemer's general idea which paved the way for a long series of geophysical investigations.

Further refraction seismic data was collected in the scope of the ALP75 active seismic experiment (Miller, 1976). The analysis of the data suggested high values of v_P seismic velocity in the area of Ivrea (above 7 $km \cdot s^{-1}$ between 5 and 20 km depth), with strong horizontal variations in the v_P-depth profile with respect to the neighbouring regions of the Western and Southern Alps (Ansorge et al., 1979).

A first 3D gravity model of the IGB was subsequently provided by Kissling et al. (1984). The model is based on gravity data collected across the IVZ, modelled along three linear profiles perpendicular to the IVZ main strike, and it presents a homogenous density contrast of 350 $kg \cdot m^{-3}$, with a steep eastward-dipping structure. A number of IGB gravity models were further produced, featuring block-assembled units with varying density contrasts (e.g., Bürki, 1990) and combining gravity data with reflection seismics data, acquired in the frame of the ECORS-CROP active seismic experiment (e.g., Bayer et al., 1989; Rey et al., 1990; Thouvenot et al., 1990). Despite the increasing amount of information on the Alpine crustal structure, mainly provided by active seismic experiments, none of the above-mentioned contributions could be considered as conclusive on the IGB structure and physical characteristics, mainly because of the technical limitations of controlled-source seismology in imaging such a complex structure (Kissling, 1993), and also because of the along-strike structural variability. Further crustal P- and S-wave seismic velocity models were later developed, based on the installation of a temporary short-period seismic array across the IVZ (De Franco et al., 1997). The analysis of local earthquake events pointed towards a uniform upper crust and a layered an reflective lower crust, reaching as shallow as between 15 and 8 km in the northern and southern areas of the IVZ, with a minumum depth of 5 km in the northern part. The reflectivity of an "Ivrea-type" lower crust has been also investigated in statistical terms, by analysing the synthetic seismic response of stochastic models, built based on the exposed geological and petrological structures at the IVZ surface (e.g., Holliger et al., 1993; Holliger et al., 1994). The spatial and compositional heterogeneities observed at the IVZ surface agree with a commonly observed reflective lower continental crust, and advocate for a strong influence of the bulk and metamorphic rocks composition on the observed seismic response.

Major advancements in the investigation of the Alpine crustal structure were introduced by seismic tomography, which is a passive seismic investigation technique, based on the propagation of waves generated by either teleseismic or local earthquake events (LET: local earthquake tomography), or both in certain applications. The analysis of seismic traveltimes is then used to constrain the bulk seismic velocity anomaly distribution within the target volume (e.g., Rawlinson et al., 2010). There has been a number of important tomographic applications, which provided images of both shallow and deep features related to the Alpine

structure (e.g., Lippitsch et al., 2003; Piromallo and Faccenna, 2004; Kissling et al., 2006). Related to the IVZ shallow crustal structure, high v_P seismic anomalies associated with the IGB have been detected and investigated, showing typical lower-crustal and mantle-like seismic velocities (above 7 $km \cdot s^{-1}$) at upper crustal depths (e.g., Diehl et al., 2009; Solarino et al., 2018). This, together with other passive seismic imaging techniques such as ambient noise tomography (e.g., Lu et al., 2018), allowed a comprehensive understanding of the IGB structure at a regional scale (Figure 1.4). Nevertheless, resolution gaps still exist and do not allow to capture the structural details and the relationship between the shallow-reaching IGB and the IVZ subsurface: Diehl et al. (2009) provides a v_P model on a 25x25x15 km grid, while Solarino et al. (2018) locally at a higher resolution on a 15x15x10 km grid. This gap is not expected to be filled by the AlpArray Seismic Network (Hetényi et al., 2018), as the station spacing and the occurrence of local events are too sparse to allow higher-resolution LET studies (on the order of kilometers) to be carried out.
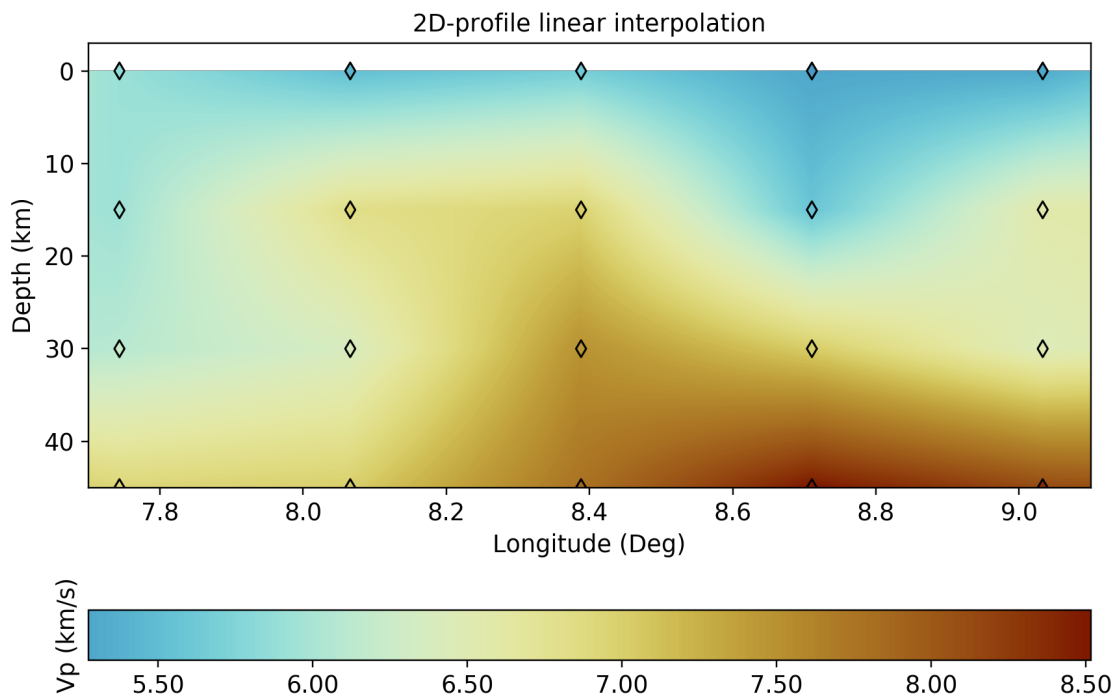
Figure 1.4 – A cross-section of the v_P seismic velocity model from Diehl et al. (2009), along a linear West-East profile across the IVZ along Val Sesia, showing the high seismic velocity anomaly associated with the IGB. The v_P is resolved on a grid of 25 km x 25 km x 15 km spatial resolution. The diamonds in the figure represent the original grid points, the velocity structure in the background is obtained by linear interpolation.

1.4   The Gotthard Base Tunnel

The Gotthard Base Tunnel (GBT) is a 57 km long dual-tube railway tunnel, which was constructed in the Central Alps in Switzerland between 2000 and 2011. The GBT is the longest railway tunnel for public transportation in Europe and it extends mainly along the North-South direction (at ca. 8.77° E longitude and between ca. 47.37° N and 46.84° N latitude), locally as much as 2500 m below the surface in the areas of higher topography. The two tunnel ends are located in Bodio (Ticino) and Erstfeld (Uri) in the South and in the North respectively, and the local topography presents a number of glacial U-shaped valleys extending in the North-South direction. While the tunnel itself remains mainly at 500 m above sea level along its own length, the topography reaches up to 3000 m height above sea level. The tunnel crosses several important tectonic units which are, from North to South, the Aar Massif, the Tavetsch Massif, the Urseren-Garvena Zone, the Gotthard massif and the Penninic Gneiss zone. Recent tectonic reconstructions (e.g., Schmid et al., 2017) show that these massives mainly belong to the European continental crust, with the Alpine deformation having occured in post-collisional times (35-30 Ma, Schmid et al., 1996).

A rich amount of geotechnical data was collected during both the construction and the subsequent operation phases, for monitoring and risk-mitigation purposes (e.g., Löw et al., 2015). As a consequence, we can benefit from a unprecedented sub-km-scale view of the geological structure of the very shallow crust, obtained by combining both surface geological mapping and geological information obtained from inside the tunnel itself (Figure 1.5).

The tunnel crosses several geological units, with their strikes mainly along the WSW-ENE direction and cutting the tunnel in an almost perpendicular fashion. The northern section presents steep southward-dipping structures, while the southern section presents steep northward-dipping structures. During the tunnel construction, relative gravity data was measured by SwissTopo (Swiss Federal Office of Topography) along the tunnel tracks with an average spacing of the order of 800 m. This scenario, together with the geological and rock-density data collected along the tunnel, constitutes an ideal framework for testing the current geological knowledge of the shallow crust, by means of gravity data modelling. As the existing gravity datasets at the surface where not spatially dense enough for this purpose, and as will be further explained in chapter 5, we acquired new gravity data at the surface along the tunnel tracks, mimicking the tunnel gravity data distribution. A novel algorithm for 3D gravity data processing and 2D crustal density modelling is discussed in the goal of testing, validating or adjusting the geological model presented in Figure 1.5.
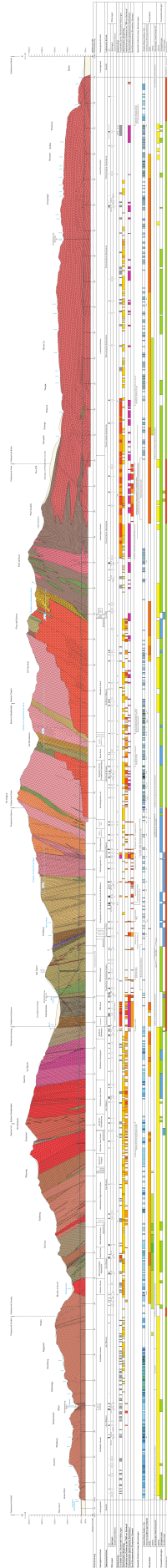
Figure 1.5 – A cross-section of the shallow crustal geological structure, along the Gotthard Base Tunnel (Guntli et al., 2016). The geological units have been obtained by a combination of the surface geological mapping and the data collected inside the tunnel itself, at the time of its construction, as well as local geophysical investigations (e.g., seismics, drilling). The tunnel extends mainly along the North-South direction in the Central Alps in Switzerland. A legible, segmented version of this figure is shown in chapter 5.

11

1.5 Motivation

The works presented and discussed in this thesis have been driven by a common motivation: to bring the geophysical investigations of the Earth crustal structure closer to the scales of the surface geological knowledge, with the purpose of closing the km-scale resolution gaps. This affected most of the past geophysical gravity and seismic investigations in many areas of the Alpine domain. As an alternative to expensive active source seismic investigations, the purpose of this work is to extend the application of passive methods towards imaging smaller scale structures, by systematically improving the data coverage in the study areas, and by combining the geophysical data with complementary geological observations and information from rock sample laboratory analysis.

New geophysical data and new processing techniques are required to address structural unknowns at crustal and intra-crustal levels. This is particularly true for the case of the Ivrea-Verbano zone and the Ivrea Geophysical Body: two outstanding features of the Alpine chain, whose structural relationship is still a matter of debate in many senses. In the subsequent chapters, the new gravity and seismic data collected for these purposes are presented, with a particular emphasis on how a targeted data coverage across key locations can help obtaining a refined image of the Earth crust. Similarly, the Gotthard Base Tunnel offers a suitable playground for testing an observation-derived geological model using gravity anomaly data, which has been collected, processed and exploited to test and improve the associated intra-crustal density model. The investigation of both the IGB and the GBT required the development of new processing and analysing tools, such as the definition and the subsequent 3D modelling of the so-called "Niggli" anomaly (chapter 3), the joint inversion of migrated seismic receiver function (RF) images with gravity data (chapter 4), and a novel iterative 3D density-dependent gravity terrain correction for 2D gravity data and density modelling (chapter 5). To optimize the success and the effectiveness of these studies, I had the opportunity to design the field experiments leading to the seismic and gravity data collection, and to perform the full sequence of research steps, ranging from planning to results and interpretation. Furthermore, the integration of available geological data and rock property laboratory analysis provided by previous studies, allowed to interpret and sharpen the results obtained by these passive geophysical investigations.

This research also developed in close collaboration with the DIVE project (Drilling the Ivrea-Verbano zonE, Pistone et al., 2017). DIVE is a continental scientific drilling project, with the aim of, among others, sampling and investigating the physical and chemical properties of continental crust in the Ivrea-Verbano zone. In this framework, several site surveys and local active seismic investigations (e.g., Greenwood et al., 2018) developed in parallel to this thesis, with the common purpose of resolving regional and local structures at higher-resolution.

2 Data and Methods

The knowledge on the Earth's internal structure is often obtained in the form of solution to an inverse problem. We could formulate a very simple *toy* problem as follows:

$$f(x) = y \qquad (2.1)$$

with y representing the observable data (e.g. seismic wave arrivals or local gravity acceleration), x representing the parameters defining an Earth model and its properties, and f representing the forward problem, i.e. our description of the real-world physical laws which relate the model parameters x to the observable data y. Unfortunately, it is rarely possible to directly access and measure the parameters x, which may describe some interesting geophysical properties of the Earth (e.g. the density or the seismic velocity of certain rock masses buried at depth). However, an inverse problem can be formulated to estimate and constrain the parameters x, by making use of the observations y. While inverse problems can be tackled through a variety of different approaches, depending on - among others - the investigation purposes and the properties of f (e.g. f may even correspond to a series of numerical calculations with no explicit formulation), real data acquisition, data processing and modelling, as well as uncertainty estimation, are key steps in any geophysical investigation probing the Earth system. In this chapter, I present the gravity and seismic data collected in the frame of this thesis (sections 2.1 and 2.3), together with the relevant forward modelling approaches I adopted (sections 2.2 and 2.4). These same topics, together with the formulation and solution of the associated inverse problems, are further discussed and developed in chapters 3 and 4. Furthermore, chapter 5 also treats data acquisition and a set of tailored processing steps to asses the validity of an existing model.

2.1 Introduction to gravity surveys

In the frame of this thesis, I collected new gravity data across the Ivrea-Verbano zone (IVZ) and along the Gotthard base tunnel (GBT), using a Scintrex CG-5 relative gravimeter (Figure 2.1). This type of gravity sensor measures the relative gravity difference between the current measuring station and previous ones. Such a device can be used to generate a network of gravity measurements, with constrained relative differences, which has to be tied to a known reference point to obtain absolute gravity values.

The CG-5 gravimeter is usually associated with an instrumental drift, which increases in time and can potentially affect all the measurement results. To minimise the effect of the drift and subsequently correct for it, all the gravity measurements are organised into loops, where the first and the last measurements of the same loop are always taken at the same location. Alternatively, a series of gravity measurements can also start and finish at two different locations, whose gravity difference is already known. This fundamental practice eventually determines a significant portion of a gravity campaign planning, and allows to estimate the instrument's daily drift for the gravity data correction, under the assumption of a linear drift behaviour (e.g. over one working day).

As the gravimeter measures the vertical component of the local gravity field, a correct estimation of the measurement point elevation is of compelling importance for the subsequent gravity data processing and modelling. In fact, one meter vertical displacement, in free-air conditions, corresponds to a ca. 0.3086 mGal gravity change, (where 1 Gal = 0.01 $m \cdot s^{-2}$). At each gravity measurement site, a GNSS GR-5 Topcon antenna was used to record satellite signals, which are subsequently processed to obtain a precise estimate of the point elevation. The elevation uncertainty can range from ca. 1 m to 1 cm depending on the acquisition and processing techniques, with 1 m as a upper limit for our application, for whose processing we used the free PPP service (Precise Point Positioning https://webapp.geod.nrcan.gc.ca/geod/tools-outils/ppp.php). In fact, intra-crustal anomalies of geophysical interest can generate a gravity anomaly ranging from few mGal (e.g. for a shallow km-scale body with a few hundreds $kg \cdot m^{-3}$ density contrast) to 100 mGal (e.g. for the regional-scale gravity anomaly associated with the Ivrea-geophysical body).

Raw gravity data has to be further processed to obtain absolute gravity values, for which I adapted and used the software GRAVPROCESS (Cattin et al., 2015). In addition to this, I computed gravity data products which take into account the effect of surface topography and provide information on the Earth crustal structure (e.g., the Bouguer gravity anomaly), and I designed and applied a density-dependent gravity correction to integrate the surface geological observations into the gravity investigation and modelling of the Ivrea geophysical body. All these steps are carefully presented and discussed in chapter 3.

I acquired the new gravity data analysed in this thesis, through a series of six gravity measurements campaigns, which took place from September 2017 to March 2021, and which required more than two months of field-only activity. Three main campaigns in the Ivrea-Verbano zone (two weeks in September 2017, two weeks in June 2018 and a further week in September 2019) lead to the collection of 207 new gravity points, which have been analysed in the works

presented in chapters 3 and 4, and have been included in the first pan-Alpine surface gravity database published recently (Zahorec et al., 2021). A further campaign in March 2021, allowed the collection of additional gravity data across the Balmuccia Peridotite outcrop in the Ivrea-Verbano zone, whose data has not been processed yet. Other two campaigns of ca. two weeks each (June 2020 and September 2020) allowed to the collection of 80 new gravity data points along the Gotthard Base Tunnel tracks, which have been analysed in the work presented in chapter 5.

Figure 2.1 – A picture taken during a gravity field campaign. It shows the typical set up for a gravity measurement. On the left, the GNSS antenna recording satellite signals, for the a posteriori estimation of the point elevation. The antenna is usually placed as high as possible with respect to ground, to avoid the surrounding obstacles. On the right, the relative gravimeter on a tripod, used to level the instrument and usually sitting on stable ground, to avoid tilting and perturbations during the measurement.

2.2 Gravity data processing and forward modelling

Gravitational attraction is described as a potential field quantity, which acts at any point of the space, as a function of the location and mass of the existing sources. Therefore, solving a forward gravity problem means modelling the gravity effect caused by massive bodies or, in general, a given density distribution (Figure 2.2).
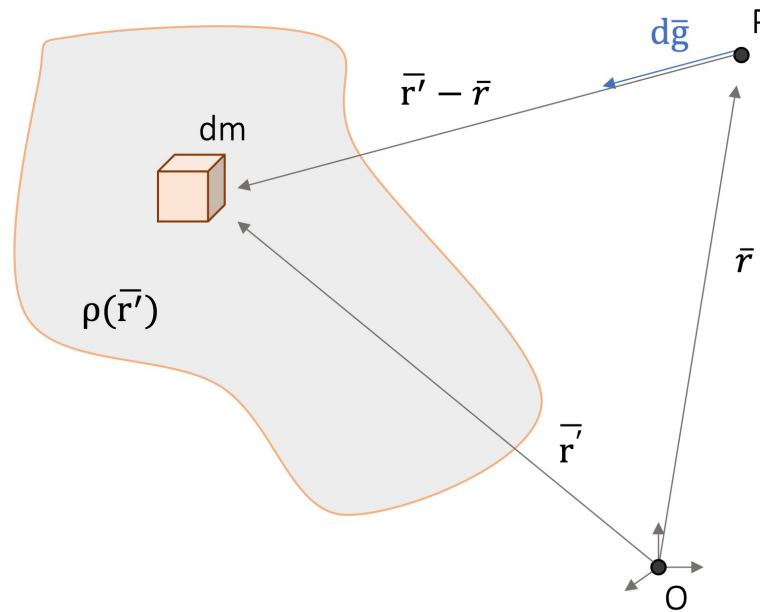
Figure 2.2 – Sketch for the computation of gravitational attraction at any point P in space. $d\vec{g}$ is the gravity acceleration vector acting in P due to the mass element dm, determined by the density distribution $\rho(\vec{r})$. The final attraction in P is the cumulative effect of every mass element dm as a function of their distance from the given point.

The gravitational attraction at a certain point in space, exerted by a given density distribution ρ, can be written in the general form:

$$\vec{g}(\vec{r}) = G \int_V \rho(\vec{r'}) \frac{(\vec{r'} - \vec{r})}{(\vec{r'} - \vec{r})^3} dV' \tag{2.2}$$

where G is the universal gravitational constant ($G = 6.67430 \cdot 10^{-11} \frac{Nm^2}{kg^2}$), $\vec{r}$ the location vector at which the gravity field is computed and dV' the volume element across which the density $\rho(\vec{r'})$ is defined.

When we compute the gravity field for a finite number of discrete homogeneous bodies, the resulting gravity attraction is the sum over all the considered bodies and it is a linear function

of density, for a given homogeneous and fixed geometry.

The implementation of equation 2.2 allows us to compute the gravitational attraction exerted by a certain Earth model, defined by a suitable range of geometry and density parameters. Nevertheless, modelling the gravity effect of complex 3D bodies can pose important challenges in the numerical implementation of equation 2.2 (Götze and Lahmeyer, 1988). Depending on the purpose of the investigation and on the context of the problem, 2D approximations may replace a full 3D calculation; subparagraphs 2.2.1 and 2.2.2 describe the type of modelling I adopted in the frame of this thesis.

As we are interested in detecting and characterizing anomalous intra-crustal structures, which represent a discontinuity in the properties of a given crustal background, gravity observations have to be corrected for the effect of several sources prior to be compared with synthetic data. The absolute gravity values, obtained by attaching the measured relative gravity network to known absolute reference points, are first corrected for the instrumental drift, the gravity tides and the latitude variations of the reference gravity field.

Subsequently, each gravity point is corrected for the measurement point elevation with respect to a reference level, i.e. the local geoid height. The free-air elevation correction can be expressed at a first-order approximation as:

$$\Delta g_h = \frac{2hg_0}{r_0} \tag{2.3}$$

where h represents the elevation with respect to the reference level r_0, and g_0 represents the reference gravity field. Δg_h is called free-air correction, which subsequently allows to define the free-air anomaly as:

$$\Delta g_{free} = g_{obs} - g_0 - \Delta g_h \tag{2.4}$$

where g_{obs} represents the measured gravity value, which accounts already for the above-mentioned preliminary corrections.

Most-often for ground gravity surveys, the layer of thickness h between the observed gravity measurement and the reference elevation is filled with topographic masses. In fact, the effect of the surrounding topographic masses above the reference elevation should be removed when the target is the crustal structure at depth. This further correction goes with the name of Bouguer correction, and it consists of two contributions:

$$\Delta g_{Bouguer} = plate_{correction} + topography_{effect} \tag{2.5}$$

where the first term represents a first-order correction for slowly-varying horizontal topographic layers, while the second term represents a correction for the higher-resolution topography surrounding the measurement point, which is of crucial importance for gravity

surveys in mountain areas and is usually known as *terrain* correction. Traditionally, ρ_c is the standard density associated with topographic masses considered in this correction, and is usually taken at 2670 $kg \cdot m^3$. However, in chapter 3 the limitations of considering a unique, constant density for all the topography above sea level are discussed and addressed, following the heterogeneous and high-density rocks of the Ivrea-Verbano zone. Eventually, we can define the complete Bouguer gravity anomaly as:

$$\Delta g_{Anomaly} = g_{obs} - g_0 - \Delta g_h - \Delta g_{Bouguer} \tag{2.6}$$

The $\Delta g_{Anomaly}$ can be used as a reference to model the gravity effect of density bodies and/or target domains. For example, in mountain regions at isostatic equilibrium, we expect the Bouguer gravity anomaly to act as a negative mirror of the topography, because of the lighter crustal roots associated with the mountain chain. Deviations from this trend can suggest the existence of anomalous density distributions in the sub-surface (Turcotte and Schubert, 2002). This is clearly the case for the IGB (see chapters 3 and 4).

2.2.1 2D forward modelling

The gravitational attraction of a two-dimensional body can be expressed as a line integral along its perimeter (Hubbert, 1948). This was later implemented for a N-sided two-dimensional polygon (Talwani et al., 1959; Won and Bevis, 1987), providing explicit formulas for the computation of the associated gravity field. In the frame of this thesis, I followed the approach proposed by Won and Bevis (1987), which is based on Talwani et al. (1959), but makes use of a minimum amount of trigonometric functions, allowing for an efficient and straightforward implementation. This approach is computationally cheap and much more simple than a full 3D gravity calculation. This can be particularly useful when studying a certain structure along a two-dimensional cross-section, whose geometry can be described with a 2.5D model (e.g. Druet et al., 2018; Hetényi et al., 2007; Tiberti et al., 2005). Eventually, the horizontal and vertical components of the gravity anomaly for a N-sided two-dimensional polygon of given density can be written as:

$$\Delta g_z = 2G\rho \sum_{i=1}^{n} Z_i \tag{2.7}$$

and

$$\Delta g_x = 2G\rho \sum_{i=1}^{n} X_i \tag{2.8}$$

where G is the gravitational constant, ρ the polygon density, Z_i and X_i the line integrals associated with the i-th side of the polygon. The reader is referred to Won and Bevis (1987)

for the complete implementation of these formulas and to chapters 4 and 5 for their further application. The linearity of the gravity field, with respect to the existing sources, allows a straightforward application of these formulas for a collection of such polygons. I apply formulas 2.7 and 2.8 in chapters 4 and 5 to investigate the IGB along the Val Sesia profile and the crustal density distribution along the GBT profile, using a home grown (MATLAB) script.
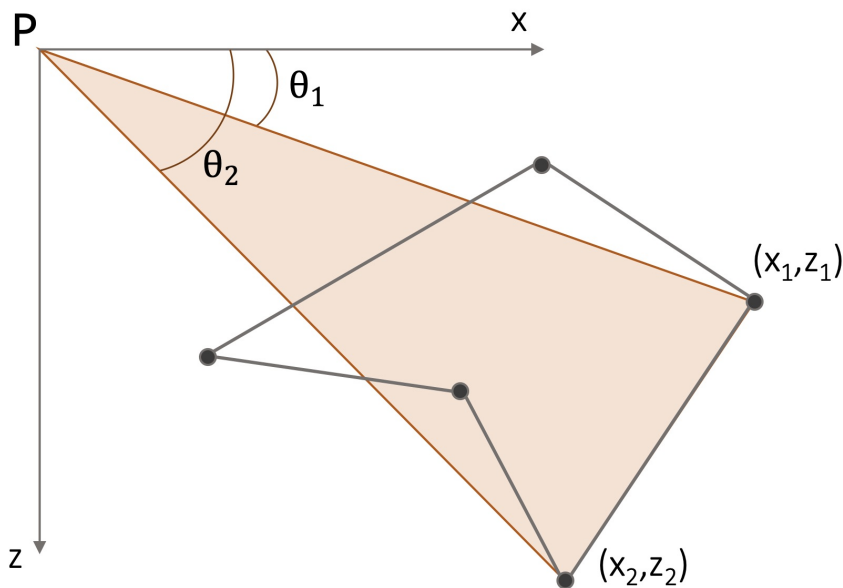
Figure 2.3 – Sketch of a 2D polygon (grey) for which we compute the gravitational attraction at point P. For a given constant density ρ, the 2D formulas 2.7 and 2.8 can be used. The final gravity anomaly is determined by the sum of line integrals computed for each of the polygon sides.

2.2.2 3D forward modelling: IGMAS+

In the frame of this thesis, I performed a full 3D density modelling of gravity data, by using the software IGMAS+ (Interactive Geophysical Modelling Application System, Schmidt et al., 2010). This software allows, among other features, to process and interpret gravity data fields, once that surface gravity measurements are provided. It can account for different 3D bodies of given density and it has been successfully used in the literature for modelling 3D crustal and lithospheric structures (e.g. Autin et al., 2016, Köther et al., 2012). In this case, the solution of the volume integral in equation 2.2 for homogeneous body is based on the reduction of the volume integrals to surface integrals across bounding polyhedra, which are defined by triangles (Götze and Lahmeyer, 1988). The software allows for an interactive modification of the bodies' geometry, with a graphical feedback on the associated gravity anomaly. The geometry of the bodies can be modified across a set of user-defined parallel and non-necessarily equidistant two-dimensional cross-sections, allowing for geometry vertices to be moved across each of

the cross-section planes.

I used the IGMAS+ software to build a 3D density model for the IGB beneath the IVZ, where the gravity data was measured and corrected for density-dependent rock masses above sea-level. Further details on the processing and modelling procedure are presented and discussed in chapter 3.

2.3 The IvreaArray seismic experiment

IvreaArray (Hetényi et al., 2017) is a passive seismic experiment and a complementary experiment of AlpArray (Hetényi et al., 2018). It took place in the Ivrea-Verbano zone for two years and three months (from June 2017 to September 2019) and collected seismic data along Val Sesia (Piemonte, Italy), crossing the IVZ from West to East (Figure 2.4).
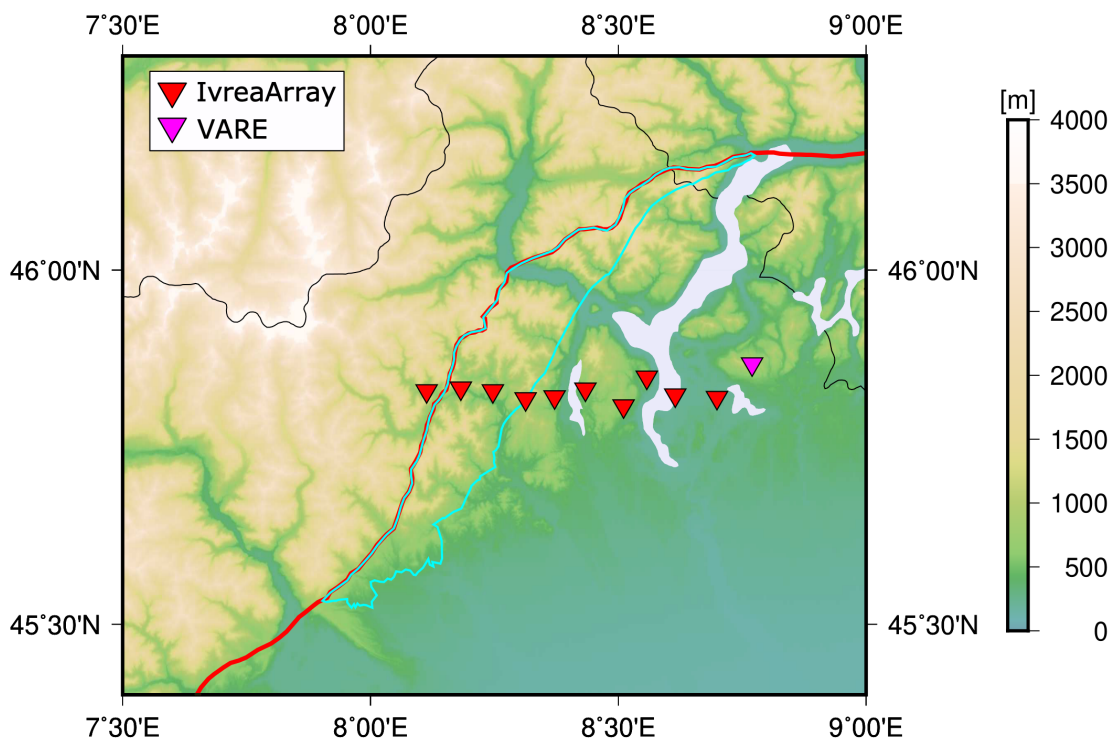
Figure 2.4 – Topographic view of the study area around the Ivrea-Verbano zone (green shape in figure), with the location of the *IvreaArray* broadband seismic stations (red triangles) and the permanent seismic station VARE from the INGV seismic network (magenta triangle). The red line represents the Insubric Line crossing the study area and the black line the border between Italy and Switzerland.

In the context of IvreaArray, 10 broadband seismic stations were deployed along a linear West-East profile at a ca. 5 km inter-station spacing. The mean latitude of the profile was 45.83°N, starting few kilometres West of the Insubric Line, crossing the lower to middle crustal composition outcrops of the IVZ and extending until the eastern shore of Lago Maggiore.

The whole profile ranges ca. 50 km from 8.11°E to 8.77°E, including the permanent seismic station VARE from the IGNV seismic network. The station metadata is accessible online at doi.org/10.5281/zenodo.1038209 (Hetényi et al., 2017), and the new seismic data will be freely available from September 2022 through the ORFEUS data center, under the FDSN network code XK.

The network continuously recorded data at 100Hz sampling frequency for 27 months, with the main purpose of providing a seismic database at a higher spatial resolution with respect to the previous passive seismic experiments addressing the crustal structure of the Western Alps, with a particular focus on the IGB. Throughout the IvreaArray operation time, regular visits were done every three-to-four months to check proper equipment functioning and to collect raw data, which was recorded on a SD card in loco. Every seismic station was equipped with a Güralp CMG-3ESP seismometers of the Czech MOBNET pool (Figure 2.5), with 60s lower corner frequency, and a GNSS sensor to guarantee a proper time synchronisation of the internal sensor clock (Figure 2.6). Station's state-of-health messages have been received daily, allowing monitoring of the network and of its conditions. The IvreaArray network ran smoothly during its operational time, with only one power outage problem, resulting in more than 90% of data recovery.

Figure 2.5 – Picture of the broadband seismic sensor IA06A installed in the framework of the IvreaArray seismic experiment, in the village of Cheggino.

Figure 2.6 – Picture of the GNSS sensor (little black antenna on the right) which equipped every seismic station, to ensure a proper time synchronisation of the internal sensor clock. Next to it on the left, the mobile antenna for routine SMS notifications.

2.4   Seismic receiver functions

There exist numerous ways of processing recorded seismic data to extract information on subsurface structures beneath a seismic receiver, both in terms of bulk rock physical properties and seismic discontinuities. In the scope of this thesis, I used seismic signals recorded from teleseismic earthquakes (with epicentral distance $\Delta > 28°$) to compute and subsequently analyse seismic receiver functions: a deconvolution-based technique which became increasingly popular after the work of Langston (1979). More specifically, I focused on applying this method to image intra-crustal structures.

A seismic receiver function is obtained when a teleseismic direct P-wave encounters a seismic discontinuity (i.e. an impendence contrast) in the propagating medium, producing smaller amplitude P-to-S (Ps) converted phases, which propagate to the surface at a lower seismic velocity than the direct P-wave, and produce secondary arrivals in the P-wave coda (Figure 2.7a). The seismic receiver function is computed by processing the vertical and the horizontal radial and transverse seismogram components, to eventually enhance the signal-to-noise ratio of these secondary converted Ps-phases and their multiple reflections (PpPs-, PpSs- and PsPs-phases), which all follow in time the direct P-wave arrival.
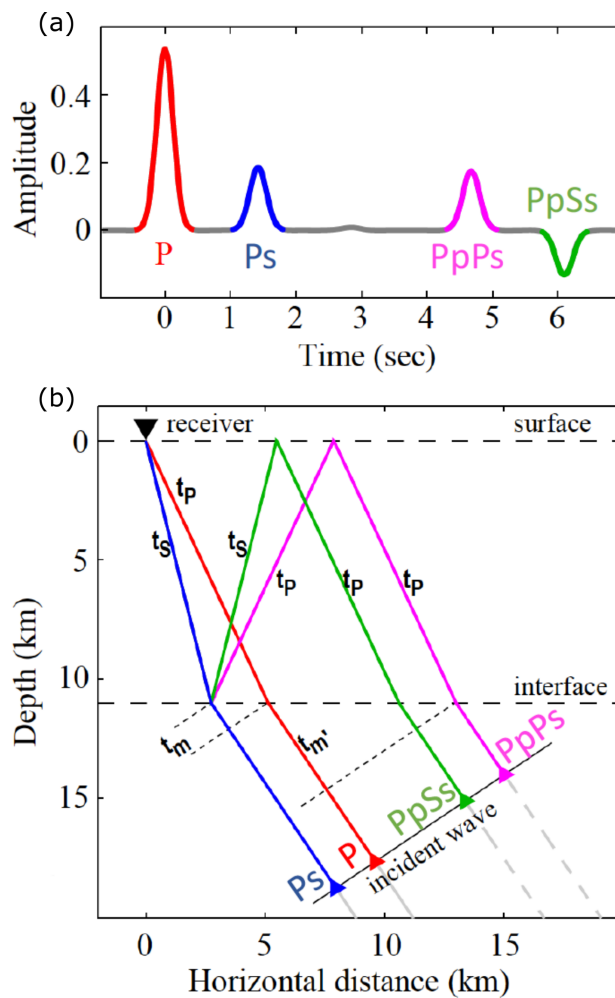
Figure 2.7 – (a) Sketch of the receiver function trace for a single flat and horizontal seismic discontinuity, located beneath the seismic receiver. The first arrival at 0s is the direct P-phase (red peak), which acts as a time reference for the subsequent converted-phase arrivals (blue, pink and green peaks). The delay times associated with the Ps, PpPs and PpSs phases contain information on the depth the seismic discontinuity beneath the seismic receiver, and on the v_P/v_S ratio of the shallowest layer (Zhu and Kanamori, 2000). (b) Simplified sketch of the subsurface path of the direct P-phase and the conveted phases, generated when the direct P-wave crossed a seismic discontinuity. All the converted phases and multiple reflections follow in time the direct-P arrival. Image modified after Hetényi (2007).

The Ps-phase amplitude in general depends on the angle of the impinging direct P-wave at the seismic discontinuity, and on the magnitude of the impedance contrast itself, with a major sensitivity for the shear-wave seismic velocity contrast (δv_S). The delay times of the converted phases and their multiple reflections, with respect to the direct-P arrival, contain important information on both the layer thickness related to the seismic discontinuity and on the associated velocity structure. It should be noted that there exist a trade-off between layer thickness and absolute velocity values, with RFs mainly able resolve well the velocity contrasts,

25

but much less the whole crustal velocity profile (Ammon et al., 1990). In a simple case scenario with a single flat horizontal interface (Figure 2.7b), the formulas for the converted-phases time delays can be written as:

$$
\begin{aligned}
t_{Ps} &= H \cdot \left[\sqrt{\frac{1}{v_S^2} - p^2} - \sqrt{\frac{1}{v_P^2} - p^2} \right] \\
t_{PpPs} &= H \cdot \left[\sqrt{\frac{1}{v_S^2} - p^2} + \sqrt{\frac{1}{v_P^2} - p^2} \right] \\
t_{PpSs/PsPs} &= 2 \cdot H \cdot \left[\sqrt{\frac{1}{v_S^2} - p^2} \right]
\end{aligned}
\tag{2.9}
$$

where H is the layer thickness, p the seismic ray parameter for the seismic event-station pair, and v_S and v_S the shear- and compressional-wave seismic velocities respectively. These formulas (equation 2.9) can be implemented to investigate the physical properties associated with a simple but effective one-layer model of the subsurface (e.g. Zhu and Kanamori, 2000): this technique is also known as $H - K$ stacking.

A receiver function can be mathematically defined as the deconvolution of the vertical seismogram component from the horizontal seismogram component (Langston, 1979). We can model the seismogram components as convolution products, by writing:

$$
\begin{aligned}
Z(t) &= S(t) * E_z(t) * I(t) \\
R(t) &= S(t) * E_r(t) * I(t) \\
T(t) &= S(t) * E_t(t) * I(t)
\end{aligned}
\tag{2.10}
$$

where $*$ is the convolution operator, Z(t), R(t), T(t) are the vertical, radial and tangential seismogram components respectively, S(t) the earthquake source time function, I(t) the instrumental filter effect, E_z, E_r, E_t the effects on the respective seismogram components of the local Earth structure beneath the seismic receiver.

By assuming $E_z(t) \approx 1$ (i.e. approximate the local Earth structure on the seismogram vertical component), then we can mathematically define the receiver function as:

$$
RF(t) = R(t) \oslash Z(t) \approx E_r(t)
\tag{2.11}
$$

where $\oslash$ is the deconvolution operation of Z(t) from R(t) and RF(t) is a time series, whose peaks' amplitude and distribution are related to the near-receiver crustal structure.

In general, solving equation 2.11 requires solving a deconvolution problem. This task has been addressed and discussed in the literature (Oldenburg, 1981), and different approaches

have been suggested to obtain a solution, either based on a water-level-stabilised frequency domain division (e.g. Clayton and Wiggins, 1976) or a time-domain approach (e.g. Gurrola et al., 1995; Sheehan et al., 1995).

To compute the seismic receiver functions for the IvreaArray seismic data, I implemented the method by Ligorría and Ammon (1999). This method performs a time-domain iterative deconvolution to solve equation 2.11, by iteratively cross-correlating the vertical and the horizontal seismogram components to locate the seismic arrivals, with the advantage of avoiding the potential unstabilities of a spectral division (Ligorría and Ammon, 1999).

Receiver functions featured a wide range of contributions in the literature, which addressed the Earth structure at various spatial scales: from regional $H - K$ stacking applications for the Moho depth and the associated poisson ratio (e.g. Licciardi et al., 2014; Piana Agostinetti and Amato, 2009; Lombardi et al., 2008), to mantle transition zones (e.g. Agius et al., 2017) and underthrusting at continental margins (e.g. Nábělek et al., 2009). In chapter 4, I further discuss the receiver functions computed from the IvreaArray data, together with their joint inversion with gravity data for the intra-crustal structure of the IGB. In this particular analysis, I implement and perform receiver function migration, which is a processing technique used to reconstruct the 2D subsurface structures as sampled by the receiver functions (Zhu, 2000), by combining the receiver function delay times with a given velocity model (e.g. Hetényi et al., 2018; Subedi et al., 2018). This technique offers a valuable framework for developing a joint velocity-density parameterisation of the Ivrea geophysical body, to be used in combination with the gravity data modelling as discussed and applied in chapter 4.

3 3D Density model of the Ivrea Geophysical Body from gravimetry

This chapter presents the IGB 3D density model I developed in the frame of this theis, by modelling the new gravity data I collected across the IVZ. Its content has been published in the following article:

3.1 Summary

We provide a high-resolution image of the Ivrea Geophysical Body (IGB) in the Western Alps with new gravity data and 3-D density modelling, integrated with surface geological observations and laboratory analyses of rock properties. The IGB is a sliver of Adriatic lower lithosphere that is located at shallow depths along the inner arc of the Western Alps, and associated with dense rocks that are exposed in the Ivrea-Verbano Zone (IVZ). The IGB is known for its high seismic velocity anomaly at shallow crustal depths and a pronounced positive gravity anomaly. Here, we investigate the IGB at a finer spatial scale, merging geophysical and geological observations. We compile existing gravity data and we add 207 new relative gravity measurements, approaching an optimal spatial coverage of 1 data point per 4–9 km^2 across the IVZ. A compilation of tectonic maps and rock laboratory analyses together with a mineral properties database is used to produce a novel surface rock-density map of the IVZ. The density map is incorporated into the gravity anomaly computation routine, from which we defined the Niggli gravity anomaly. This accounts for Bouguer Plate and terrain correction, both considering the *in situ* surface rock densities, deviating from the 2670 $kg \cdot m^{-3}$ value commonly used in such computations. We then develop a 3-D single-interface crustal density model, which represents the density distribution of the IGB, including the above Niggli-correction. We retrieve an optimal fit to the observations by using a 400 $kg \cdot m^{-3}$ density contrast across the model interface, which reaches as shallow as 1 km depth below sea level. The model sensitivity tests suggest that the ~300–500 $kg \cdot m^{-3}$ density contrast range is still plausible, and consequently locates the shallowest parts of the interface at 0 km and at 2 km depth below sea level, for the lowest and the highest density contrast, respectively. The former model requires a sharp density discontinuity, the latter may feature a vertical transition of densities on the order of few kilometres. Compared with previous studies, the model geometry reaches shallower depths and suggests that the width of the anomaly is larger, ~20 km in west–east direction and steeply E–SE dipping. Regarding the possible rock types composing the IGB, both regional geology and standard background crustal structure considerations are taken into account. These exclude both felsic rocks and high-pressure metamorphic rocks as suitable candidates, and point towards ultramafic or mantle peridotite type rocks composing the bulk of the IGB.

3.2 Introduction

The present-day architecture of the Alps is the result of a succession of lithospheric-scale processes, involving the collision between the two major European (to the North) and African plate (to the South), since 35 Ma (Handy et al., 2015), following the opening and the subsequent subduction of the Piemonte-Liguria ocean (e.g. Handy et al., 2010). The Europe-Adria collision, with Adria as the largest among the micro-plates involved in the collision, provided most of the rock mass of the current Alps (Schmid et al., 2004). The resulting geometry of the Alps is structurally complex both at the surface and at depth, and has been continuously investigated by a broad spectrum of geological and geophysical methods for more than a

century. One of the outstanding features of the Alps are the Ivrea-Verbano Zone (IVZ) and the Ivrea Geophysical Body (IGB).

The IGB is considered as a sliver of Adriatic lower lithosphere, which was emplaced in the upper crust along the inner arc of the Western Alpine domain and is located at unusually shallow depths (e.g., Schmid et al., 2017). This work focuses on its north-eastern portion, where the IGB is partially outcropping at the surface and presents a variety of middle-to-lower crustal and mantle composition rocks, across the geologically well-known IVZ (Figure 3.1). This almost-unique complex can be regarded as a nearly complete cross-section of the continental crust (Fountain, 1976) and it has been the subject of a variety of laboratory sample analyses for rock physical properties (e.g. Khazanehdari et al., 2000, Fountain, 1976), tectonic mapping (e.g. Schmid et al., 2004, Brack et al., 2010, Petri et al., 2019) and petrological studies aiming at deciphering magmatic processes (e.g. Rivalenti et al., 1995, Sinigoi et al., 2011, Karakas et al., 2019) and its emplacement (Quick and Denlinger, 1993, Quick et al., 1994, Quick et al., 2003). This exposed cross-section is delimited on its north-western side by the Insubric Line (Figure 3.1), i.e. the western end of the largest fault system in the Alps, marking the boundary between the Adriatic plate and the orogenic wedge. From a geological point of view, it separates the Southern Alps – with a very low grade of Alpine metamorphism – from the Western, Central and Eastern Alps – with moderate to high grade Alpine metamorphism (e.g. Schmid et al., 1989, Bousquet et al., 2012). Several contributions support the idea of this fault being a sub-vertical to vertical feature, cutting across our study area, both from structural evidences (e.g. Berger et al., 2012, Schmid et al., 1987, Schmid et al., 1989) and geophysical investigations (e.g. Schmid and Kissling, 2000).
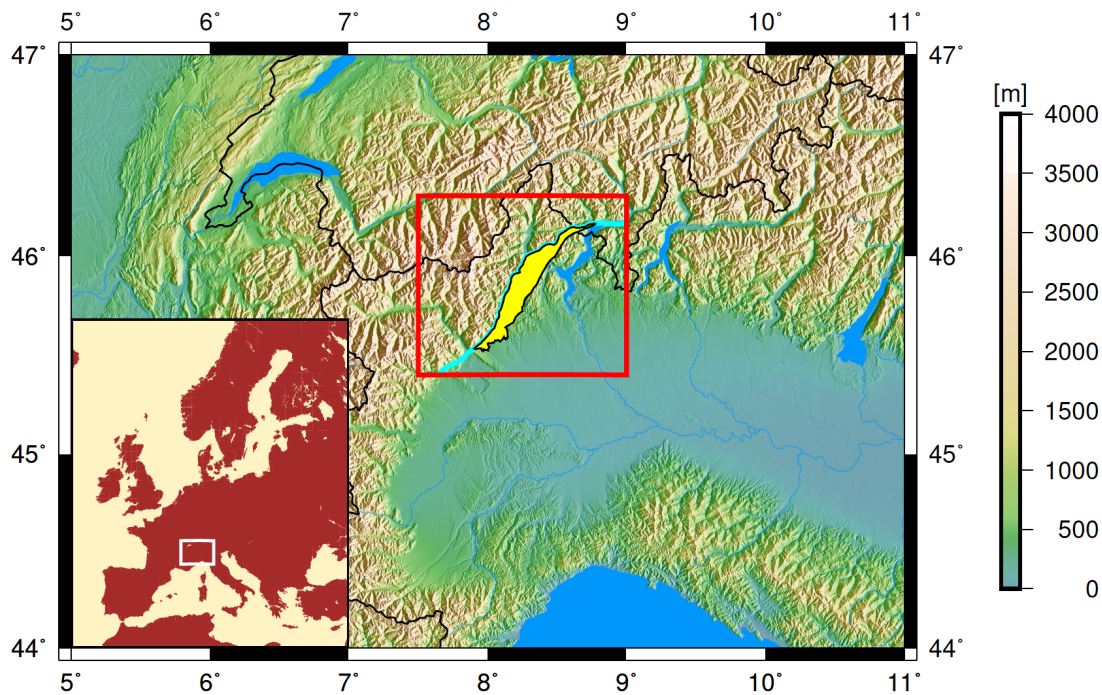
Figure 3.1 – Topographic map of the Western European Alps (see inset for broader location). The red box is the region of the interest for this study, focusing on the geologically well-known Ivrea-Verbano Zone, indicated in yellow (from Petri et al. (2019)), and bounded to the West by the Insubric Line (shown only within the red box, in cyan). Figures 2 to 6 show the same area than the red box.

In this work, we focus on the IGB structure beneath the IVZ, which is characterized by two main geophysical anomalies: a pronounced positive gravity anomaly and a high seismic P-wave velocity anomaly. The IGB density structure and the associated gravity anomaly have been addressed by several contributions in the literature (e.g., Niggli, 1946, Vecchia, 1968, Marson et al., 1994), leading to the production of different crustal density models. These range from continuous bodies with a constant density and a sharp density-contrast interface (e.g. Berckhemer, 1968, Kissling et al., 1984) to numerous and varying-size block-assembled models, employing different density contrasts (e.g. Bürki, 1990, Bayer et al., 1989, Rey et al., 1990). The profile presented by Berckhemer, 1968 shows an anomalous body similar in shape to a bird with a head, a neck and a beak, from which the term bird's head is sometimes used in the literature.

A certain number of Bouguer anomaly maps have also been produced from field-data, highlighting a broad agreement on the order of magnitude of the anomaly's amplitude and on the main location of the pronounced positive anomaly, associated with the IGB (Figure 3.2). Nevertheless, differences between these maps arise when it comes to compare iso-anomaly contour shapes and locations, crest lines and local maxima, most likely because of the heterogeneous and sparse data coverage and interpolation artefacts (Figure 3.2).
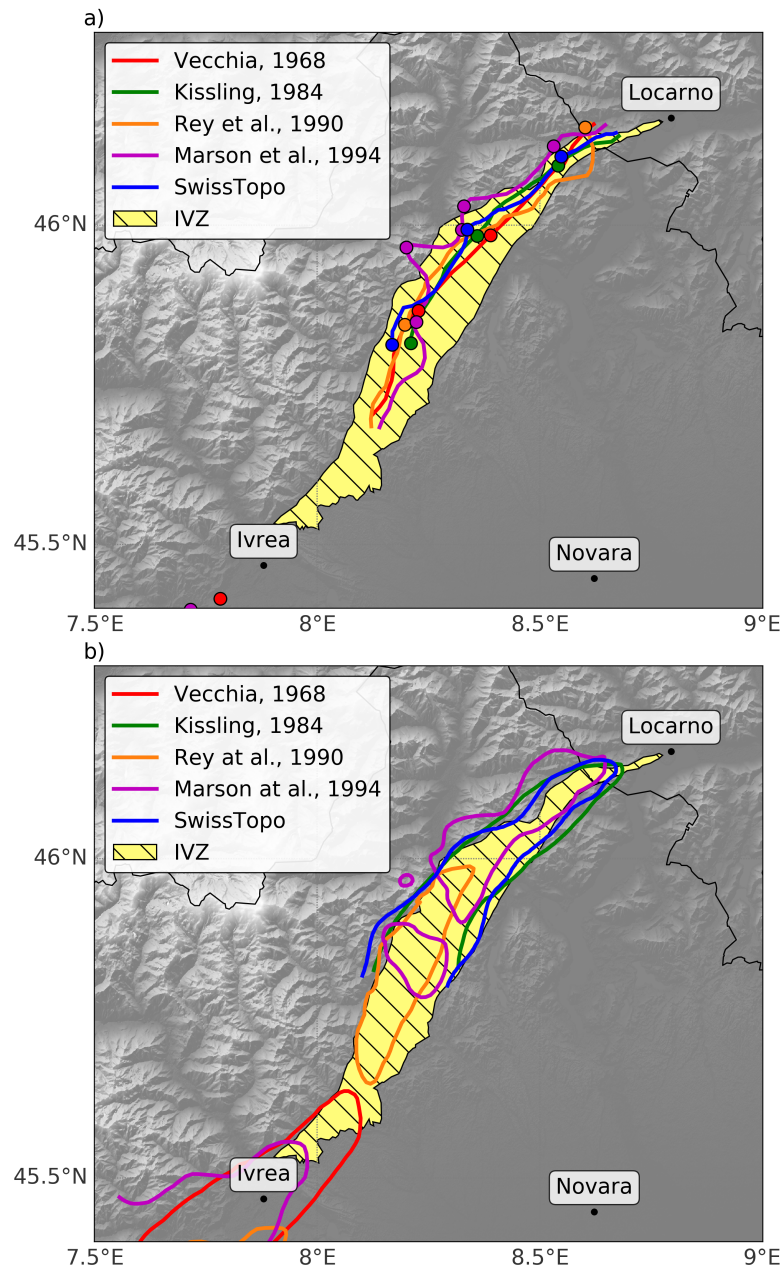
Figure 3.2 – Compilation of previous gravimetric works, as referenced in the legend, having mapped Bouguer anomalies in the area. All document a pronounced positive anomaly following the geological Ivrea-Verbano Zone (IVZ, in yellow). (a) Location of the crest lines and the local maxima. (b) The 0 mGal anomaly contour lines. (a) and (b) highlight discrepancies between the maps.

The main constraints on the IGB structure and geometry were first given by seismic refraction experiments across and along the Western Alps (e.g. Berckhemer, 1968, Ansorge et al., 1979). These seismic investigations provided the first constraints on the gravity models of the shallow

IGB structure, suggesting the existence of seismic interfaces as shallow as few kilometres. Later, the IGB has been detected with reflection seismics as well (e.g. Bayer et al., 1989, Thouvenot et al., 1990), highlighting shallow seismic features that served as guidance for the further development of two-dimensional (2D) density models with gravity data (e.g. Rey et al., 1990, Bayer et al., 1989). More recently, important insights on the IGB structure and bulk properties came from local earthquake tomography, showing anomalous P-wave seismic velocities in the range of 7-8 km/s at middle-crustal depth (e.g. Solarino et al., 2018, Diehl et al., 2009).

We also base our study on a seismically-constrained Moho map over the whole region (Spada et al., 2013) which, together with the latest seismic tomography experiments, offers a suitable and homogeneously-defined initial structure for the development of a higher-resolution 3D crustal density model. Indeed, while tomographic images reveal a broad-scale connection between the top of the bird's head imaged by active seismics and the European Moho at more than 40 km depth and shallower on the Adriatic side at ca. 35 km, the size and geometry of the IGB at depth still remain uncertain. Here, we advocate for the need for higher-resolution imaging to investigate the shallow upper-crustal density-structure beneath the IVZ and to look at the IGB in more detail, using gravimetry and geological field surveys. This is especially important in the perspective of understanding how seemingly dense rocks are emplaced at shallow depth in an orogen, and in particular in light of the forthcoming scientific drillings in the area (Pistone et al., 2017). For the latter, progress towards an exhaustive, investigation of the IGB and new insights on the IVZ crustal structure, by means of a complete and up to date gravity database of the area, are a strategic step.

For this purpose, we have collected new and compiled old gravity data, together with surface rock density information. We developed a new 3D density model, defined by a single density-contrast interface within the crust, by iteratively minimizing the misfit between synthetic data and gravity anomaly observations. We define a new gravity anomaly correction, the Niggli correction, in order to account for the surface density deviations from the otherwise constant correction density 2670 $kg \cdot m^{-3}$ and we incorporate this correction into the computations. The sensitivity of model geometry to the crustal density contrast is then investigated in order to explore the acceptable range of model geometries and density contrasts, which may add constraints on the nature of the rocks composing the IGB.

3.3 Gravity data acquisition

A new gravity database was compiled by merging existing gravity datasets with our own newly acquired dataset, aiming at a homogeneous spatial coverage of one gravity point per 4 to 9 km^2. This allows for a detailed mapping of the regional anomaly and brings the investigation scale closer to the available geological observations within the IVZ, as represented by the various tectonic units adopted from Petri et al. (2019) and from Manzotti et al. (2014) for what lies to the North-West of the Insubric Line (Figure 3.4a). In the following, the data collection procedure and pre-processing practices (from raw data to absolute gravity values) are presented.

3.3.1   Existing gravity data compilation

Existing gravity data have been compiled from several sources. The Swiss Federal Office of Topography (Swisstopo: https://www.swisstopo.admin.ch/) provided one dataset covering some of the North-Italian valleys and a dataset covering the fraction of Swiss territory of our interest. Additional data has been obtained from the Istituto Nazionale di Oceanografia e di Geofisica Sperimentale (OGS: https://www.inogs.it/).

This preliminary compilation served as basis for field-campaign planning across our study area, which presents several areas of limited accessibility due to their rough topography and limited road network in the high mountain areas. Therefore, the measurement locations have been defined in order to refine the previously available dataset and to obtain a data coverage as homogeneous as possible. The new data is available upon request and will be publicly released by end of 2020.

3.3.2   New gravity data collection

We reached the majority of the locations by road vehicle, on foot (0.5 to 3 hours hiking to the target location for a dozen of points) and by helicopter, the latter to reach the most remote areas. By the end of our field efforts, requiring ca. 36 days in the field, in September 2017, June 2018 and September 2019 respectively, we have made measurements at 207 new gravity points, which has drastically improved the spatial coverage map (Figure 3.3). The average distance of a newly measured gravity point to their respective nearest neighbour – in the previous dataset – is 2.1 km, while it is 2.9 km to nearest 4 existing points, on average.
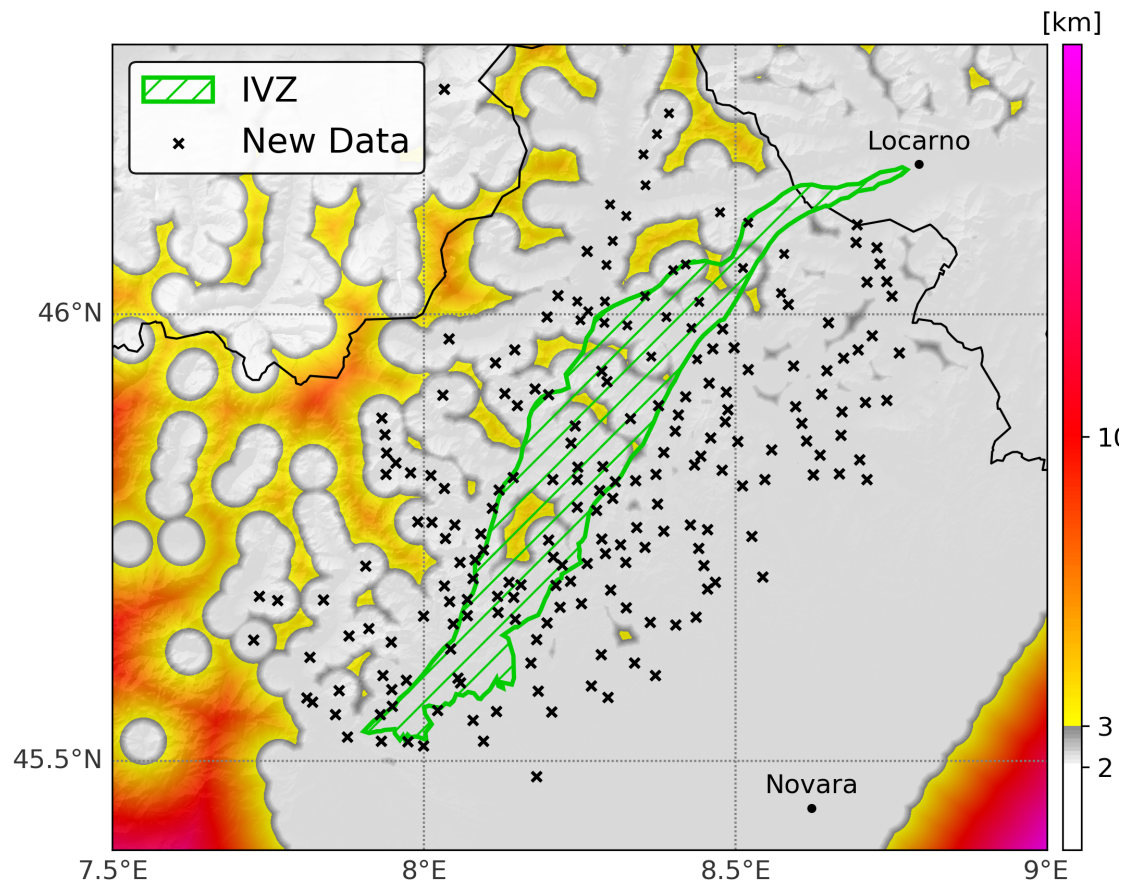
Figure 3.3 – Gravity data coverage around the IVZ (green contour), obtained by merging previous gravity databases and newly collected gravity measurements. The black crosses represent the 207 new relative gravity points from this project. The colour map indicates the distance to the nearest gravity point, white-to-gray representing our intended optimal coverage.

All measurements were organised into daily loops, with each day or half-day of field campaign starting and finishing at the exact same location. This practice allows to estimate the gravimeter instrumental drift, a mechanically inherent property of the instrument which needs to be estimated and then subtracted from each measurement, assuming that the drift is linear during the loop.

At each site, a Scintrex CG-5 relative gravimeter was used to measure the local gravity variation, with respect to the previous site or the starting point of the associated daily loop. In this way, relative gravity variations are recorded at each step along the loop.

As a result, we obtained a relative but self-consistent network, with fixed gravity variations within the network, that needs to be referenced to an absolute gravity point. We connected our network to the established gravity reference points at the Simplon Pass (Switzerland) and at the Polytechnic of Milan (Italy), where the very first loop of the campaign started. After measuring gravity in the absolute reference point in Milan, additional reference points for

further loops were defined progressively, allowing for an expansion of the network loop by loop.

3.3.3 Point location and elevation estimate

For each gravity point, the elevation estimate at the measurement site is of fundamental importance for the subsequent data processing and modelling, as each meter of vertical displacement upward in free atmosphere corresponds to ca. 0.3086 mGal decrease in gravity. For the purpose of estimating elevation, a stand-alone GNSS (Global Navigation Satellite System) receiver antenna (TopCon, www.topconpositioning.com) has been used at each site to record satellite signals for ca. 20 minutes at 1 Hz sampling rate. Repeated measurements at the same location show that this setup allows a 0.5 m precision on the elevation estimate, obtained via PPP (Precise Point Positioning) processing from Natural Resources Canada (https://webapp.geod.nrcan.gc.ca/geod/tools-outils/ppp.php). This open-access service provides longitude and latitude coordinates in the WGS84 reference system as well. The ellipsoidal height, given by the PPP procedure, is then converted to the physical height, by interpolating the geoid map of Italy (Corchete, 2010) at our measurement locations. To ensure the best precision, we measured the gravimeter and GPS antenna elevations from the ground with 1 cm precision, and referenced our gravity data points homogeneously. The elevation of the newly acquired points ranges from 117 to 2009 m.

3.3.4 Gravity data pre-processing

Processed GNSS coordinates and raw gravity data, organised into ordered loops, were processed via the GRAVPROCESS software (Cattin et al., 2015). This tool calculates point-wise absolute gravity values, free-air gravity anomaly and complete Bouguer gravity anomaly values, by applying corrections for tides, atmospheric pressure, instrumental drift, latitude, elevation, as well as the Bouguer plate and terrain corrections.

The terrain correction is especially important in mountain areas and contributes to the signal by several mGals (1 mGal = $10^{-5}\,m/s^2$); it is thus fundamental for a correct estimation of the Bouguer gravity anomaly. In our study, we used the SRTM digital elevation model (Shuttle Radar Satellite Mission, Farr et al., 2007) for the terrain correction in the whole region, together with the measured site elevations. The gravitational effect of topography has been computed within a 166.917 km radius circle (second Hayford zone) around each gravity point, by interpolating the digital elevation model over a 2D mesh grid, whose resolution is decreasing with the distance from the gravity data point. The mesh geometry parameters in GRAVPROCESS are user-defined (see the Mesh box in the software interface) and were fixed at 0.1 km, 166.917 km, and 0.3 during our calculations, representing respectively the maximum grid resolution, the maximum distance from the gravity point for topographic effects and the resolution decay with the distance from the gravity point. We refer to the GRAVPROCESS user manual for further details. Statistics on the quality of the newly processed data indicate data point uncertainties well below 1 mGal: the mean value of standard deviation of repeated measurements at a given

point is 0.015 mGal (min. 0.005, max. 0.14), the daily instrument drift mean is 0.007 mGal (min 0.001, max 0.13), and uncertainties on the final anomaly products range between 0.18 and 0.27 mGal.

We then processed uniformly a unique gravity database, made up of both compiled and newly measured data. The gravity data from various sources match well, as data represented along various profiles crossing the entire study area do not show visible systematic shifts among the different data sources. We cannot exclude the existence of smaller-amplitude systematic errors or fluctuations, on the order of one or few mGals; nevertheless, their effect would be lower than the variations introduced by the 5-km projection of data along our profiles, necessary for the modelling.

3.4   Gravity data products

The IVZ presents a variety of outcropping dense rocks at the surface, typical of middle-to-lower crust (e.g. Fountain et al., 1990). Their respective densities clearly differ from the 2670 $kg \cdot m^{-3}$ correction density used in standard gravity anomaly computations (Hinze, 2003). Hence, we define and apply the *Niggli correction* during the gravity anomaly computation. We named the corrected anomaly the Niggli anomaly in honour of one of the first authors who studied the relationship between gravity anomaly and dense-rock observations in the IVZ (Niggli, 1946). This correction accounts for surface rock-density deviations from the 2670 $kg \cdot m^{-3}$ reference value, and hence includes geological surface observations which can be local but of significant amplitude. As a first step in applying this correction, we compile a surface density map, which is in turn incorporated into the GRAVPROCESS terrain correction computation, as described below.

3.4.1   Surface rock-density map

Our study area encompasses the western end of the Southern Alps and the adjacent units of the Western Alps, separated by the Insubric Line (Figure 3.1). The studied portion of the Western Alps is located in an area where the nappe stack involves, from top to bottom, (i) continental units deriving from the Adria palaeomargin (i.e. the Sesia-Dent Blanche nappes); (ii) remnants of the Mesozoic Piemonte-Liguria ocean (i.e. the Zermatt-Saas and Combin Zone); and (iii) slices of the Iberian-European basement (e.g. Gran San Bernard, Gran Paradiso and Monte Rosa massifs) (e.g., Schmid et al., 2004; Manzotti et al., 2014). Southeast of the nappe stack (i.e. southeast of the Insubric Line boundary, Figure 4(a)), the Southalpine domain is represented by the IVZ and the Serie dei Laghi (e.g. Zingg, 1983, Boriani et al., 1971). The former is a piece of Permian middle to lower Adriatic crust whereas the latter is a piece of Permian upper Adriatic crust covered by Mesozoic sediments; both belonged to the upper plate during the Alpine orogeny.
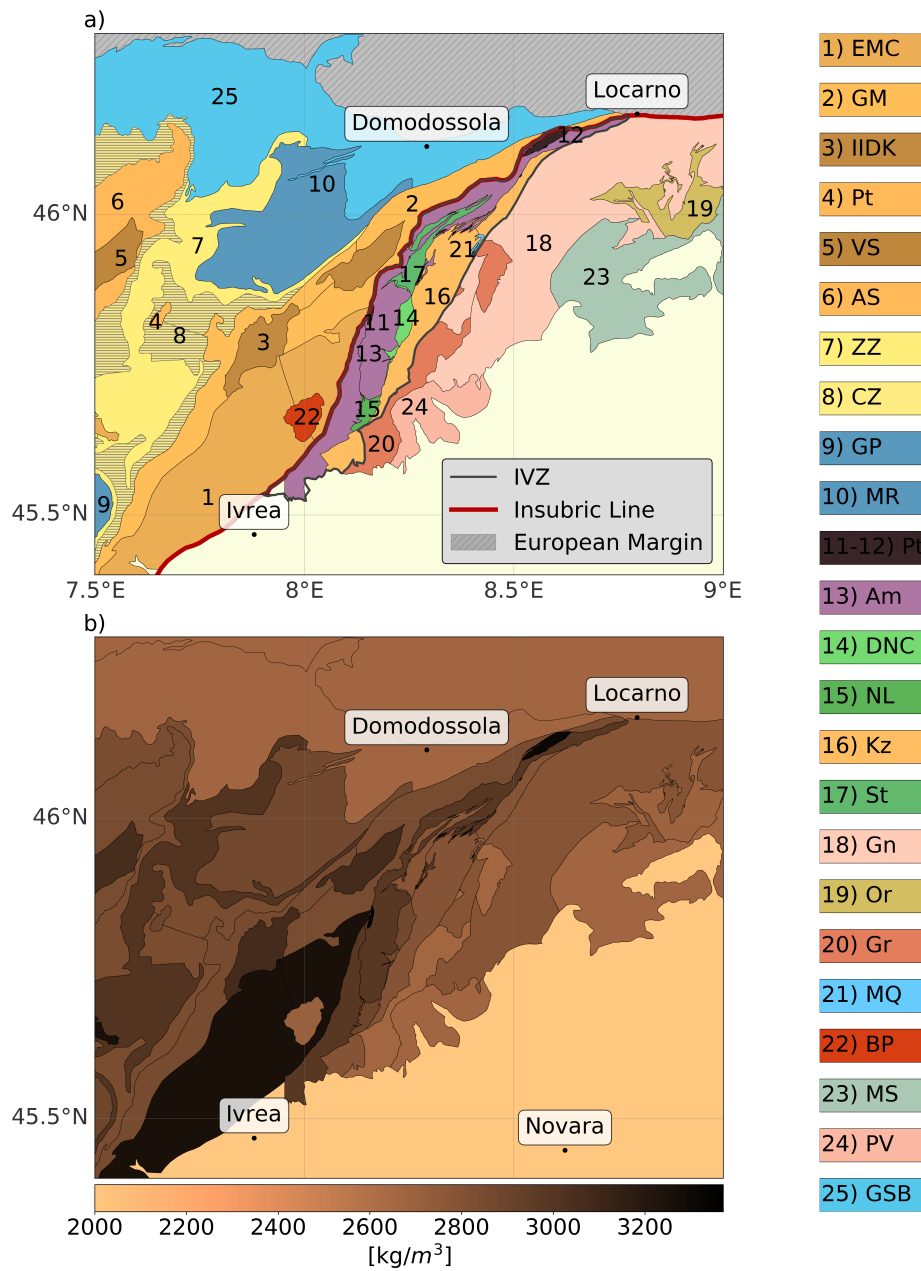
Figure 3.4 – (a) Geological units we compiled for our study area, following Bigi (1983), Manzotti et al. (2014), and Petri et al. (2019). Each compiled unit has been associated with the dominant rock composition. The legend on the right refers to each unit type as listed in Table 3.1. (b) Surface rock-density map of the Ivrea-Verbano Zone, associating a constant value with every tectonic unit as mapped in Petri et al. (2019) and Bigi (1983). The density of each unit was chosen as a mean value, on the basis of their mineralogical composition, field observations and laboratory rock-sample analyses (Khazanehdari et al., 2000, Brack et al., 2010, Petri et al., 2019). Mean unit density is shown in Table 3.1 and obtained as a result of the associated unit composition.

In order to produce a surface density map of this area, we compiled information from different sources and followed a systematic and consistent approach, both for what lies South-East of the Insubric Line (the IVZ, its sub-units and the Serie dei Laghi, Petri et al., 2019) and for what lies to the North-West (Manzotti et al., 2014). Finally, the compiled units have been merged into a single map (Figure 3.4a).

Concerning the IVZ, we follow the tectonic unit boundaries from Petri et al., 2019. We have associated each unit with a reference petrological signature (Figure 3.4a) by comparing with previous maps (Brack et al., 2010) and with laboratory rock analyses of samples collected within the units themselves (Khazanehdari et al., 2000; Table 3.1).

In order to follow a consistent procedure for the density estimation of these and subsequent units, we compiled the published petro-physical data of IVZ rock-samples with specific mineral model proportions (Table 3.1) from Khazanehdari et al., 2000 and we referred to a mineral property database (www.mindat.org) to assign individual mineral densities (Table 3.1). For minerals with end-member compositions, we considered weighted averaged densities according to expected mineral abundances in the area. Finally, we computed rock densities according to the mineral densities and the given mineral abundances (Table 3.1, Figure 3.4b). Evaluating the rock densities from mineral density and compositions is likely to be an upper bound as they are not accounting for possible presence of distributed fractures and porosity, yet rock sample porosity measurements appeared to be negligible in this area (<1 per cent for those reported by Khazanehdari et al., 2000).

Some remarkable deviations from the reference 2670 $kg \cdot m^{-3}$ arise in the IVZ, especially in the areas of exposed lower crust, including upper mantle rocks that were integrated as lenses in the lower crust (e.g., ~3370 $kg \cdot m^{-3}$ for the Balmuccia and Premosello peridotites and ~3320 $kg \cdot m^{-3}$ for the Finero peridotite).

Concerning the tectonic units on the North-Western side of the Insubric Line (Figure 3.4a), we mainly referred to the previous tectonic maps of Bigi (1983), Manzotti et al. (2014) and Brack et al. (2010). For each unit, we have considered a representative and simplified composition in terms of rocks and mineral percentages (Table 3.1). The continental Monte Rosa and Gran Paradiso units display high percentage of orthogneiss (mainly dominated by quartz, K-feldspar, and biotite). In the units derived from the Piemonte-Liguria ocean, calcschists (mainly containing calcite, quartz and white mica) are dominant in the Combin Zone, whereas the Zermatt-Saas Zone largely consists of serpentinite. A high percentage of weakly retrogressed granulite is found in some units (e.g. Valpelline Series and IIDK, Table 3.1) of the Sesia-Dent Blanche nappes.

As a result, we obtain a surface rock-density map (3.4b), composed of different units and each characterized by a representative mean density. Despite being an approximation in petrological and geological terms, this map serves well the purpose of accounting for major surface rock-density variations and deviations from 2670 $kg \cdot m^{-3}$, to be included in the gravity anomaly computation. Some units are partially extending outside the study area, still we compile them in order to account for distant contributions on the gravity measured at each site.

To further consider the existing geological knowledge at smaller spatial scales, we have in-

cluded additional information from the SAPHYR rock property catalogue (Zappone and Kissling, 2021), containing point-wise bulk-density information from laboratory analyses on rock samples from 164 locations across the IVZ. This information has been included in the density map, by smoothly interpolating between the added SAPHYR points and the assigned background unit densities (explained above). In practice, each bulk-density value from SAPHYR was assigned to the nearest point in our digital elevation model (90 m resolution) and the smooth interpolation was performed following a Gaussian-shaped bell of 1 km half-width, which is comparable to the size of the smallest mapped unit considered here. As a result, we obtain a surface density map (Figure 3.4b), showing the density associated with each mapped unit and containing local heterogeneities from point-wise information.

ID	Unit Name or Area	Density (kg/m3)	Rock Proportions (%)	Rock Type(s)	Qz	Kfs	Pl	Grt	Ctd	Bt	Ph/Ms/Pa	Chl	Omp	Jd	Di	f-Act	Gln	Hbl	Lws	Ep	Sil	Ky	Srp	Tlc	Mag	Dol	Cal	Ol(Fo+Fa)	Ru	Ilm	Titanite	Opx	Cpx	Cr-Sp	Norm	Ref
11	Balmuccia-Premosello Peridotite (IVZ)	3371	-	Peridotite																								73					25	2	100	2
12	Finero Peridotite (IVZ)	3321	-	Peridotite							5																	52				22	14	2	95*	2
13	Ivrea Mafic Complex - Gabbro 1 (IVZ)	2989	-	Amphibolite	3		40											50													2		4		99*	2
14	Ivrea Mafic Complex – Diorite (IVZ)	2870	33	Diorite			70			20																						10			100	2
			33	Norite			50																								30	15		95*	
			33	Leucochamrokite	30	25	25	10																							3		93*	
15	Ivrea Mafic Complex - Gabbro 2 (IVZ)	2890	50	Norite			50																								30	15		95*	2
			50	Leucocharnokite	30	25	25	10																							3		93*	
16	Kinzigite (Upper Amphibolite Facies Metasediments) (IVZ)	2790	-	Kinzigite	35		34	6		22	5										3													94*	2
17	Stronalite (Granulite Facies Metasediments) (IVZ)	2778	-	Stronalite	44	16	25	6		5											4												100	2
18	Serie dei Laghi (SDL)	2787	50	Gneiss Minuti	38	8	34			14	5																						99*	2
			50	Gneiss Ceneri	31		25	5		17	22																						100	
19	Ordovician Granitoids (SDL)	2689	-	Orthogneiss	45	22	23			10																							100	2
20	Permian Granite (Valle Mosso, Roccapietra, Baveno, Mont'Orfano) (SDL)	2666	-	Granite	50	26	18			6																							100	2
21	Marbles	2708	-	Marble	5																					95							100	2
23	Mesozoic Sediments	2670	-	Default Crustal Density																-												-	-
24	Permian Volcanics	2670	-	Default Crustal Density																-												-	-
1	Eclogitic Micaschists Complex	3255	20	Granite	20	10		20			15			20			5			10													100	1
			45	Metapelite	25			25	5		25	20		5			10			5									5				100	
			30	Basic Rock				25			15	15	25				15			10									5				100	
			5	Marble				10		10																20	25	10					100	
2	Gneiss Minuti	2854	10	Metapelite	25	15	10	5			15	15								10													100	1
			90	Orthogneiss	25	15	10			5	15	5								15													100	
3	IIDK	3073	70	Granulite	20	10	20	20							10							15											100	1
			20	Amphibolite			40	15		15								40		5													100	
			10	Marble				5		5																	70	10					100	
4	Pillonet	2895	80	Orthogneiss	25	10	10	10			15	15					10			15													100	1
			10	Metapelite	25	10	15	10		5	15	10					5			10													100	
			10	Marble	5		10	5			15	5								5						50	15			5			100	
5	Valpelline Series	3064	50	Granulite	20	10	20	20		15					5						15												100	1
			40	Amphibolite			40			5					10			40		5													100	
			10	Marble			5																				70	10					100	
6	Arolla Series	2849	95	Orthogneiss	25	15	10	10		5	15	15								15		5											100	1
			5	Metapelite	30	15	25			25	15																						100	
7	Zermatt-Saas Zone	3009	60	Serpentinite												5							75	5	5								100	1
			30	Basic rock				10					30				5			10									10				100	
			10	Calcschist	10		10	10			15	5								10							45						100	
8	Combin Zone	2840	5	Serpentinite												30							95										100	1
			15	Basic Rock			10	10		5	15	15								30										5			100	
			80	Calcschist	20		5				10	5								5					5		50						100	
9	Gran Paradiso	2891	20	Metapelite	30	10	5	15			25	5								5													100	1
			75	Orthogneiss	30	15	15	15		20	5	10								10									5				100	
			5	Basic Rock			10	15			10	5	20				15			10									5				100	
10	Monte Rosa	2877	15	Metapelite	30	10	15	15			25	5								5													100	1
			80	Orthogneiss	30	15	15			20	5	5					15			10									5				100	
			5	Basic Rock			10	15			10	5	20				15			10									5				100	
22	Biella Pluton	2720	-	Quartzdiorite-Monzonite																													-	3
25	Grand-Saint-Bernard	2670	-	Default Crustal Density																													-	-
	Mineral Densities (kg/m3)				Qz	Kfs	Pl	Grt	Ctd	Bt	Ph/Ms/Pa	Chl	Omp	Jd	Di	Act	Gln	Hbl	Lws	Ep	Sil	Ky	Srp	Tlc	Mag	Dol	Cal	Ol(Fo+Fa)	Ru	Ilm	Titanite	Opx	Cpx	Cr-Sp		
					2660	2536	2690	4022	3600	3050	2810	2950	3300	3300	3278	3135	3008	3200	3090	3435	3240	3670	2545	2780	5200	2876	2711	3284	4250	4789	3530	3270	3315	3578		

Table 3.1 – * Those mineral compositions who were not summing up to 100 (see Khazanehdari et al., 2000) have been normalized accordingly. 1 - Reference person Paola Manzotti, 2 - Khazanehdari et al. (2000) and 3 - Zappone and Kissling (2021). The red line represents the Insubric Line (IL). What lies to the east of the IL is reported above the red line, what lies to the west is reported below.

3.4.2 Bouguer gravity anomaly and Niggli Correction

The point-wise complete Bouguer gravity anomaly map shows a pronounced positive feature, that extends throughout the whole study area trending North-East to South-West (Figure 3.5a). The maximum anomaly amplitude varies along the crest line along strike, while the cross-strike extent above 0 mGal is ca. 30 km, decreasing gently to the East and steeply to the West.
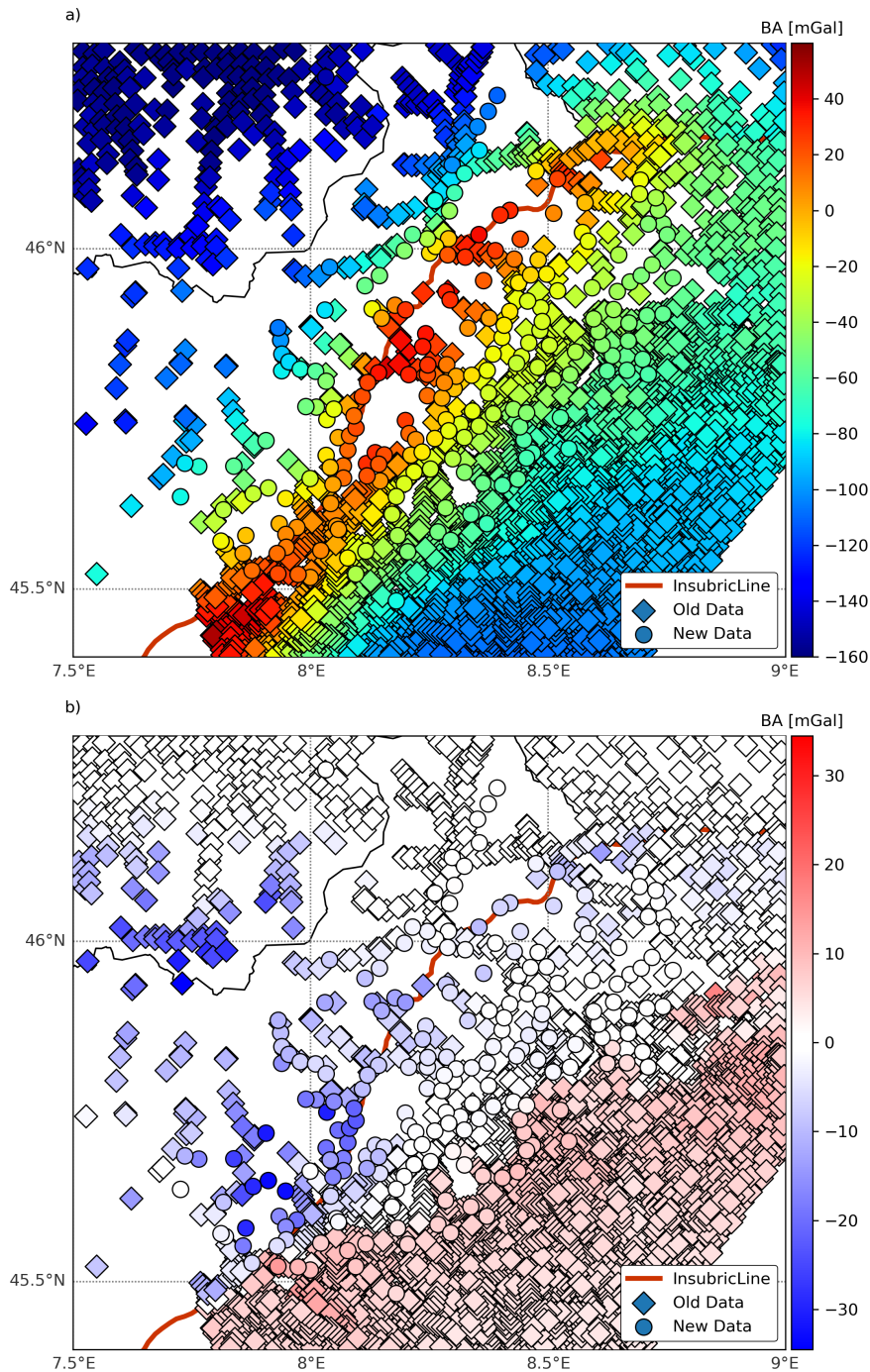
Figure 3.5 – (a) Point-wise Bouguer gravity anomaly (BA), computed from the currently avail-able merged gravity dataset. (b) Point-wise Niggli correction (NC), computed by taking into account mapped surface rock-densities in the terrain correction, as described in the text. This Niggli correction is negative in areas of denser rocks at the surface, and positive in areas of lighter rocks at the surface.

In the calculation of the complete Bouguer anomaly, the following classical equation is used:

$$BA = G_{obs} - G_0 - FA - BP - TC \qquad (3.1)$$

where G_{obs} is the observed gravity value, G_0 is the ellipsoidal gravity at the station location, FA is the free-air correction, BP is the Bouguer plate correction, and TC is the topographic correction. In equation 3.1, a constant and standard density value of 2670 $kg \cdot m^{-3}$ is considered both in the Bouguer plate and in the terrain correction terms. In order to consider the in situ rock densities as introduced and compiled above, both terms need to be corrected. The terrain correction will consider a 3D density model between topography and station elevation, and the Bouguer plate correction will consider the same 3D density model between the station elevation and sea-level. The amount of correction depends on the difference of local densities with respect to the standard 2670 $kg \cdot m^{-3}$. The values of the density-dependent corrections BP* and TC* compared to the standard corrections BP and TC are shown on Figure 3.6(a) and (b), and can reach ca. 40 and ca. 5 mGal, respectively.

We then define the Niggli correction (NC) as a term that considers the rock density-dependence between topography and sea level:

$$NC = (BP - BP^*) + (TC - TC^*) \qquad (3.2)$$

Adding this correction term NC to the equation of the Bouguer anomaly, we obtain the Niggli anomaly (NA)

$$NA = BA + NC = G_{obs} - G_0 - FA - BP - TC + NC \qquad (3.3)$$

In other words, the Niggli anomaly is a type of Bouguer anomaly where local rock densities have been taken into account for the Bouguer Plate and terrain correction terms:

$$NA = G_{obs} - G_0 - FA - BP^* - TC^* \qquad (3.4)$$

The Niggli correction is obtained by incorporating the surface density map in the same GRAVPROCESS routine that has been previously used to compute the Bouguer gravity anomaly. At the terrain correction stage, each triangle face of the surface mesh geometry, vertically extended downward until sea level, defines a volume unit. The topographic masses between surface and sea level are a compact ensemble of such volume units. The Bouguer anomaly is computed via summation of line integrals along the perimeter of every single volume unit and, thanks to the linearity of the problem, the Niggli correction can be defined by the same calculation, by multiplying each unit integral with the associated local density deviation from the reference value of 2670 $kg \cdot m^{-3}$. As a consequence, the Niggli correction is positive in the

areas with a lower surface rock density while it is negative in the areas of higher surface rock density.

While developing the 3-D crustal density model to explain the field observations, we will refer to and aim at reproducing the Niggli anomaly.

This allows us to simplify the definition of the model geometry in our approach described below, as we account for the shallow and complex structures mapped at the IVZ surface directly with the Niggli correction term. We consider the compiled surface rock-units as a first valid representation of the crustal complexity between the surface and the sea level in our study area. Hence, we eventually model the density distribution at depth only up to sea level, assuming in our model that the layer above sea level has already been accounted for based on the compiled surface rock-density map (Figure 3.4b). We note that the main features of the Niggli anomaly map are similar to that of the Bouguer anomaly map, but the local maxima reported by earlier studies (Figure 3.2) are either diminished in amplitude or vanished.
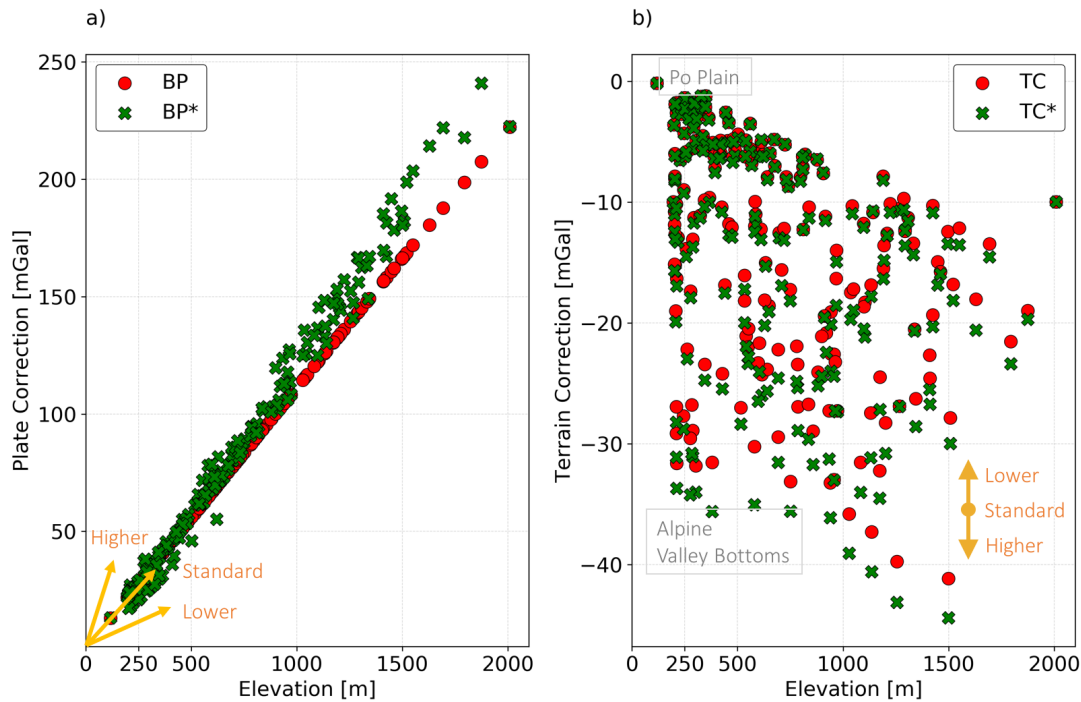
Figure 3.6 – Effect of considering in situ rock densities on gravity corrections, plotted versus elevation. (a) Bouguer Plate correction BP, with the standard constant value of $kg \cdot m^{-3}$ everywhere (red), and when considering the 3-D variation of densities (green). Yellow lines indicate the orientation of higher and lower density effects. (b) Terrain correction TC, with the standard approach (red), and when 3-D density variations are taken into account (green). Yellow legend indicates the trend of the effects caused by higher and lower density variations with respect to the standard value.

3.5 3-D density model construction

The crustal density model has been developed using the IGMAS+ software (Schmidt et al., 2010). This tool allows the creation of 3-D models using triangulated polyhedrons and/or triangulated grids, with the possibility of manipulating geometries and physical parameters such as density, susceptibility and magnetization. For this work, density and model geometry have been iteratively modified to reach an optimal fit to the data.

Here we present a 3-D crustal density model, defined by one single density–contrast interface with respect to a constant-density background, from 60 km depth up to sea level. Despite the reality being most likely closer to spatial density gradients, the sharp contrast of our model serves efficiently in fitting the pronounced gravity anomaly we observe, which would be increasingly complex and non-unique with broad density gradients. We therefore model the geometry of the interface defining the density contrast and the amplitude of the density jump itself, with respect to a given background. Therefore, the modelling is not constraining the absolute density values across the interface geometry, but only their difference. The initial model geometry is based on the regional Moho discontinuity map (Spada et al., 2013), locally modified to match the 7 km s–1 P-wave velocity contour surface from the local earthquake tomography model (Diehl et al., 2009), in the vicinity of the IGB gravity anomaly. The software package GeomIO (Bauville and Baumann, 2019) was used to interpolate the initial model interface on a 3 km by 3 km grid to serve as the input in IGMAS+. In order to develop this model to fit the gravity anomalies, we have assigned a target density contrast of 400 $kg \cdot m^{-3}$, which is consistent with what has been suggested by previous authors: 400 $kg \cdot m^{-3}$ by Berckhemer (1968), 350 $kg \cdot m^{-3}$ by Kissling et al. (1984), from 360 to 410 $kg\,m^{-3}$ from Bürki (1990).

Within the IGMAS+ workflow the input model geometry is interpolated and displayed over an ensemble of user-defined west–east cross-sections (10 km spaced from each other in north–south direction). We have left the far-field structure untouched and coincident with the Moho discontinuity map, constrained by previous studies (Spada et al., 2013). On the contrary, our geometry modifications focused on the IGB gravity anomaly and where the IGB is supposed to be more pronounced and extending towards the surface, presenting the iconic bird's head shape as suggested by previous investigations (e.g. Berckhemer, 1968).

At each modelling step, the user is free to modify either the geometry and/or the value of the associated model density contrast; the software displays the updated comparison between synthetic and observed data, allowing an immediate visual feedback.

In order to investigate the feasibility of a 400 $kg \cdot m^{-3}$ density–contrast model, we iteratively modified the geometry along each cross-section within our study area. At regular intervals between geometry modifications, we ran an automated inversion (available within IGMAS+ tools) which provides, at a given geometry, the density–contrast value minimizing the misfit between observed and synthetic data. We observed that a minimum of 5 rounds of geometry change and density contrast inversions were necessary to reach a stable solution with ca. 10 mGal RMS misfit, and beyond a few more iterations the user effect became important without obvious model updates.

For each small geometry modification, the inverted density contrast varied of small amounts:

ca. $\pm$ 10 $kg \cdot m^{-3}$ with respect to the previous iteration. This practice served as a step-by-step guide during the model development. In order to fit the positive gravity anomalies, our model geometry rapidly converged towards a gently E–SE dipping structure, similar to the ones reported in the literature (e.g. Kissling et al., 1984).

3.6 Results

3.6.1 Model geometry

The proposed reference model for the IGB presents a 400 $kg \cdot m^{-3}$ density–contrast interface, which is significantly closer to the surface than the initial model. The modelled structure is more than 10 km shallower in the areaswhere the anomaly is most pronounced, reaching as shallow as 1 km depth below sea level, which is also shallower than other proposals in the literature (e.g. 3 km by Berckhemer 1968). Given this density contrast, we require the IGB to be not only shallower but also to have a ca. 1.5–2 times wider neck than the earlier models (Berckhemer, 1968). However, we have no resolution to resolve the very thin beak of the bird's head proposed earlier. The neck width was not a well-constrained feature as only one side of it was seismically imaged (Figure 3.9d).

With this reference model,we reproduced the main features of the gravity anomaly across the IVZ in terms of maximum amplitude, east–west extension and along-strike variations (Figure 3.7). In the next section, we discuss the model sensitivity to the density contrast, showing how the geometry is modulated by the density variations with respect to the reference model.

Six east–west profiles were extracted from the model's target area for a more detailed comparison between observations and synthetics (Figure 3.8), presenting a satisfactory fit to the data in the areas where the anomaly is most pronounced. The far-field effects are less well-explained than the central area, most likely because of the thick sedimentary cover effects on the Eastern side of the study area (Po Plain) and other possible but much smaller density anomalies different from the IGB itself.

Along these profiles, the model misfit is defined as the RMS of the anomaly residuals, within an interval focused around the main peak for each west–east profile (Figure 3.8). This misfit definition omits the far-field residuals, which are not directly related to the IGB and are beyond the scope of this work. For this reference model, we have a RMS of ~7.5 mGal over the selected points and profiles of interest (Figure 3.8).

3.6.2 Model sensitivity

The 400 $kg \cdot m^{-3}$ density contrast of our reference model provides a satisfactory fit to the data (Figure 3.9a) and suggests a shallow structure that explain the gravity anomaly (Figure 3.9b).

However, very small modifications of individual vertices of the model geometry (on the order of a few 100 s of metres) and subsequent density–contrast adaptations are suitable to keep the fit to the data almost unchanged.

Hence, we have investigated the model geometry sensitivity with respect to the density–contrast values, in order to see how the model behaves when we deviate from the reference model 400 $kg \cdot m^{-3}$. We present end-member models, whose geometry have been developed starting from the reference model at two different density contrasts: a lower (300 $kg \cdot m^{-3}$) and a higher (500 $kg \cdot m^{-3}$) density–contrast model.

In both cases, we have modified the IGB structure in 3-D until a reasonable fit the data was recovered again (Figure 3.9c).While visually the fits seem to be acceptable, both models are slightly worse in terms of RMS misfit than our reference model. For example, for the profile shown in Figure 3.9: 5.23 mGal for the high, and 6.70 mGal for the low density–contrast model, compared to 4.23 mGal of the reference model.

Changing the density–contrast has consequences on the model geometry in both the lower and higher density–contrast cases (Figure 3.9d). The former requires the IGB to have an even wider neck and a shallower and wider head: the IGB head reaches and is limited by the virtual sea level, implying that 300 $kg \cdot m^{-3}$ represents the lower limit for the IGB density contrast. In this case, a broader density gradient instead of a single interface does not seem to be a realistic solution, as it would have difficulties explaining the sharp gravity anomaly shape. The high density–contrast model presents a narrower neck and a deeper top of the interface, located at ca. 2 km below sea level. In this case, the higher density–contrast is providing a sharp peaked gravity anomaly, suitable to fit the observations: we may obtain a plausible solution by distributing this density contrast across a few kilometres thick interface by using a spatial gradient, instead of a sharp contrast located at the interface boundary. We estimate this spatial gradient to be up to 4 km thick.

Nevertheless, all three tested models require a shallow-lying anomalous structure with a somewhat sharp density contrast to explain the observed gravity data. This range of possible density contrasts is directly usable for petrological modelling of the IVZ (Pistone et al., 2020). Furthermore, in order to test the user uncertainty and the effect of non-uniqueness in gravity modelling on our work, we developed two other end-member models with higher and lower density contrasts (500 and 300 $kg \cdot m^{-3}$, respectively), this time starting directly from the initial structure, and not from the reference model solution. In both cases, we reached the same order of- magnitude RMS of previous models and the same main results: the IGB being thinner and further away from surface in the higher density case and thicker and closer to surface in the lower density case. During these tests, it became clear that near-surface points are better constrained from the gravity measurements, and the constraints are looser at depth. Given our data set's resolution ability (about 1 gravity point per 4–9 km^2 and at ca. 1 mGal uncertainty), the horizontal position of the IGB neck is resolved at <5 km on either side, and the vertical position of the IGB head-top is resolved at ca. 1 km, depending on the chosen density contrast.
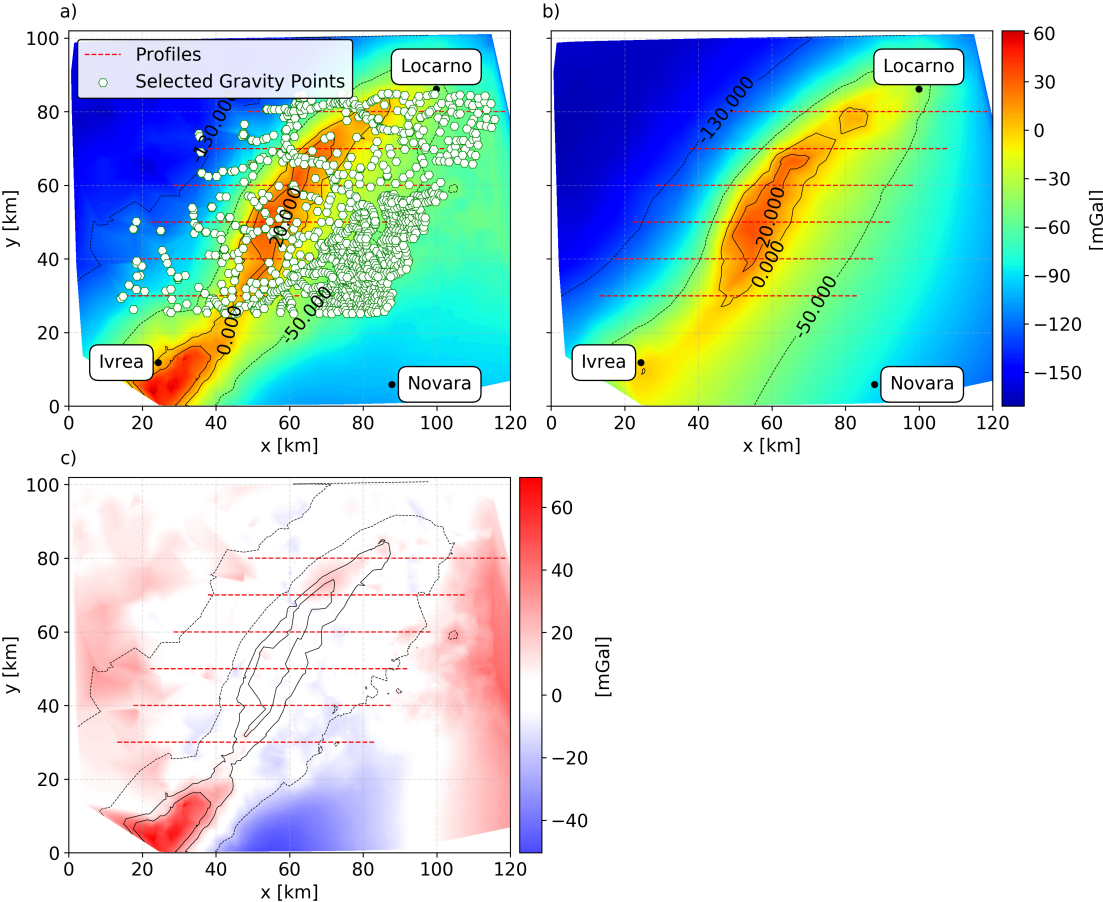
Figure 3.7 – Gravity data and model. (a) Observed Niggli gravity anomaly, interpolated over the study area. Selected gravity data points along six west–east oriented profiles serving for the comparison with the model across the most pronounced anomaly are highlighted. (b) Interpolated synthetic gravity effect, obtained from 3-D density modelling (see text for details). The same west–east profile locations are given as a reference. (c) Misfit map, obtained by subtracting the synthetic Niggli gravity anomaly from the observed one.
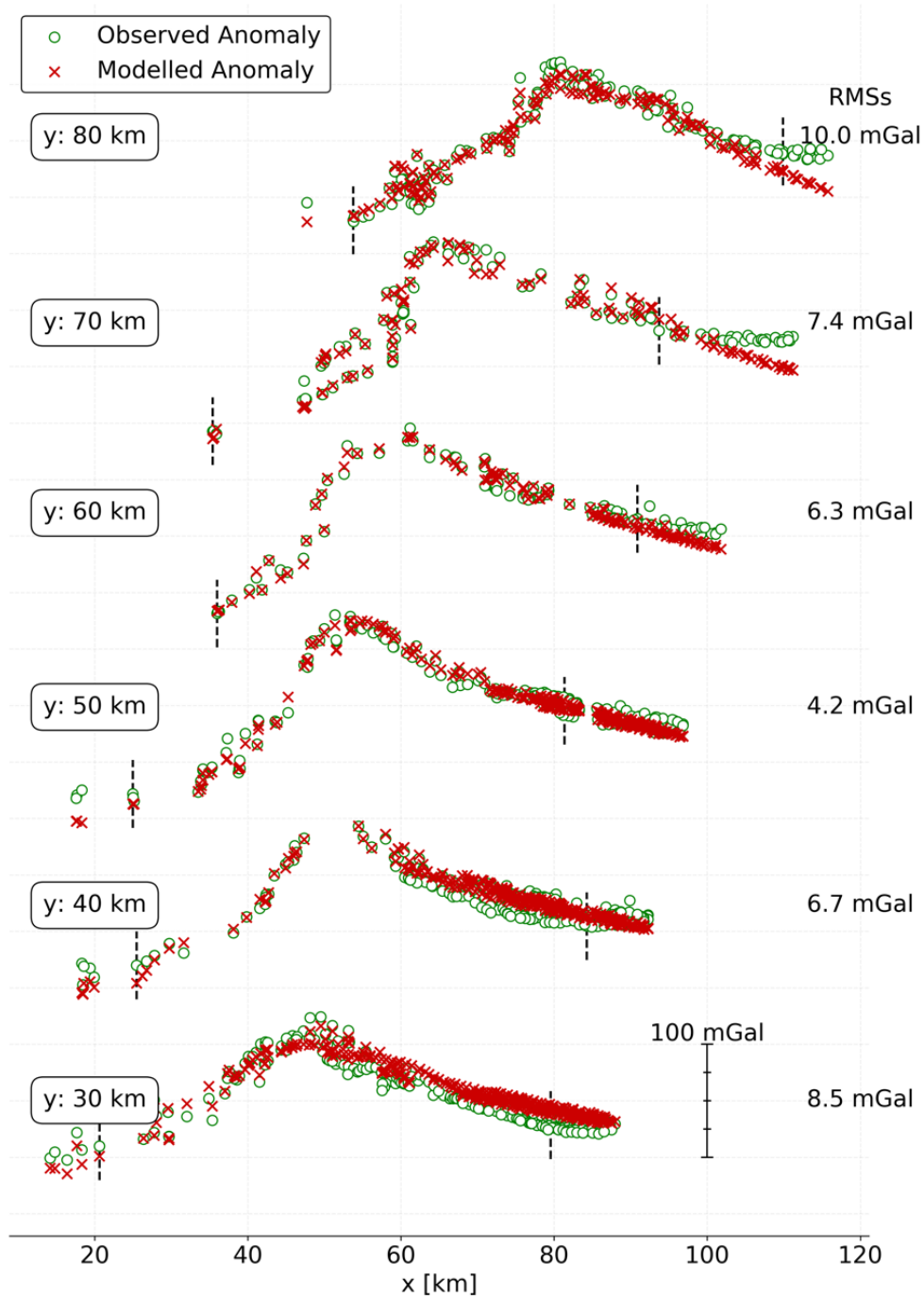
Figure 3.8 – Comparison between observed Niggli gravity anomaly and the corresponding synthetic model's effect along the six west–east oriented profiles presented in Figure 3.6. Profile locations are given on the left-hand side. For each profile, gravity points within 5 km distance on both sides have been considered. The mGal scale is valid for all six profiles, shown in an offset way. The RMS misfit has been computed around the main peak, between the two vertical black dashed lines.

3.7 Discussion

The effect of the Niggli gravity anomaly correction (Figure 3.5b) is not negligible when it comes to study areas with such complex surface geology as the rocks of the IVZ (Figure 3.4). In our study area, the Niggli correction flattens certain local maxima of the Bouguer gravity anomaly (in particular the ones located close to denser rock units) and it shifts the main gravity anomaly crest-line to the east, as an effect of accounting for denser and high elevation (i.e. thicker) rock units on the western side of our domain (e.g. units 1, 3 and 13).

Still, the model presents some limitations beyond the inherent non-uniqueness of gravity modelling and potential field methods in general, which could be addressed in future works, using other geophysical data such as receiver functions analyses, allowing for seismic discontinuity mapping and additional geometry constraints.

Here below we address the limitations of the proposed 3-D density model. Regarding the amplitude of the Niggli correction, some uncertainties affect the computation itself due to the uncertainty in the single mineral-density estimates as solid solution end-members which differ substantially for pure Mg and Fe end-members. This is the case for olivine, pyroxenes and garnet (Table 3.1), where mineral density variations can change by few hundreds of $kg \cdot m^{-3}$ depending on the chemical composition. However, on average for a given rock, and ranging through different mineral end-members, typical density variations are on the order of ten to a few tens (and up to a maximum of 100) $kg \cdot m^{-3}$ of the final rock density. The density extrapolation to whole unit density may be affected by the same order-of-magnitude uncertainty, if one was to explore all the possible combinations of mineral abundances and rock proportions. Nevertheless, 100 $kg \cdot m^{-3}$ is estimated as a conservative and safe upper bound for the uncertainty related to unit density association. As an example to quantify the effect of mineral density uncertainties on the observed gravity anomaly, we computed the Niggli correction of a middle-sized, middle-elevation unit in the centre of our study area (i.e. the IIDK unit, identified by number 3 in Table 3.1 and Figure 3.4a), with a 100 $kg \cdot m^{-3}$ density change of the whole unit with respect to its own reference density. The associated Niggli correction variation at a gravity point nearby is ~2.7 mGal, which is compatible with the scopes and below uncertainties of our modelling work.

Another limitation stems from the model geometry itself. The 3-D crustal structure is built by working on parallel cross-sections which are 10 km apart from each other, not allowing for much smaller details or for single unit bodies to be modelled in detail (e.g. Balmuccia peridotite unit, extending N–NE to S–SW with ~4 km length and 1 km width). Also, the single-interface model is not able to capture possible density variations along strike of our study area, as only one density contrast value is used for the IGB. However, the choice of the single-interface modelling approach captures the main signal related to the IGB. Finally, the user effect in the construction of the model involves spatial ambiguities and flexibility below the kilometre scale. The main features such as the shallow-lying anomaly, the steeply E–SE dipping body, and the arcuate shape in map view of the IGB are well constrained.

The proposed model suggests 300 $kg \cdot m^{-3}$ as a possible lower bound for the density contrast associated with the IGB with respect to the surrounding lithologies, which would not fit the

observations if distributed across a broad vertical gradient instead of a sharp interface. Hence, assuming a standard (upper crustal) background density of 2670 $kg \cdot m^{-3}$ our model requires the IGB composing rocks to be at least 3000 $kg \cdot m^{-3}$. Such a density may point to both mafic and high-grade felsic metamorphic rocks commonly documented in middle to lower continental crust (e.g. gabbro, stronalite, kinzigite; Hacker et al., 2015). However, the limit of ~3000 $kg \cdot m^{-3}$ should be regarded as a minimum density for the rocks composing the IGB. Indeed, the density model would equally fit the observed data if there was the same crustal background density increase with depth in the whole model instead of a uniform constant one. The assumption of such a gradient is closer to reality: the present-day lower continental crust is likely made of mafic rocks and/or high-grade metamorphic rocks (Bois et al., 1989; Fountain, 1989; Rey, 1993; Schmid and Kissling, 2000; Hacker et al., 2015). This implies that we can expect the background crustal density to reach ~3000 $kg \cdot m^{-3}$ above the Moho. Keeping the same density contrast of the IGB of 300 $kg \cdot m^{-3}$ along the model interface would imply that, in turn, the density of the IGB is 3300 $kg\,m^{-3}$ at its root, which is a ~30 to 40 km depth below IGB head. Such a density for the IGB would exclude felsic rocks (Hacker et al., 2015) and rather point either to mafic rocks that underwent high pressure metamorphism (eclogites; Aoki and Takahashi, 2004), ultramafic plutonic rocks such as pyroxenites or garnet hornblendites (e.g. Müntener and Ulmer, 2006) or mantle peridotites.

Geological arguments can help to sharpen the lithological composition of the IGB. The IGB gravity anomaly is bounded to its western side by the Insubric Line (Figure 3.4), as underlined by with the 0 mGal anomaly contour line (Figure 3.5b). Both geological (Schmid et al., 1987, Schmid et al., 1989; Berger et al., 2012) and near-surface geophysical arguments (Greenwood et al., 2018) indicate that the Insubric Line is a crustal scale, subvertical to vertical structure: this implies that the IGB structurally belongs to the Southern Alps. While common in the Western Alps, Alpine high-pressure metamorphic rocks are unknown in the Southern Alps, as these are mostly dominated by high-temperature metamorphic rocks. This makes high-pressure metamorphic rocks (eclogites) a rather unlikely lithology for the IGB. In consequence, plagioclase poor, ultramafic plutonic rocks or mantle peridotite appear as the main candidate for the composition of the IGB.

These considerations remain valid for higher values of IGB density contrast: the preferred 400 $kg \cdot m^{-3}$ model, and also our model's upper limit at 500 $kg \cdot m^{-3}$. Such scenarios would require to have mafic IGB rocks at shallower depth, and to have mantle density at the root of the IGB.

Additional field observations and a wider study area with more detailed geological considerations would be necessary to investigate in further detail the broader surroundings of the IVZ, such as the Sesia Zone and the Po Plain sedimentary basin. However, the conclusions on the dominant gravity anomaly of the IGB in relation to the rocks exposed in the IVZ remain valid. These results are also mutually valuable in the perspective of forthcoming projects in the same area such as the DIVE project (Drilling the Ivrea Verbano zonE; Pistone et al., 2017), which would provide additional joint geophysical and petrological investigations across scales in the IVZ.

Finally, the new constraints on the density, shape and total volume of dense IGB rocks in the

IVZ call for investigating how such rocks could have been emplaced at shallow depth. Detailed geological observations coupled to 3-D thermomechanical modelling, with appropriately selected physical parameters (density, rheology) may shed light on the involved mechanisms, and may help to understand why other deep-crustal section are exposed but remain rare on the continents.

3.8 Conclusions

We have integrated a newly compiled gravity database with 207 new gravity points we measured across the IVZ, in order to investigate the IGB at higher resolution and in a novel way. By defining the Niggli anomaly, we have incorporated the geological surface observations from the field into the geophysical investigations in form of an adapted density correction, bridging across different spatial scales, from regional gravity anomaly trends to laboratory rock sample analyses.

The result is a 3-D single-interface crustal density model of the IGB,which presents an optimal fit to the observed data at $400 \ kg \cdot m^{-3}$ density contrast with respect to its environment. The model result supports a dense body with a structure located close to surface, with new constraints suggesting 0–2 km depth below sea level.

The modelling procedure highlights the need for a shallow and pronounced density contrast or spatially sharp (<4 km) density gradient in order to fit the observations. The range of plausible density contrasts is between 300 and $500 \ kg \cdot m^{-3}$, with the preferred model at $400 \ kg \cdot m^{-3}$. Considering a natural increase of densities with depth, and the metamorphic grade of rocks in the area, felsic and high-pressure metamorphic rocks (eclogites) were excluded as main composing rocks if the IGB. Instead, mafic or ultramafic plutonic rocks are most likely for the lithology of the IGB.

Further efforts will be spent to investigate the structure beneath the IVZ, especially by jointly analysing gravity and seismological data we have collected in the same region. Starting in 2017, 10 broad-band seismic stations have been installed along a west– east profile across the IVZ and have continuously recorded seismic data for 2 yr (https://doi.org/10.5281/zenodo.1038209). The seismic data will be processed by the receiver function method in order to investigate seismic discontinuity locations and sharpness, and the seismic crustal structure. The joint use of gravity and seismic data will put new constraints on the IGB geometry and on its physical properties. This, in turn, will provide useful input for geological and numerical models exploring the emplacement of deep-crustal bodies at shallow depth, which may explain the mechanism and relative rareness of Ivrea-type outcrops across the globe.
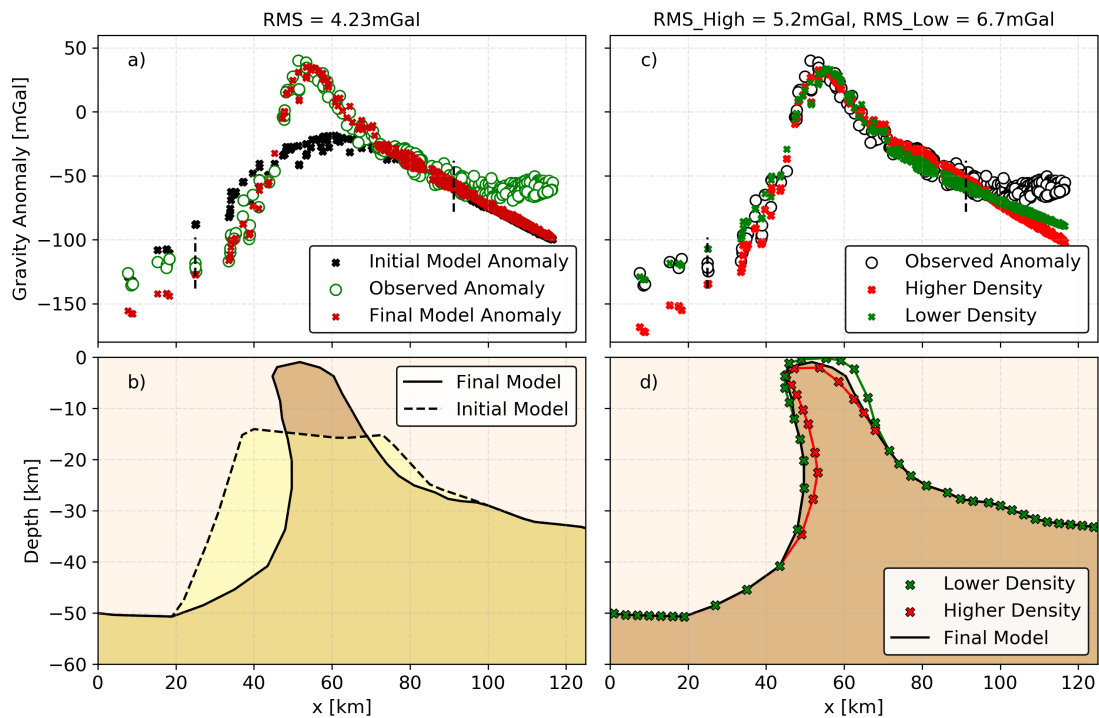
Figure 3.9 – West–east gravity profile and corresponding density model cross-section at y = 50 km across the study area. (a) Observed and modelled Niggli gravity anomaly. The RMS misfit has been computed around the main peak, between the black dashed lines. (b) Respective crustal density model cross-section using a 400 $kg \cdot m^{-3}$ density–contrast interface, in comparison with the initial model defined by the 7 kms–1 Vp contour from local earthquake tomography (dashed line). (c) and (d) Same profile but use a lower (300 $kg \cdot m^{-3}$) and a higher (500 $kg \cdot m^{-3}$) density contrast to explore the sensitivity of the model geometry. See main text for more details.

3.9   Acknowledgements

version.

4 Joint seismology-gravimetry inversion of the Val Sesia profile

In this chapter I present the 2D seismic and gravity joint investigation I performed, to model the Ivrea geophysical body along the Val Sesia West-East linear profile.
Its content has been published in the following article:

4.1 Summary

We present results from a joint inversion of new seismic and recently compiled gravity data to constrain the structure of a prominent geophysical anomaly in the European Alps: the Ivrea Geophysical Body (IGB). We investigate the IGB structure along the West-East oriented Val Sesia profile at higher resolution than previous studies. We deployed 10 broadband seismic stations at 5 km spacing for 27 months, producing a new database of ~1000 high-quality seismic receiver functions (RFs). The compiled gravity data yields 1 gravity point every 1-2 km along the profile. We set up an inversion scheme, in which RFs and gravity anomalies jointly constrain the shape and the physical properties of the IGB. We model the IGB's top surface as a single density and shear-wave velocity discontinuity, whose geometry is defined by four, spatially variable nodes between far-field constraints. An iterative algorithm was implemented to efficiently explore the model space, directing the search towards better fitting areas. For each new candidate model, we use the velocity-model structures for both ray-tracing and observed-RFs migration, and for computation and migration of synthetic RFs: the two migrated images are then compared via cross-correlation. Similarly, forward gravity modelling for a 2D density distribution is implemented. The joint inversion performance is the product of the seismic and gravity misfits. The inversion results show the IGB protruding at shallow depths with a horizontal width of ~30 km in the western part of the profile. Its shallowest segment reaches either 3-7 or 1-3 km depth below sea-level. The latter location fits better the outcropping lower crustal rocks at the western edge of the Ivrea-Verbano Zone. A prominent, steep eastward-deepening feature near the middle of the profile, coincident with the Pogallo Fault Zone, is interpreted as inherited crustal thickness variation. The found density and velocity contrasts of the IGB agree with physical properties of the main rock units observed in the field. Finally, by frequency-dependent analysis of RFs, we constrain the sharpness of the shallowest portion of the IGB velocity discontinuity as a vertical gradient of thickness between 0.8 km and 0.4 km.

4.2 Introduction

The geologically defined Ivrea-Verbano Zone (IVZ) and the related but much longer Ivrea Geophysical Body (IGB) belong to the most outstanding features of the whole Alpine domain. They have been the subject of numerous international investigations in the fields of geology, petrology and geophysics (e.g. Schmid et al., 2017, Petri et al., 2019, Kissling et al., 1984 and detailed references below).

The western end of the Southern Alps (Figure 4.1a) is regarded as a nearly complete cross-section of the continental crust, exposing upper to middle and middle to lower crustal composition rocks at its surface in the Serie dei Laghi and the IVZ, respectively (e.g. Fountain, 1976; Khazanehdari et al., 2000). These units belong to a complex tectonic setting, which has been mapped by several groups of authors (e.g. Brack et al., 2010; Petri et al., 2019; Schmid et al., 2004).

This work focuses on the IGB, which constitutes the crustal root of the IVZ and consists of an

anomalously dense and seismically fast rock complex. This anomalous crustal complex extends along the whole inner arc of the Western Alps and outcrops in its north-eastern portion as the IVZ. The IGB is nowadays regarded as a sliver of the Adriatic lower lithosphere (e.g. Petri et al., 2019; Schmid et al., 2017), which was involved in the Alpine collision and tectonically emplaced at unusual shallow depths (e.g. Handy et al., 2015). The Adriatic plate, among other micro-plates, was one of the key actors in the Alpine collision and the related orogenic process, which featured the subduction of the former Tethys ocean and the subsequent Adriatic thrusting against the European margin (e.g. Handy et al., 2010). The IGB is associated with pronounced seismic, gravity and magnetic anomalies (e.g. Diehl et al., 2009; Kissling et al., 1984; Lanza, 1982). The IGB is bounded by the Western Alps along the Insubric line (IL): a main vertical to sub-vertical fault line (Berger et al., 2012; Schmid et al., 1989; Schmid et al., 1987) which separates the Adriatic plate from the orogenic wedge (Figure 4.2a).
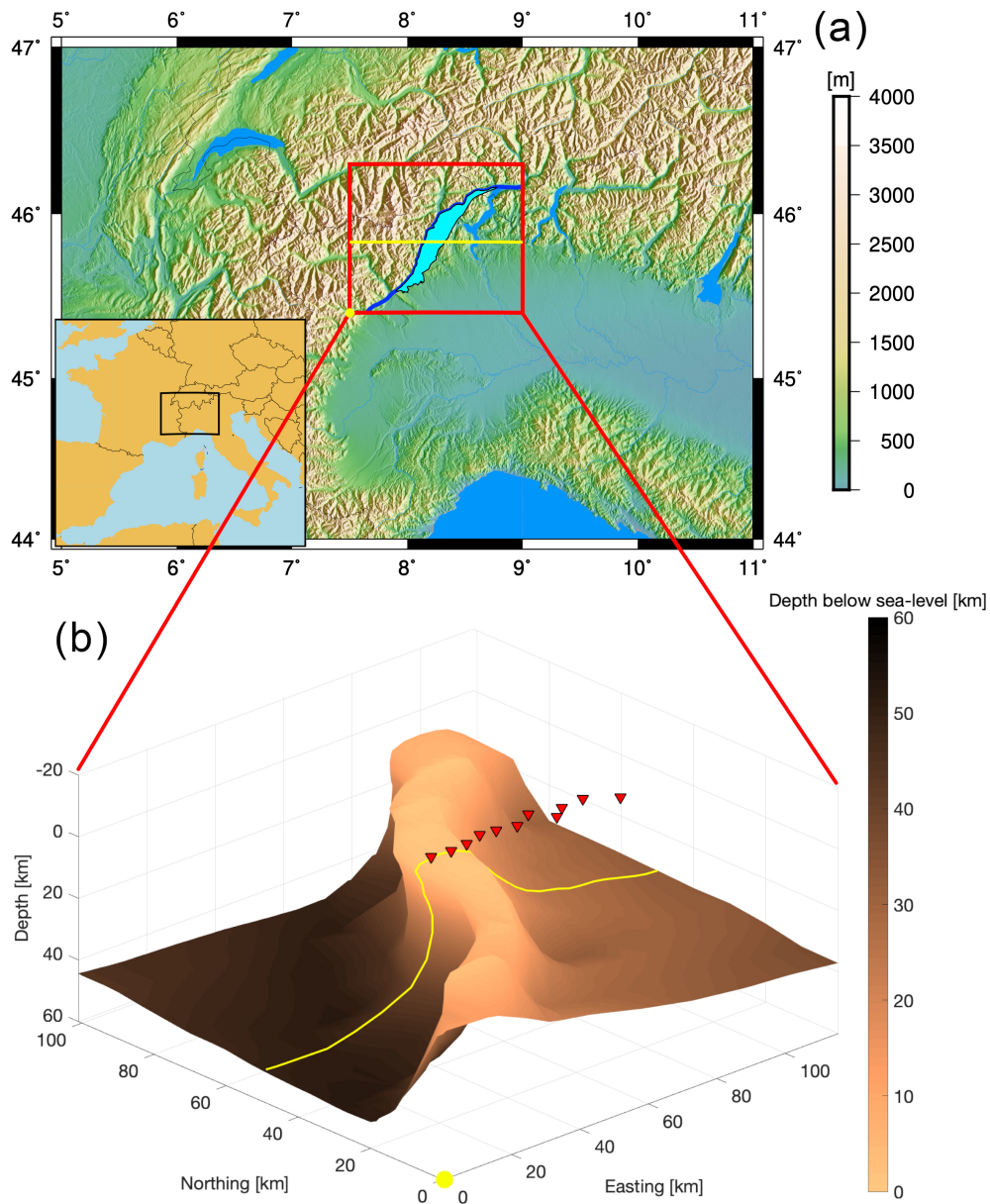
Figure 4.1 – Study area and the Ivrea Geophysical Body. Bottom: perspective view of the IGB 3D density model interface constrained by gravity data modelling in an earlier study (Scarponi et al., 2020). The 2D cross-section investigated in this study, along the 2D West-East IvreaArray seismic profile (red triangles), is highlighted by a yellow line. This target profile extends across the IVZ (cyan shape on map), delimited on the West by the Insubric Line (blue line). The yellow circle is the origin of the km-coordinate system used in this study and the subsequent figures (7.5E long., 45.4N lat.). The inset show the overview map's location in Europe.

A long history of investigations has addressed the IGB, both in terms of gravity mapping (e.g. Masson et al., 1999; Niggli, 1946; Vecchia, 1968) and gravity data modelling, with models based on continuous bodies with a sharp and constant density contrast (e.g. Berckhemer, 1968;

Kissling et al., 1984), and on heterogeneous-size and -density blocks as well (e.g. Bayer et al., 1989; Bürki, 1990; Rey et al., 1990). Concerning seismic investigations, the IGB was first imaged by refraction experiments (Ansorge et al., 1979); Berckhemer, 1968), which lead to the birth of an iconic model, usually referred to as the "Bird's Head" in the literature. This became of historical value with subsequent investigations, revealing high level of structural complexities of the IGB (e.g. Ansorge et al., 1979). In the frame of the ECORS-CROP experiment, the regional crustal structure was investigated via reflection seismics (e.g. Bayer et al., 1989; Nicolas et al., 1990; Thouvenot et al., 1990), guiding the development of several 2D gravity models but also stressing the limitations of controlled-source seismology, in imaging such a complex structure as the IGB (Kissling, 1993). Local earthquake analysis and tomography (LET) studies (e.g. De Franco et al., 1997; Diehl et al., 2009; Solarino et al., 2018) allowed the IGB to be better imaged and interpreted in light of the tectonic setting as well (Schmid and Kissling, 2000). Despite the latest advances in the terms of LET resolution (Diehl et al., 2009 provides the crustal vP structure on a 25 x 25 x 15 km grid and Solarino et al., 2018 locally higher, up to 15 x 15 x ~ 10 km), a spatial imaging gap persists between the IGB structure at the geological maps' spatial scale. Therefore, structural questions on the IGB's relation with the exposed IVZ remain open.

Recent gravity investigations, based on new, densely spaced gravity surveys and earlier-existing compiled gravity data (Figure 4.2b) allowed the development of a new 3D IGB gravity model across the IVZ area (Scarponi et al., 2020; Figure 4.1b). In this work, we focus on a central cross-section of this most recent 3D IGB model (Figure 4.1b) and we integrate the gravity dataset with new high-resolution broad-band passive seismic data, recorded during the IvreaArray passive seismic experiment (Hetényi et al., 2017). We intend to use the new seismic data to further constrain the most recent IGB 3D density model along the IvreaArray profile (Figure 4.2b). In fact, we investigate the West-East oriented 2D profile along Val Sesia (~45.83N lat.), crossing the entire IVZ at that latitude (~8.11E to 8.77E). We model the IGB along this 2D cross-section as a body below a single discontinuity, and set up a joint inversion scheme to fit the observed gravity anomaly and seismic receiver functions (RFs) from IvreaArray, to constrain both the shape and the physical properties of the IGB. The RF technique enhances smaller-amplitude P-to-S (Ps) converted phases in the P-wave coda, and extracts information on the Earth discontinuities beneath a seismic receiver (Langston, 1979). While RF inversion is routinely performed to investigate the seismic properties of the crust and the upper mantle (Bodin et al., 2012), inverting the RFs-only is in general a strongly non-linear and non-unique problem (Ammon et al., 1990). Joint inversions of RFs along with complementary geophysical observations reduce this non-uniqueness. Such complementary data sets can be, e.g., RFs and surface wave dispersion curves (Julia et al., 2000), also with the addition of magnetotelluric data (Moorkamp et al., 2010) or RFs combined with gravity data and seismic tomography (Basuyau and Tiberi, 2011).

Here, we implement a novel iterative joint inversion algorithm, acting on the gravity and seismic data. This algorithm is meant to explore and characterise the performance of all considered IGB models in non-probabilistic terms, by implementing a performance-driven pseudo-random walk in the model space. The gravity anomaly along the profile and the

computed seismic RFs represent our observations. In particular, we combine the sensitivity of gravimetry to the geometry and magnitude of density contrasts in the subsurface structure, with the sensitivity of RFs to the crustal discontinuities beneath the seismic receiver.
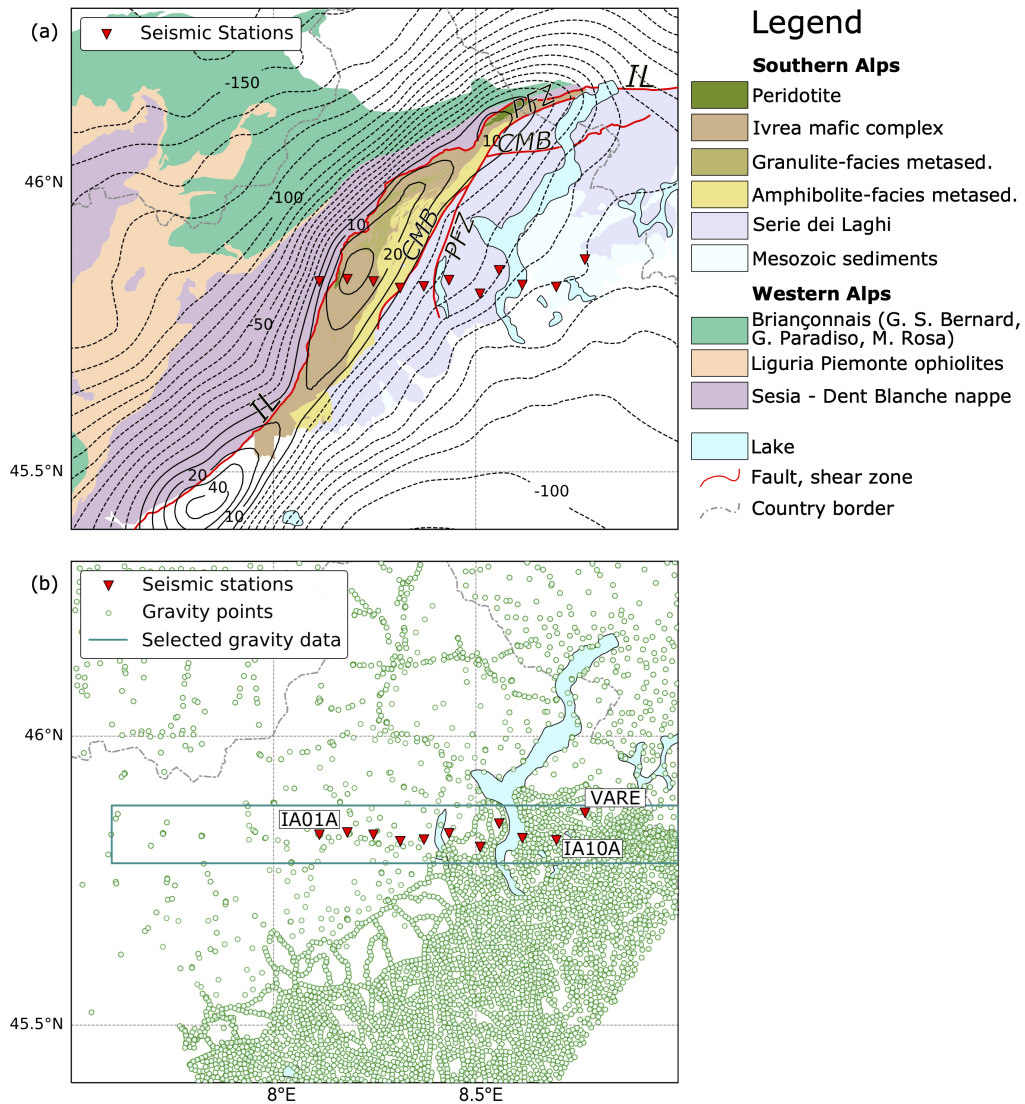
Figure 4.2 – (a) Geological map of the IVZ and the surrounding areas, simplified from Petri et al. (2019) and Schmid et al. (2004) (see legend on the right hand of the figure), together with the location of the 10 IvreaArray broadband seismic stations and the INGV permanent seismic station IV.VARE (red triangles, see station names in panel (b)). The main faults (red lines), relevant for this study, are indicated as "IL" for Insubric Line, "PFZ" for Pogallo Fault Zone and "CMB" for Cossato-Mergozzo-Brissago Line. Overlaid, the 10 mGal contour lines for the Bouguer gravity anomaly from our data across the study area. (b) The compiled gravity data set for this study is shown (green circles), which comprises earlier existing gravity data and recently collected gravity data in the scope of the work of Scarponi et al. (2020). The location of the IvreaArray seismic stations is shown (red triangles) together with the INGV permanent seismic station IV.VARE and their names. The cyan box indicates the gravity data we selected for this study along the 2D IvreaArray profile. The dashed-pointed grey line indicates the Swiss-Italian border as shown in the legend.

4.3   Data and data products

New seismic data has been acquired and recent gravity data has been compiled to produce a higher resolution image of the IGB along the Val Sesia profile. The following paragraphs present how the data was obtained and processed prior to the joint inversion. The complete seismic dataset is directly available in the supplementary materials, in the form of radial (RRF) and transverse (TRF) seismic receiver functions.

4.3.1   The IvreaArray seismic network

We collected the new seismic data in the framework of IvreaArray (Hetényi et al., 2017): a temporary seismic network, installed and operated for 27 months (June 2017 to September 2019) as one of the AlpArray complementary experiments.
The main purpose of IvreaArray was to record high-quality seismic signals at a higher spatial resolution in Val Sesia, compared to earlier studies addressing the crustal structure in the Western Alps and in the IVZ.
For this purpose, we deployed 10 broadband three-component seismic stations at 5 km spacing along a West-East linear profile (~45.83E lat.). The INGV permanent seismic station IV.VARE is included as it located as a natural eastern continuation of IvreaArray (Figure 4.2b). All 10 deployed sensors were the Güralp CMG-3ESP seismometers of the Czech MOBNET pool, with 60 sec lower corner frequency. The linear seismic profile crosses the entire IVZ. It starts few km to the west of the IL at ~8.11E long. (in the village of Boccioleto), then crosses the lower and middle crustal rocks outcropping in the IVZ and extends to the eastern shore of Lago Maggiore (~8.77E long.).
The seismic network operated for 27 months and continuously recorded data at 100 Hz sampling rate on all three components. Data recovery was ~90 per cent. During this time and according to the USGS earthquake catalogue, we selected and retrieved 347 events of interest for our study (magnitude ≥5.4, epicentral distance 28≤ Δ ≤95, appendix A.1).

4.3.2   Seismic receiver functions

We process the recorded teleseismic signals by computing seismic receiver functions: a deconvolution-based technique which enhances the arrival of P-to-S (Ps) converted phases (Langston, 1979). Ps converted phases follow the direct P-wave arrivals. They are produced when an impinging P-wave encounters a discontinuity – an impendence contrast – in the propagating medium beneath a seismic receiver, thus containing information on the associated Earth structure. A receiver function is mathematically defined as the deconvolution of the seismogram's vertical component from the radial component, yielding a series of delay times with respect to the first P-wave arrival (Langston, 1979. This operation removes the event source time function and the distant-path effects from the trace, favouring a constructive stacking to investigate the receiver side Earth structure. The analysis of the Ps delay times and

amplitudes carries information on the depth of a seismic discontinuity and the shear-wave velocity vS profile, together with the magnitude of the impedance contrast itself, with a primary sensitivity for the vS contrast.

We compute RFs based on the time-domain iterative deconvolution technique (Ligorría and Ammon, 1999) by iteratively cross-correlating the vertical and the horizontal (radial) seismic traces and saving the associated delay times, generated by the strongest amplitudes first and by the minor ones later on. The final RF is obtained via convolution of the spike train with a Gaussian pulse, whose width corresponds to the maximum allowed frequency into the seismic signal during pre-filtering.

In our case, we filtered the seismic data in the 0.1Hz to 1Hz frequency band and performed 150 iterations during deconvolution for each RF. Quality control (QC) is applied both on the seismic traces and on the final RFs. First, we look for amplitude similarity for each seismogram component across all the stations for each seismic event, and for teleseismic signal prominence with respect to the background noise. Then, for each computed RF, we verify an acceptable location of the reference direct-P wave signal and for its satisfactory recovery in terms of amplitude. We refer the reader to the work of e.g. (Hetényi et al., 2018; Hetényi et al., 2015; Subedi et al., 2018) for further description of this QC practice. This ensured retrieval of high-quality earthquake signal (in the original seismogram components) and of the direct-P arrival (in the computed RF) prior to the converted phases, providing a final dataset of ~1000 high-quality RF traces. The original seismic traces were rotated into the LQT, ray-based coordinate system. This practice allows us to maximise the Ps amplitude and to prevent the direct-P signal from strongly interfering with the peaks' interpretation in case of very shallow interfaces, which are expected in the IVZ. The distribution of all available RFs shows a strong variability in the peak polarities and delay times as a function of the back-azimuth (appendix A.2), in particular between the traces coming from the East and the West, which hints at the presence of dipping interfaces. In fact, dipping interfaces and/or anisotropic layers can affect the signal polarity and introduce back-azimuthal periodicities, especially on the transverse RF component (e.g. Levin and Park, 1997). By inspecting all the transverse RF signals from the IvreaArray recordings, we could find some but limited evidence for local dipping structures, but no clear signs of resolvable anisotropy at any of the stations, and therefore decided not to address this particular feature in the subsequent analysis.

Relative to the RF complexity, reverberations cause so-called multiples and small-scale heterogeneities can increase noise. Furthermore, as RFs record delay times, there is a trade-off between layer thickness and average vP/vS, which prevents from uniquely inverting for the Earth structure by using RFs Ps phases only (e.g. Ammon et al., 1990).

To address these limitations, and to avoid stacking numerous waveforms sampling a heterogeneous crust in the IVZ, we migrate the observed RFs from time to depth and produce migrated profiles. During migration, we perform ray-tracing for each station–event pair with a vertical resolution of 0.25 km using a 2D velocity model and respecting Snell's law including local interface dip. Then we distribute the RF time sample amplitudes along these ray paths to finally obtain a migrated image, with a final spatial resolution of 0.5 km. The migration spatially re-distributes wave conversions to where they were produced, and gives a structural image

of the sub-surface. The areas where the RF amplitudes are stacked constructively represent either an increase or a decrease of seismic velocity with depth. Figure 4.3b shows an example for the 1D iasp91 velocity model (Kennett and Engdahl, 1991).

While the observed RFs constitute the seismic part of the input to the joint inversion scheme, the computation of RF migration images is incorporated into the iterative inversion procedure, and constitutes the actual mean for the model seismic performance evaluation. The detailed description of the inversion workflow is provided in paragraph 3.
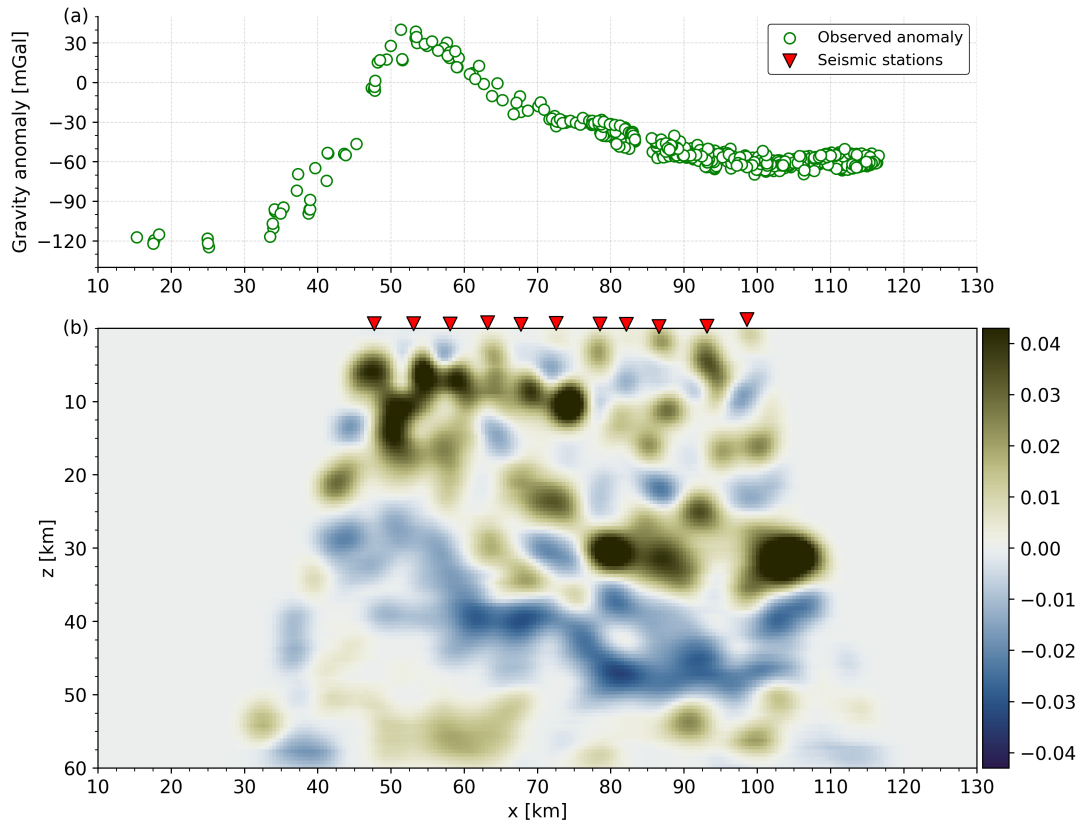
Figure 4.3 – (a) Niggli gravity anomaly computed from observed data and applying rock-density-based terrain corrections (Scarponi et al., 2020) along the West-East IvreaArray profile. (b) An example of migrated receiver function profile with the use of the IvreaArray and VARE seismic data and the iasp91 velocity model for ray-tracing and migration. Colours highlight areas of increasing (brown) and decreasing (blue) seismic velocities with depth. Migration colormap from Crameri (2018).

4.3.3   Gravity anomaly along Val Sesia

We compiled a gravity dataset by merging earlier and the most recent gravity data acquired across the IVZ. The earlier existing gravity data points were compiled from the Swiss Federal Office of Topography (Swisstopo: https://www.swisstopo.admin.ch/) and from the Istituto

Nazionale di Oceanografia e di Geofisica Sperimentale (OGS: https://www.inogs.it/), and were merged with the most recent data set in our earlier work (Scarponi et al., 2020). The full dataset was analysed in the same work (Scarponi et al., 2020), where the original raw relative gravity measurements were processed and transformed into absolute gravity values with the software GravProcess (Cattin et al., 2015), with a final mean uncertainty of 0.22 mGal (1 Gal = 1 $cm \cdot s^{-2}$). The reader is referred to the work of Scarponi et al., 2020 for full details of the gravity data acquisition practices and processing. In our joint inversion, we use a subset of this data (Figure 4.2b). The compiled dataset reaches a coverage of 1 gravity point every 1 to 2 km along the Val Sesia profile. For the joint inversion presented here, we include all the gravity points up to 5 km to the North and to the South along the IvreaArray seismic profile (Figure 4.2b). As the gravity data points were not uniformly distributed along the IvreaArray profile, we binned the data at 2 km intervals along the profile, obtaining a more balanced spatial distribution and allowing for faster gravity data modelling (0.08s instead of 1s for each test model). For each interval, the considered gravity data points were averaged in location (x and z coordinates) and in the measured gravity anomaly, with mean standard deviation of 3 mGal across the whole profile (appendix A.6).

The final gravity data product we use in the inversion of this study is the Niggli gravity anomaly, which is an improved Bouguer anomaly considering surface rock densities for the terrain and plate corrections (Scarponi et al., 2020). This anomaly is obtained by the classical correction of the absolute gravity values for the effect of homogeneous and constant-density 3D topographical masses (i.e. Bouguer plate correction and terrain correction with = 2670 $kg \cdot m^{-3}$), accounting for the density variations of rocks seen at the surface and extrapolated down to sea-level (i.e. the Niggli correction), which is well justified by the general IVZ vertical structure (e.g. Fountain, 1976; Khazanehdari et al., 2000).

Considering the Niggli gravity anomaly (henceforth simply gravity anomaly) as final gravity observation allows us to focus our modelling effort on the IGB crustal structure below sea level and to analyse it consistently together with seismic RF migration images (Figure 4.3).

4.4 Inversion approach

To reduce the non-uniqueness of RF-only inversion (Ammon et al., 1990), which are sensitive to sharp discontinuities, we jointly invert them with the gravity data, which are sensitive to volumetric anomalies. The RF inversion task has been addressed by many authors in the literature with the application, among others, of different algorithms such as: genetic algorithm (e.g. Levin and Park, 1997; Shibutani et al., 1996), simulated annealing (e.g. Vinnik et al., 2004) and neighbourhood algorithm (e.g. Sambridge, 1999). The reader is referred to (Bodin et al., 2012) for further discussion on RF inversion approaches.

For this joint gravity and seismic data inversion, we implemented an iterative algorithm to explore the ensemble of all possible IGB models (i.e., the model space) and to evaluate their performance in terms of their fit to the observations. Even at a simplified parameterisation

of the model, the high dimension of variables (9 in our case) can require long and computationally expensive efforts (Sambridge and Mosegaard, 2002). To extract more information on models' behaviour in an efficient manner, our iterative algorithm explores in a guided pseudo-random fashion the model space. The algorithm is based on the principles of a Monte Carlo exploration, as at each iteration a new candidate model is proposed upon a random perturbation of the current model, and the exploration evolves as a series of small random steps. Strictly speaking, we implemented a Markov chain property as well, as the candidate model depends only on the current model, and its acceptance is based on the performance of its forward model with respect to the current's one only. If the new candidate model presents a better fit to the data (i.e., the performance), it is always accepted. Otherwise, its acceptance depends on a probability: the poorer the performance, the lower the chance to be accepted. At each iteration, the evaluation of the overall performance for a given candidate model consists of two parts – the seismic and gravity data modelling respectively – which are eventually combined together upon comparison with the seismic and gravity observations (Figure 4.4). It develops as follows. Given a candidate model, the associated velocity structure (defined by the candidate IGB model geometry, velocity and density contrasts) is used for both the seismic ray-tracing, and the computation and migration of the synthetic RFs. The same velocity structure and the associated ray-tracing are subsequently used for the migration of the observed RFs. We thus obtain a "synthetic" and an "observed" RF migration image respectively, which are then compared to define the candidate model's seismic performance. Similarly, the gravity model performance is evaluated by comparing the observed gravity anomaly to the synthetic gravity anomaly, computed for the same candidate model structure (Figure 4.4). The following paragraphs discuss more in detail the model parameterisation, the associated forward problem solution and joint model performance definition, and the technical implementation of the model space exploration.
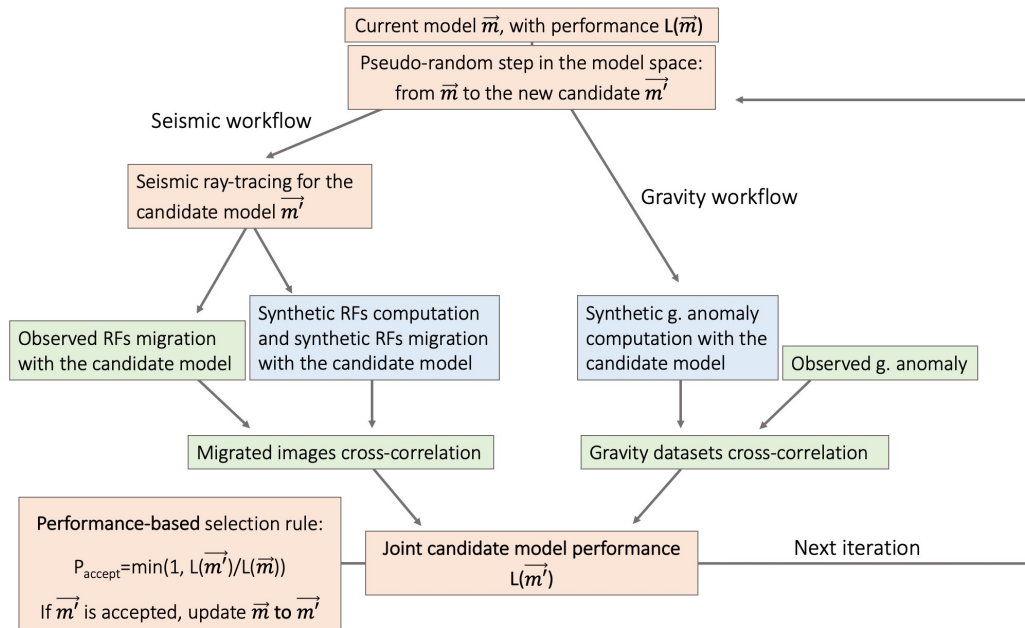
Figure 4.4 – The joint seismic-gravity inversion workflow implements a performance-driven pseudo-random walk in the model space and a performance-based selection rule for the new candidate models. Red boxes refer to the new candidate model generation and evaluation, followed by the forward modelling steps (blue boxes) and by the model performance evaluation (green boxes). At each iteration, a new candidate model is proposed. Successively, the associated seismic and gravity model performances are evaluated and combined into a joint model performance, which determines whether the newly proposed model is accepted or not (following the idea behind the Metropolis-Hastings selection rule). For coherency, the same model is used both for migrating the observed RFs and for generating and migrating the synthetic RFs at each step. The iterative procedure continues by suggesting new model space samples until the maximum number of iterations is reached.

4.4.1   Model parameterisation

We model the IGB's upper boundary as a single 2D discontinuity with a few segments, associated with sharp density ($\delta\rho$) and shear-wave seismic velocity (δv_S) contrasts (Figure 4.5)representing the IGB bulk physical properties with respect to the surrounding crust. While the former parameters are allowed to vary independently during the inversion, a homogeneous crustal background is assigned to the model and characterised by absolute values of $v_S = 3.5$ km/s and density = 2700 $kg \cdot m^{-3}$, which is also a consistent choice of velocity and density values, according to the v_S-density relationship from Brocher (2005) (as further discussed in paragraph 4). The choice of the background velocity fits well the upper crustal layer properties of 3.6 0.2 km/s deduced from a short period regional network (De Franco et al., 1997). The v_P/v_S ratio is fixed at 1.73 and 1.8 for the medium above and below the model interface, as indicated by the iasp91 model for the upper and lower crustal rocks. The number of parameters has been chosen based on the a priori knowledge of the IGB and of the associated seismic and gravity anomalies. Berckhemer (1968) and Kissling et al. (1984) provided seismic and

gravity evidence for an anomalously dense, eastward-dipping body. Further contributions showed sub-vertical and eastward-dipping units to the East of the Insubric Line (e.g. Petri et al., 2019; Zingg et al., 1990). In addition, the preliminary RF migration with a 1D velocity model (Figure 4.3) clearly points to a shallow interface in the western portion of the profile, and a deeper interface further to the East. In our investigation of the shape of the IGB-top structure, the model boundaries connect to the eastern and the western branches of the regional Moho interface (Spada et al., 2013), acting as far-field constraints on either side of our study's imaging area. We selected this Moho map as the reference crustal thickness only outside our data coverage and modelling domain, and kept it unvaried during the inversion procedure. The IGB model geometry is parameterised by 4 nodes, whose location can vary in space within given boundaries. This allows for a complete exploration in terms of width and depth of IGB head and neck, in analogy with the historical bird model anomaly as a vertical protuberance reaching shallow depths. The locations of the nodes, connected by straight segments, define the IGB model structure within the investigation domain (Figure 4.5). The western connection between node 1 and the Moho mimics the curved shape obtained in the 3D gravity model (Scarponi et al., 2020), as such a steep boundary is not resolvable with converted seismic waves.

We hence expect a shallow, not necessarily flat, discontinuity in the western portion of the profile and an eastward dipping structure – at an undetermined angle – towards the eastern portion of the profile. Therefore, we define four nodes to determine the IGB model geometry, and we prescribe that the depth of node 3 is the same as the depth of node 1. This still allows accounting for the East-West extent of the IGB, its variable eastern slope (due to the relative position of nodes 2 and 4), as well as a shallow interface with two segments, but saves one parameter to invert for.

Then, each IGB model is completely defined by 9 parameters:

$$\vec{m} = [\delta v_S, \delta \rho, x_1, x_2, x_3, x_4, z_1, z_2, z_4] \tag{4.1}$$

All these parameters can attain values within a fixed range, with the exception of z_2 and x_2, as node 2 is always prescribed to be located between (along x) and above (along z) node 1 and node 3, in order to investigate the shallowest features of the IGB head. Similarly, node 4 is prescribed to be farther east than node 3. Therefore, the allowed value ranges for x_2, z_2 and x_4 are dynamically adapted at each iteration, depending on the other parameter values. Figure 4.5 summarizes the possible range for each of the 9 inverted parameters, with minimum and maximum values based on a priori geometry and rock properties. The allowed range of $\delta \rho$ (Table 4.1) is broader than that of the best fit 3D gravity model ($400 \pm 100 \ kg \cdot m^{-3}$, obtained by sensitivity analysis in Scarponi et al., 2020), while the range of δv_S allows changes in a very broad range with respect to lower crust to mantle vS change in iasp91 (0.72 km/s). It also includes the full range of velocity variations from upper crust to upper mantle (up to 4.8 km/s) as suggested by the short-period regional network (De Franco et al., 1997).

Parameter	Min	Max
δv_S	0.1 km/s	1.3 km/s
$\delta \rho$	200 $kg \cdot m^{-3}$	600 $kg \cdot m^{-3}$
x_1	35 km	55 km
x_2	x_1	x_3
x_3	40 km	85 km
x_4	$\max(x_3, 75\text{km})$	105km
z_1	2km	15km
z_2	0.25km	z_1
z_4	20km	40km

Table 4.1 – Allowed-values range for each of the model space parameters. During the inversion, each parameter is free to vary within the given limits, with an exception for x2 and x4 which are constrained by the location of the neighbouring nodes.
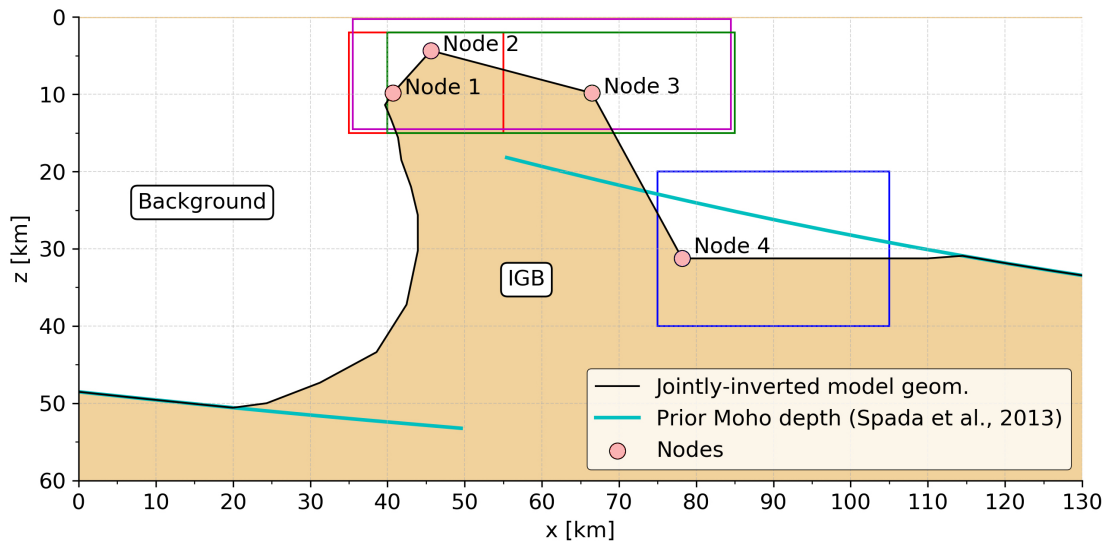
Figure 4.5 – Model parameterisation of the IGB shape used for the joint inversion of seismic and gravity data. We invert for the 2D IGB interface geometry (black line), whose configuration depends on the coordinates of four nodes (red, magenta, green and blue). Spatial positions of each node are investigated within a given perimeter (dashed boxes of respective color) during the inversion, together with the velocity and density contrast of the IGB relative to the surroundings. The far-field model geometry connects to the Moho map (Spada et al., 2013). In the East, the connection is by a horizontal line. In the West, the curved shape is taken from the earlier 3D gravity model of (Scarponi et al., 2020), as the vertical wall cannot be resolved by converted seismic waves.

4.4.2 Forward calculation and model performance

The forward modelling task produces the synthetics to be compared with the respective observations, for a given candidate model. It consists of two separate contributions – the seismic

and the gravity part – whose misfits are then combined (see Figure 4.6 for an example). The solution of each seismic forward problem produces two new RF migration images, which we may refer to as the "synthetic" and the "observed" migration images respectively. The synthetic RF migration image is produced via three main steps: seismic ray-tracing, synthetic RFs computation and synthetic RFs migration (Figure 4.4, Seismic workflow). Each of these steps always considers the candidate IGB model (or the current in the case of the first iteration): as a first step, we perform the ray-tracing across the candidate 2D velocity model structure for the same seismic catalogue – station pairs, identical to the observed dataset. Snell's law is respected at each model interface segment including local dip, meaning that it considers the relative angle between the propagating seismic trace and the dip (and depth) of the local interface segment (Figure 4.6b). The synthetic seismograms are computed via the Raysum software (Frederiksen and Bostock, 2000), whose code is wrapped in our inversion routine and receives as input the local IGB geometry along each ray-path. Finally, the synthetic RFs are migrated along the candidate velocity structure with the computed ray-tracing, therefore producing the "synthetic" migration image. In addition, the observed RFs are migrated as well along the same candidate model and ray-tracing (Figure 4.6d,e), producing the so-called "observed" migration image. This allows to compare in a consistent manner the observed and the synthetic RFs for each given candidate model. The migrations pictures are spatially smoothed by 2D Gaussian ellipsoidal filter with 1.5 km and 0.75 km horizontal and vertical half-width. Noise, taken as low-amplitude signals at <15 per cent of the image maximum amplitude, is removed from the observed migration picture. The final migration pictures have 0.5 km x 0.5 km pixel size.

We define the seismic model performance $L_S(\vec{(m)})$ as the zero-shift cross-correlation between the observed and synthetic RF migration images (Im_{obs} and Im_{syn}):

$$L_S(\vec{m}) = \frac{\sum_{i=1}^{N}(Im_{obs,i} \cdot Im_{syn,i})}{\sqrt{\sum_{i=1}^{N}(Im_{obs,i} \cdot Im_{obs,i}) \sum_{i=1}^{N}(Im_{syn,i} \cdot Im_{syn,i})}} \qquad (4.2)$$

where i is the pixel index and $L_S(\vec{(m)})$ is normalised, by definition, between -1 and 1. For the gravity forward problem, we implemented direct formulas for the computation of gravity anomaly for a given density distribution. The distribution is defined as an n-sided polygon in a two-dimensional plane (Hubbert, 1948; Won and Bevis, 1987), under the assumption that the geometry extends unchanged towards infinity along the direction perpendicular to the profile (i.e. the out-of-plane coordinate). Therefore, we numerically treat the IGB model shape as a 2D polygon associated with a $\Delta\rho$ density contrast with respect to the surrounding background. The synthetic gravity anomaly is then computed for each of the binned gravity points (Figure 4.4, Gravity workflow).

Similarly to the seismological part, we define the gravity misfit or model performance $L_G(\vec{(m)})$ as the zero-shift cross-correlation of the observed and synthetic gravity profiles (G_{obs} and

G_{syn}):

$$L_G(\vec{m}) = \frac{\sum_{i=1}^{N}(G_{obs,i} \cdot G_{syn,i})}{\sqrt{\sum_{i=1}^{N}(G_{obs,i} \cdot G_{obs,i})\sum_{i=1}^{N}(G_{syn,i} \cdot G_{syn,i})}} \tag{4.3}$$

where i is the single gravity point index and where $L_G(\vec{m})$ is normalised, by definition, between -1 and 1.

The problem of defining of a joint model performance (or joint misfit), combining the information from different geophysical data sets into the inversion process, has been addressed in the literature via different approaches. Various authors have introduced explicit scalar weighting parameters to accommodate for differences in the dataset's noise and information content (e.g. Julia et al., 2000; Syracuse et al., 2016). Other authors have implicitly incorporated the weighting between different datasets in a more recent Bayesian formulation of their inverse problem (e.g. Bodin et al., 2012).

In our case, the objective functions are not set up on physical properties with values on different orders of magnitudes, but instead they are cross-correlation based. Therefore, in our case, we define our final model performance function as the direct multiplication between the seismic model performance and the gravity model performance, following a maximum likelihood principle (Drahos, 2008):

$$L(\vec{m}) = L_S(\vec{m}) \cdot L_G(\vec{m}) \tag{4.4}$$

Thus, we obtain a performance measure for which we do not apply any user-defined weighting or scaling factor, and which, by definition, is normalised between -1 and 1.

4.4.3 Model space exploration

The model space exploration is carried out in a series of small random steps, with a new model being proposed at each of the iterations. Each of the model space coordinates m_j (with j=1, ...,9) has been assigned with a pair of minimum and maximum values, m_j^{min} and m_j^{max}, within which the model coordinates can range during the inversion procedure (Table 4.1). At each iteration, the exploration starts from the current model space location m^{cur} (i.e. the initial or the latest accepted model sample) and randomly suggests a new candidate model m^{cand}, related to m^{cur} by:

$$m_j^{cand} = m_j^{cur} + r_j \cdot s_j \cdot (m_j^{max} - m_j^{min}) \tag{4.5}$$

for j=1,...,9 where r_j is uniform random deviate and s_j a scaling parameter.

We defined an acceptance rule to guide the acceptance or not of the newly proposed model

m^{cand}. Given $L(m^{cand})$ the candidate model's performance and $L(m^{cur})$ the current model's performance, m^{cand} is accepted as model space sample if

$$r < \frac{L(m^{cand})}{L(m^{cur})} \tag{4.6}$$

where r is a random number between 0 and 1.

If m^{cand} is accepted, it is updated as new current model and it becomes the starting point for the subsequent iteration; otherwise, the exploration stays at m^{cur} a new candidate model is proposed.

The acceptance rule we adopted follows the idea behind the Metropolis-Hastings algorithm, which is developed for sampling a probability density function defined over a model space (Sambridge and Mosegaard, 2002). We apply that idea and its acceptance rule here, in non-probabilistic terms, to guide our random walk towards better fitting areas of the model space. In fact, when providing a better fit to the data, the newly proposed model m^{cand} is always accepted (i.e. when $L(m^{cand}) > m^{cur}$).The proposed model mcand can still be accepted, even when it provides a worse fit to the data compared to the current model m^{cur} (i.e. when $L(m^{cand}) < m^{cur}$), as there still is a non-zero probability for the random number r – constrained between 0 and 1 – to be minor than $L(m^{cand})/m^{cur}$: the lower the ratio, the lower the probability. The overall acceptance mainly depends on the shape of L(m) and on the distance between the current and the proposed model: $\Delta m = |m^{cand} - m^{cur}|$. In fact, the algorithm requires a fine-tuning of the jump length, which is the only necessary user-defined parameter. Too little steps could cause the model space exploration to be trapped in a local minimum, without escaping and thus leaving wide regions of the model space unexplored. On the other hand, too long steps could provide model proposals too far away from the best fitting areas, causing too many rejections and waste of computational resources. For this reason and based on three preliminary tests we performed on subsets of the data, we rescale the uniform random deviates to be within the [0.05,0.25] interval, which provided a balanced compromise between model space exploration and exploitation.

The inversion on the full dataset was eventually run for 50'000 iterations. As we do not formulate the inverse problem in probabilistic terms, this prevents us from interpreting the sampled models as the realisations of a probability density function. Nevertheless, we used the a priori knowledge on the IGB to assign reasonable boundaries to all inversion parameters (as discussed in paragraph 3.1) and we use a performance-driven pseudo-random walk to guide our exploration towards the best-fitting areas of the model space, to retrieve an ensemble of acceptable IGB models, which reproduce and explain the observed datasets.

4.5   Results

The inversion algorithm kept 41'363 models out of 50'000 iterations in one week of computation time on a standard computer (2.2GHz Quad-Core Intel Core i7), requiring 10s to 12s

per iteration. Throughout the model space exploration, 20'692 steps were directed towards a better performing model and were therefore retained. The remaining sampled models were accepted based on Equation 4.6 even if they were not improving the performance with respect to the previous iteration, with an acceptance ratio of ~70 per cent. Exploration has been favoured in spite of exploitation. By inspecting the distribution of all sampled models for all the model parameter pairs (appendix A.3), a satisfactory model space coverage has been achieved for all the pairs. Less samples cover the worse fitting areas, while a higher sampling density concentrates around the best performing models.

The seismic model performances range from 0 to 0.64 with a nearly symmetric bell-shaped distribution and a median value of 0.26 (negative performances have been discarded by choice). The gravity model performances vary across a narrower range of values, between 0.59 and 0.99, with a negative skew (more frequent higher values) and a median of 0.90 (appendix A.4). The better performance of the model with respect to gravity data is not surprising, as our a priori choices for the model geometry were driven by the recently constrained 3D gravity model. Therefore, in the final model performance, defined as the multiplication of seismic and gravity fits, the seismic performance acted as a more important guiding factor for the model space exploration. The gravity performance provided finer tuning across the best fitting areas, and also resolved some of the inherent trade-off in RF analysis. Furthermore, jointly inverting with seismic data allowed to constrain geometry features which were not resolvable with a gravity-only inversion, as demonstrated by preliminary tests (appendix A.5). The final model performances range between 0 and 0.60, with a median value of 0.22.

The results reproduce well the main features of the observed seismic and gravity anomalies. First, we describe the best performing model and then we consider the group of 150 best fitting models.

The best performing model fits the gravity anomalies both in terms of location and amplitude, with a slightly broader peak compared to the observations (Figure 4.6c). The vertical part of the IGB model is wider than what was suggested by the earlier, 3D gravity model (Scarponi et al., 2020). Node 2 locates the shallowest IGB portion in the vicinity of the western kink of the previous model (Figure 4.6a), as shallow as 4 km depth, and West of seismological station IA01A and of the IL at the surface. This location is a few kilometres too far to the West considering the local a priori geological knowledge. Concerning the migration images, the shallowest interface segment (node 2 to node 3) successfully reproduces the shallowest converted phases in the western portion of the profile, locating a sharp increase of shear-wave velocity right below the surface, between 3 and 7 km depth, and extending for ~20 km to the East from station IA01A to station IA05A (Figure 4.6d,e). Minor local features are recovered as well, such as the positive patch at ~75 km distance and at 12 km depth, and further reverberations at ~45 km distance and 15 km depth, below the shallowest conversion. The eastern portion of the image with prominent signals at ~35 km depth is recovered and consistent with the Moho depth further to the East (Figure 4.6a,d,e).

Using a single interface model prevents us from reproducing the eastern negative amplitudes at ~48 km depth ranging from 80 to 105 km distance, which cannot be regarded a converted-phase multiple reflection (PpSs) from an interface at 34 km depth. Such phase would be

expected at a higher delay time (~19 sec with the given model structure and therefore migrated at more than 100 km depth). This feature can represent a real decrease of shear-wave seismic velocity with depth, or PpSs multiples of local conversions seen in the upper crust (Figure 4.6d) which are not modelled in this distance range.
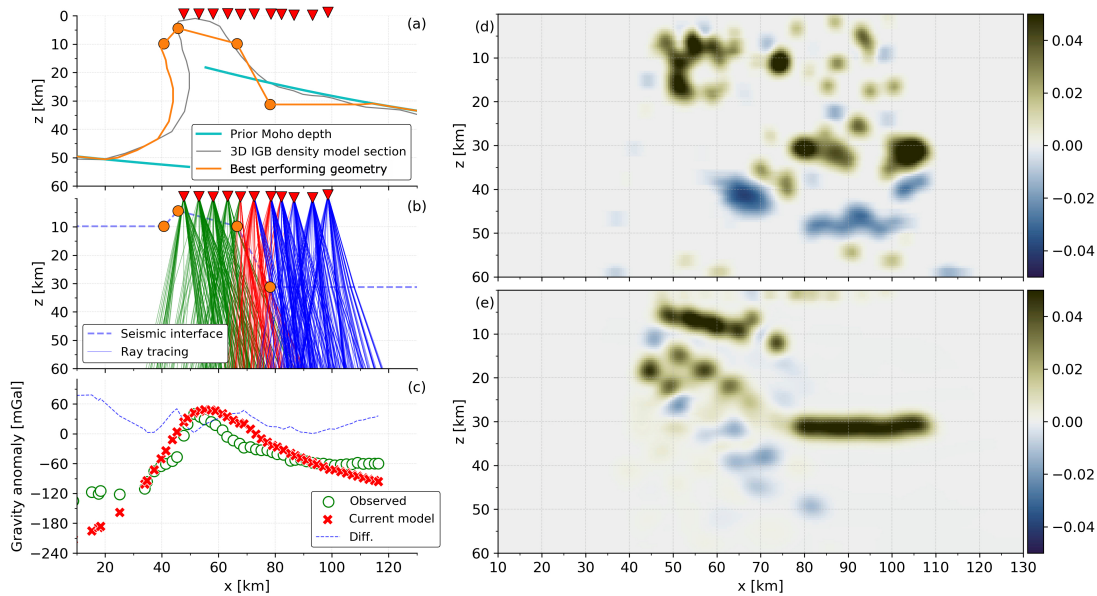

Figure 4.6 – Example of forward model calculation demonstrated on the best performing IGB model. (a) The current model geometry (orange line), defined by four nodes (orange circles) and assumptions as in Figure 4.5. (b) Seismic ray-tracing across the model interface (blue dashed line segments) for the current velocity model. Seismic rays are coloured according to the interface segment they cross along their path. The wave mode conversion respects Snell's law considering the local interface dip. (c) Comparison between observed and synthetic gravity anomalies for the current model, and their misfit. (d) Observed-RFs migration, including ray-tracing and migration with the velocity structure of the current model. (e) Synthetic-RFs migration, using RFs generated by the current velocity structure, and then treated the same way as the observed RFs. The comparison between Observed-RFs and Synthetic-RFs migrations is obtained via image cross-correlation (further details in the text).

A more representative image of the joint inversion results is provided by looking at the ensemble of the 150 best performing models (Figure 4.7). From this, the general characteristics of the retrieved well-fitting IGB model geometries can be outlined. It still is a shallow-reaching, crustal-scale important geophysical anomaly, similar to our earlier 3D gravity model (Scarponi et al., 2020), but without a prominent westward extending horizontal "beak" as in the historical model of Berckhemer (1968). A shallow interface is always present in the western part of the profile between 1 and 10 km depth, between IA01A and IA05A stations (~40 to 70 km distance). The position of the vertical structures is less constrained than the horizontal ones, as the steeply dipping structures cannot be imaged by the RFs at all. The shape of the western IGB vertical wall was inherited by the previous 3D gravity model (Scarponi et al., 2020) and its horizontal position was here varied together with node 1. The range of variation of either side

of the IGB neck spans ~15 km horizontally, while the horizontal segments span a narrower depth range (less than 10 km). In the western part, the neck is on average 30 ± 5 km wide, only a few models deviate up to ± 10 km width. The main IGB discontinuity is tightly constrained in the eastern, flat part of the profile at 35 km depth (Figure 4.7), which is consistent with the Moho structure there (Spada et al., 2013).
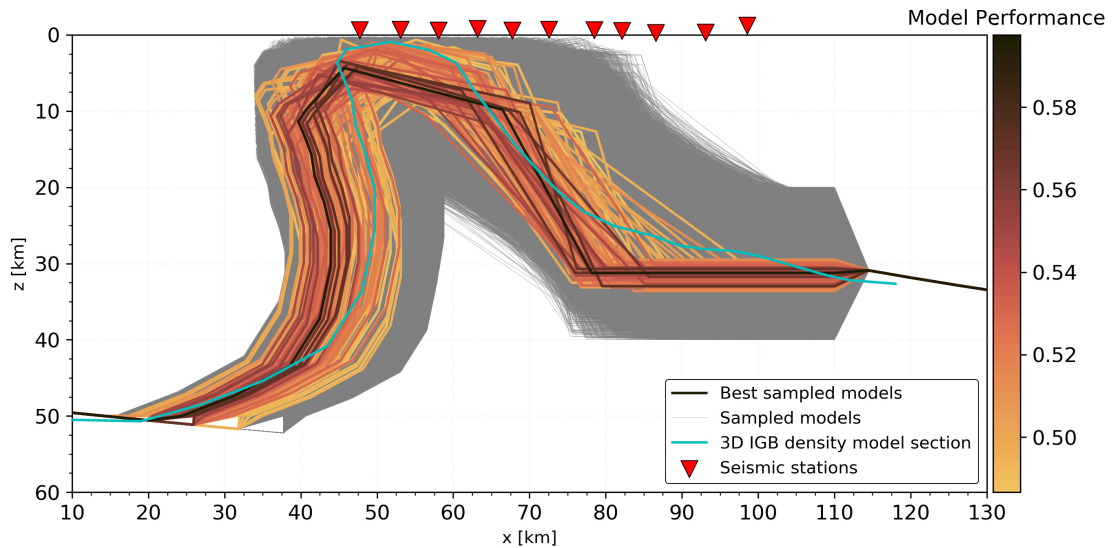

Figure 4.7 – Figure 7. Model geometries resulting from the joint inversion. The 150 best performing models are shown in coloured lines according to the model performance. All other sampled and kept models are shown in grey (in total 41'365 models). The cyan dashed line is the cross-section through the 3D IGB gravity model from previous study (Scarponi et al., 2020).

How well the IGB-top interface geometry is constrained by the joint inversion can be assessed through the distribution of the sampled model nodes position, which also shows the characteristics of the model space exploration (Figure 4.8). All four nodes have spanned the entire allowed perimeter, with a decreasing sampling density towards the worse-fitting external boundaries, and with node 2 being more restricted by definition of its position lying between and above nodes 1 and 3 (Figure 4.8). This proves the efficiency of the implemented algorithm in providing a satisfactory model space exploration, which is computationally much more affordable than a 9-dimensional full grid search at a comparable resolution. In general, node depths are better constrained better than their horizontal locations. The depth-variation range of ~10 km for node 1 to ~4-5 km for node 4. Node 1 solutions are preferentially at 10 km depth to West of the IL, which is in agreement with the IL being a vertical to sub-vertical dipping feature. Node 2 constrains the shallowest model position and features a bi-modal depth result, with a group of solutions between ~1-3 km at x=50-55 km. This finding is in agreement with the outcropping dense rocks at the surface. Another group of solutions concentrate at ~3-7 km depth to the West of the surface trace of the IL. Node 3 isn't tightly constrained; nevertheless, it extends the shallow IGB portion to the centre of the seismic profile, until the surface trace

of the Pogallo Fault Zone (PFZ), prior to high-angle deepening towards node 4 at 31~32 km depth (Figure 4.8).
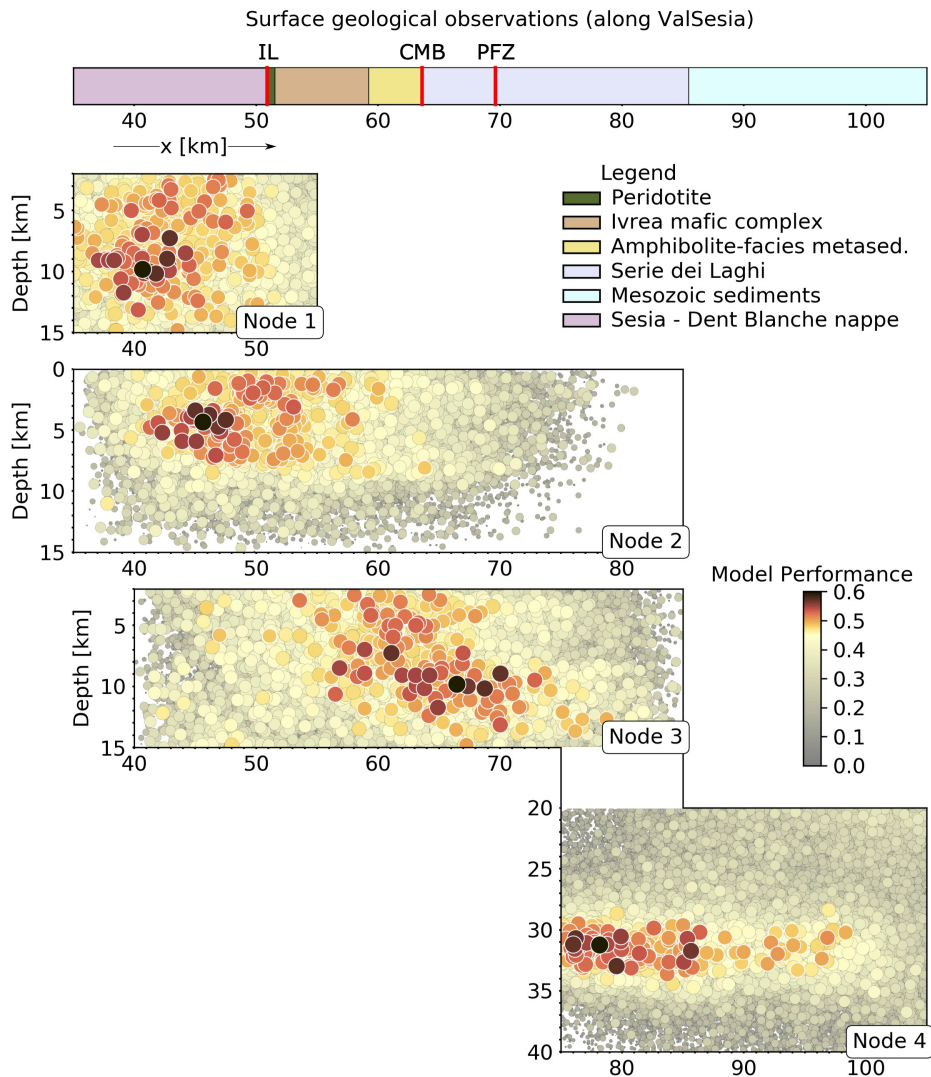

Figure 4.8 – Inversion results on the position of the four nodes, presented in four distance–depth panels. Each panel is showing the locations visited by each single node during the inversion, for each sampled model. All four panels share the same horizontal x-axis, but they are shifted along the vertical direction for better visual distinction. Panels of nodes 3 and 4 share the same depth axis, too. All sampled and kept models are shown (in total 41'363), with size and colour according to the model performance, plus all models with performance higher than 0.48 are indicated by white edges. Each panel is limited to the allowed range of parameter values. On top, the corresponding surface geological observations from earlier studies (along the same x-axis), identifying rock types along the profile (legend on the top right, same as in Figure 4.2). The relevant faults for this study are indicated (as in Figure 4.2) as "IL" for Insubric Line, "CMB" for Cossato-Mergozzo-Brissago Line and "PFZ" for Pogallo Fault Zone.

Concerning the physical property contrasts of the IGB compared to the shallower layer (Fig-

ure 4.9), the well-performing models point to a relatively broad range of shear-wave seismic velocity increases. This is mainly constrained by the amplitude of the Ps signals, which is not their most reliable feature due to attenuation. A certain number of better-performing models is associated with a velocity contrast of the order of 0.5 to 1.2 km/s. The best performing density contrasts are in the 200 to 400 $kg \cdot m^{-3}$ range, with some models at 500 $kg \cdot m^{-3}$ associated to the higher vS contrasts. This is in good agreement with the earlier 3D gravity model which suggested that 500 $kg \cdot m^{-3}$ represents a reasonable higher limit for the IGB density contrast (e.g., Scarponi et al., 2020). We note that models with very high density- and low velocity-contrasts perform poorly (Figure 4.9).

We note that the gravimetric method is able to resolve density contrasts, and not absolute densities. Therefore, the set of inversion results on Figure 4.9 can be shifted to the right, to higher density values, by simply assuming that the surrounding crustal density was not 2700 $kg \cdot m^{-3}$ but higher. A geologically reasonable shift would be around 100 $kg \cdot m^{-3}$: a density of 2800 $kg \cdot m^{-3}$ is reasonable for mid-crustal rocks; hence, the well-fitting models from the joint inversion would fall closer to the v_S–ρ relationship trend taken from Brocher (2005). We note that the trend line of Brocher (2005) represents empirical fits, and that actual rock property data dispersions of 0.2 km/s in v_S or of 200 $kg \cdot m^{-3}$ are reasonable.
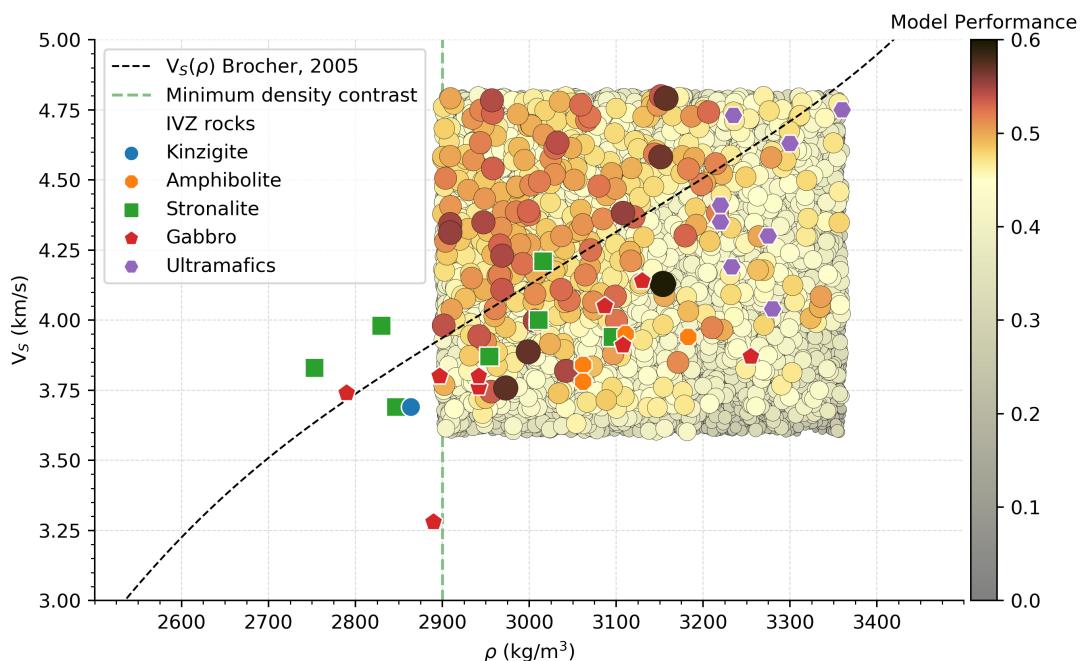

Figure 4.9 – Inversion results on the density and shear-wave velocity contrasts associated with the 2D model interface, shown as gray-contoured circles of size and colour according to to the model performance. The background density and the background shear-wave velocity absolute values are common for all models (2700 $kg \cdot m^{-3}$ and 3.5 km/s respectively). For comparison, the regression fit for the vs(ρ) relationship from rocks discussed in Brocher (2005) (black dashed line) is shown together with a relevant set of rock physical properties across the IVZ from the SAPHYR catalog (Zappone and Kissling, 2021).

4.6 Discussion

The inversion results can be interpreted in light of the existing multidisciplinary investigations on the IVZ formation history and the surrounding crustal structures. By inspecting the best performing IGB models (Figure 4.7), two main groups of models can be identified according to the shallow geometry characteristics of the retrieved IGB models (Figure 4.7, Figure 4.8, node 2). The first group of models suggests a gently eastward-dipping interface in the shallow portion, locating the IGB-top head from ~3-7 km depth (node 2) to ~8-12 km depth (node 3) with a minimum horizontal extent of ~20 km. The second group of models features node 2 at clearly shallower depths than nodes 1 and 3, reaching as shallow as 1-3 km depth between seismological stations IA01A and IA03A. While both groups are in agreement with a western boundary associated with a steeply westward dipping IL, the very shallow anomaly of the latter group agrees with the well-known variety of lower to middle crustal rock outcrops observed across the IVZ. Moreover, when compared with the rock properties of in situ IVZ samples (Zappone and Kissling, 2021) in vS–ρ space, the inversion results show good agreement with several gabbro samples, and also with ultramafic rock and amphibolite samples if the aforementioned density-shift is considered (Figure 4.9). These align with indications drawn from studies by Pistone et al. (2020) and Scarponi et al. (2020) on possible rock types. However, we make no further selection of rock types, to avoid potential over-interpretation here, as reality is surely more complex than a single-discontinuity 2D model. Nevertheless, considering the model assumptions, the match with rock properties is satisfactory.

An interesting feature of sampled IGB model structures is the steep eastward-dipping segment at the centre of our profile between nodes 3 and 4 (~70-75 km distance, Figure 4.7), representing the eastern flank of the IGB. The steepness of this segment precludes any direct imaging by the RFs. The segment, however, joins the two surrounding and imaged segments (between nodes 2 and 3 and east of node 4) and it compares well with the location at the surface of the Pogallo Fault Zone (PFZ, Figure 4.8). The PFZ is a prominent Jurassic fault zone associated with pre-orogenic crustal thinning episodes, related to the opening of the Alpine Tethys without being subsequently reactivated during the orogenic compression, but only tilted to its present-day vertical position (Handy et al., 1999; Petri et al., 2019).

The PFZ crosses our seismic profile at the surface at the Lago d'Orta, between stations IA05A and IA06A. Several evidences suggest that the PFZ may have offset the Moho during the Jurassic (Handy, 1987) and that the shape of the IGB was determined by a combination of Jurassic crustal thinning and subsequent Alpine orogeny (Schmid et al., 1987). The importance of pre-orogenic inheritance with respect to syn-orogenic processes is however clearer in the light of our results. Along our profile, the eastern flank of the IGB coincides much more closely with the surface exposure of the PFZ than what was pointed at by previous models (Berckhemer, 1968): the PFZ is likely responsible for shaping the Moho since the Jurassic, implying that the IGB was strongly pre-set by the pre-orogenic rift-related deformations, before being integrated in the Alpine orogeny.

In light of the planned scientific drilling in Val Sesia (Pistone et al., 2017), we further investigated one particular property of the shallowest portion of the IGB interface, namely the

sharpness of the velocity discontinuity, by applying frequency-dependent RF analysis. In fact, the frequency content of the observed RFs can put constraints on the resolved thickness of the seismic velocity gradient associated with the converted-wave generating interface itself (James et al., 2003). The narrower the peaks with increasing RF analysis frequency, the sharper the interface at which the conversion was produced. Conversely, if there is a vertical gradient, the highest frequency RFs will remain broad and lose amplitude. We demonstrate this effect by synthetics, which we then compared with the observed RFs. We focused our analysis on station IA02A and stacked a high-quality selection of RFs, for a certain number of high-pass filtering frequencies: 1Hz, 2Hz, 3Hz, 4Hz and 6Hz respectively (Figure 4.10a). We used RFs in the ZRT coordinate system and only for eastwards [45-135°] back-azimuths to maximise the Ps conversion amplitude on the inferred eastward dipping interface. The RF stacks show two shallow conversion peaks at ~3 and 6 km depth (Figure 4.10a). Considering the respective piercing points, the two peaks correspond to early arrivals from ENE to late arrivals from ESE. This points to local structural variations at shallow depth beneath the gabbro and norite rocks exposed on the surface (Figure 4.10b). Comparing our results to the synthetics shown in Figure 4.10(c,d,e) indicates that the velocity gradient thickness is more than 0.4 km, and closer to but less than 0.8 km. This is slightly more than the Moho transition zone of 0.5 km proposed for the Kaapvaal craton by James et al., 2003, based on a similar seismic analysis. Our finding is well-resolved as the wavelength of 6Hz waves at v_S of 3.5 km/s is below 600m, so this approach would have been able to resolve sharper gradients.

Future contributions could address the IGB structure by inverting for more complicated geometries, including more than one seismic interface. P-to-SH converted phases could be addressed as well, as they do present seismic energy due to the presence of dipping angles and possibly anisotropy, which was not addressed in this contribution as there were strong a priori indications for dip. Much finer, high-resolution images of the western part of our area will be revealed with the recently acquired active seismic data with Vibroseis sources and several targets at depth along two long profiles crossing between stations 1 and 2, and carried out as a cooperative project between GFZ Potsdam, Montanuniversität Leoben and the University of Lausanne. We plan to complement these with higher resolution gravimetric and magnetic measurements around the Balmuccia peridotite, to approach the scale of scientific drilling. Subsequent, joint petrological and geophysical investigations will further constrain the lithologies composing the IGB.
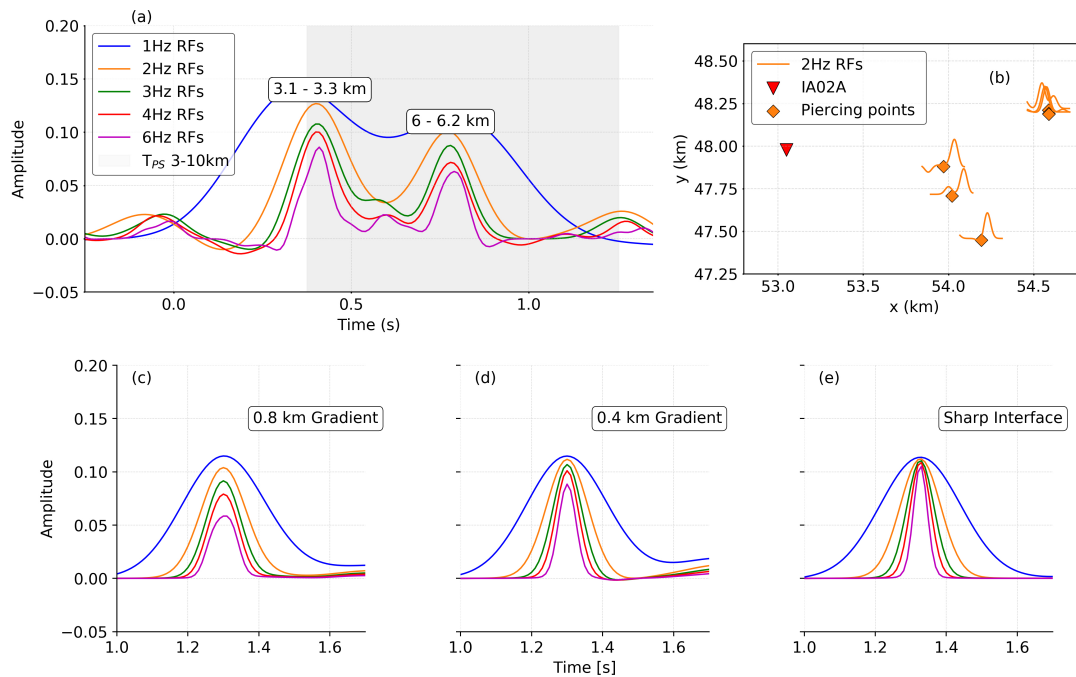
Figure 4.10 – Investigating the sharpness of the seismic interface by frequency-dependent analysis of the highest quality RFs near station IA02A. (a) Observed RFs stacked at different frequency ranges, from 0.1Hz to five different maximum frequencies as specified in the legend. The decreasing signal width, with increasing frequency, points towards a discontinuity sharper than the resolution of the highest frequency waves. The gray band in the background indicates the expected time delay for a P-to-S converted phase from a discontinuity located between 3 and 10 km depth, and with vs = 3.5 km/s above it. The estimated depth of the conversion for the two observed peaks is indicated. For this analysis, a stricter quality control has been applied and only the RFs qualifying at all frequency ranges have been considered. (b) Piercing point map (orange squares) for the traces that have been considered in panel (a), for the frequency range 0.1Hz to 2Hz. Next to each piercing point, the time interval 0 to 1s of the associated RFs is plotted, to highlight the spatial variability of the stacked RFs signals. (c-e) Synthetic RFs for the same frequencies as in (a) demonstrating the effect of velocity gradient sharpness on peak widths and amplitudes.

4.7 Conclusions

We implemented and ran a joint inversion algorithm using seismic receiver functions and gravity data to constrain the shape and the physical properties of the Ivrea Geophysical Body (IGB), along a 2D West-East cross-section along the Val Sesia profile and across the Ivrea-Verbano Zone (IVZ). The algorithm executes a performance-driven random walk in the model space, to preferentially explore the better fitting areas of the model space.

Processing the new seismological and recently collected gravity data led to new constraints on the IGB structure. A shallow and relatively sharp interface is resolved over at least 20 km

horizontal distance in the western part of the seismic profile (between ~8.11E and 8.43E). In particular, we identify two main groups of model geometries for the shallowest portion of the IGB: a flat and gently eastward-dipping interface between 3 and 7 km depth, and a structure with a local peak reaching as shallow as 1-3 km depth, beneath the three westernmost stations (~8.11E to 8.25E). While both groups of models agree with a western boundary associated with the steeply westward-dipping Insubric Line, the latter is more consistent with the well-known lower crustal rock complex outcropping at the western edge of the IVZ. Further agreement with the observed geological structures at the surface is found by comparing the IGB model structure with the location of the Pogallo Fault Zone (PFZ). The eastern flank of the protruding IGB coincides with the surface exposure of the Jurassic PFZ, highlighting the role of pre-orogenic processes in shaping the IGB.

The retrieved IGB velocity and density contrasts relative to the surroundings are in general good agreement with the physical properties of the rock samples collected in the area and analysed in earlier studies. The results span a rather broad range of acceptable shear-wave velocity contrasts (0.5 to 1.2 km/s), providing slightly higher velocities than those from field samples and/or trends in the literature (Brocher, 2005). In terms of density, a reasonably narrow range of better-fitting density contrasts of 200-400 $kg \cdot m^{-3}$ is found, in agreement or slightly below the recent 3D IGB density model.

We further analysed the amplitude and frequency content of a stack of selected high-quality receiver functions, to constrain the sharpness of the vertical velocity-gradient associated with the shallow IGB discontinuity. We then compared the observed stack with synthetics, for a range of different pre-deconvolution maximum filtering frequencies, and using various vertical velocity-gradient thicknesses. We found thicknesses of 0.8 km and 0.4 km as reasonable higher and lower limits for the shallow velocity-gradient mimicking the top of the IGB discontinuity. Already acquired but still in-the-processing active seismic campaign data will shed more light on the very shallow structure at high resolution along the same profile, and prepare the ground for deep scientific drilling to deepen our knowledge of the IGB.

4.8 Acknowledgements, funding, authors contribution and data availability

5 The Gotthard Base Tunnel profile: a gravimetric assessment

5.1 Introduction

The Gotthard Base Tunnel (GBT) is a 57 km long railway tunnel, currently the longest on Earth, constructed in the Central Alps in Switzerland and extending mainly North-South (at ~ 8.77°E and from ~ 47.37°N to ~ 46.84°N). Locally it gets as much as 2500 m below the surface in the areas of higher topography, which ranges between 300 and 3000 m above sea level. The tunnel itself remains mainly at 500 m above sea level and crosses a number of important tectonic units, mainly belonging to the European continental crust (e.g., Schmid et al., 2017) and mainly deformed after the Alpine collision (35-30 Ma, Schmid et al., 1996): the Aar Massif, the Tavetsch Massif, the Urseren-Garvena Zone, the Gotthard Massif and the Penninic Gneiss Zone. A rich amount of geotechnical data was collected during the tunnel construction and the subsequent operation phases (e.g., Löw et al., 2015). The surface and tunnel surveys related to the construction provide an unprecedented sub-km-scale and "inside" view of the geological structure of the very shallow crust along the GBT profile (Figure 5.1). The tunnel crosses several geological units, presenting vertical to sub-vertical features, with their strikes mainly along the WSW-ENE direction. During the tunnel construction, relative gravity data was measured by swisstopo (Swiss Federal Office of Topography) inside the tunnel with an average spacing of ~ 800 m. While the GBT geological profile presents a variety of units interpolated between geological field mapping and tunnel observations, it has never been tested with the available gravity observations.

In the literature of gravimetry, several methods have been suggested to estimate the optimal reduction density for a topographic profile (e.g., Nettleton, 1939, Parasnis, 1952, Fukao et al., 1981). Nettleton's method (Nettleton, 1939;Nettleton, 1976) is maybe one of the most known approaches. It is based on the assumption that the Bouguer gravity anomaly profile, computed for a set of densely spaced gravity measurements along a certain topographic profile, should not be correlated at all with the topography when the correct reduction density is applied. Hence, this method allows to set up a trial-and-error search for the best reduction density value,

obtained when the correlation between topography and Bouguer gravity anomaly approaches 0. However, this method works under the limiting assumption of a constant, homogeneous reduction density, which is less likely to represent reality for long tunnels. Therefore, the GBT geological profile, together with the available gravity observations in the tunnel, constitutes an ideal natural target to test the resolving capabilities of gravity data analysis, to test and/or constrain the geological units' density and/or geometry along the GBT profile.

To this end, as explained in the following paragraphs, the GBT geological profile has been digitised to be associated with a 2D density distribution and subsequent forward modelling. In addition, I have collected new gravity data at the surface, along the tunnel track, to optimize measurement coverage and to mimic the gravity data point distribution in the tunnel. In the following paragraphs, I present the new gravity data I collected, together with the associated processing practices to simplify 3D reality to a 2D gravity model, including a novel, density-dependent gravity terrain correction to be applied to the observed gravity data, prior to the comparison with the synthetics from the 2D geological profile. A consideration of applicable density for various lithologies is also presented.

As of today, first results are available, and will be further polished before a manuscript is prepared for peer-review.

5.2   Geological setting

In this section I present the Gotthard Base Tunnel geological profile (Guntli et al., 2016) and I explain how it has been digitised and adapted for the subsequent analysis. The digitalization process served for extracting the coordinates of the contours of each geological model unit, and to associate them with a given density for the forward gravity modelling. Prior to the modelling phase, both the reference geological model, and the acquired and the compiled gravity data have been projected onto a straight profile, connecting the southern and northern tunnel portals.

5.2.1   Tunnel geological profile

The geological profile along the Gotthard Base Tunnel track has been published in form of supplementary material to a complete geological, geotechnical and hydrogeological final report on the tunnel (Guntli et al., 2016). The geological profile presents lithological information for the shallow crust along the tunnel track, extending from the surface to 300 m above sea level. It covers the whole length of the tunnel, presenting different rock units of various lithological and geological signature, including an indication for more recent Quaternary sediments (Figure 5.1). While the southernmost segment of the Gotthard Base Tunnel geological profile is mainly dominated by Gneiss formations, the central and northern segments present several thin km-scale units characterized by a vertical to sub-vertical structure. These units are intersected by the tunnel profile almost perpendicularly with respect to their strike (Figure 5.2).
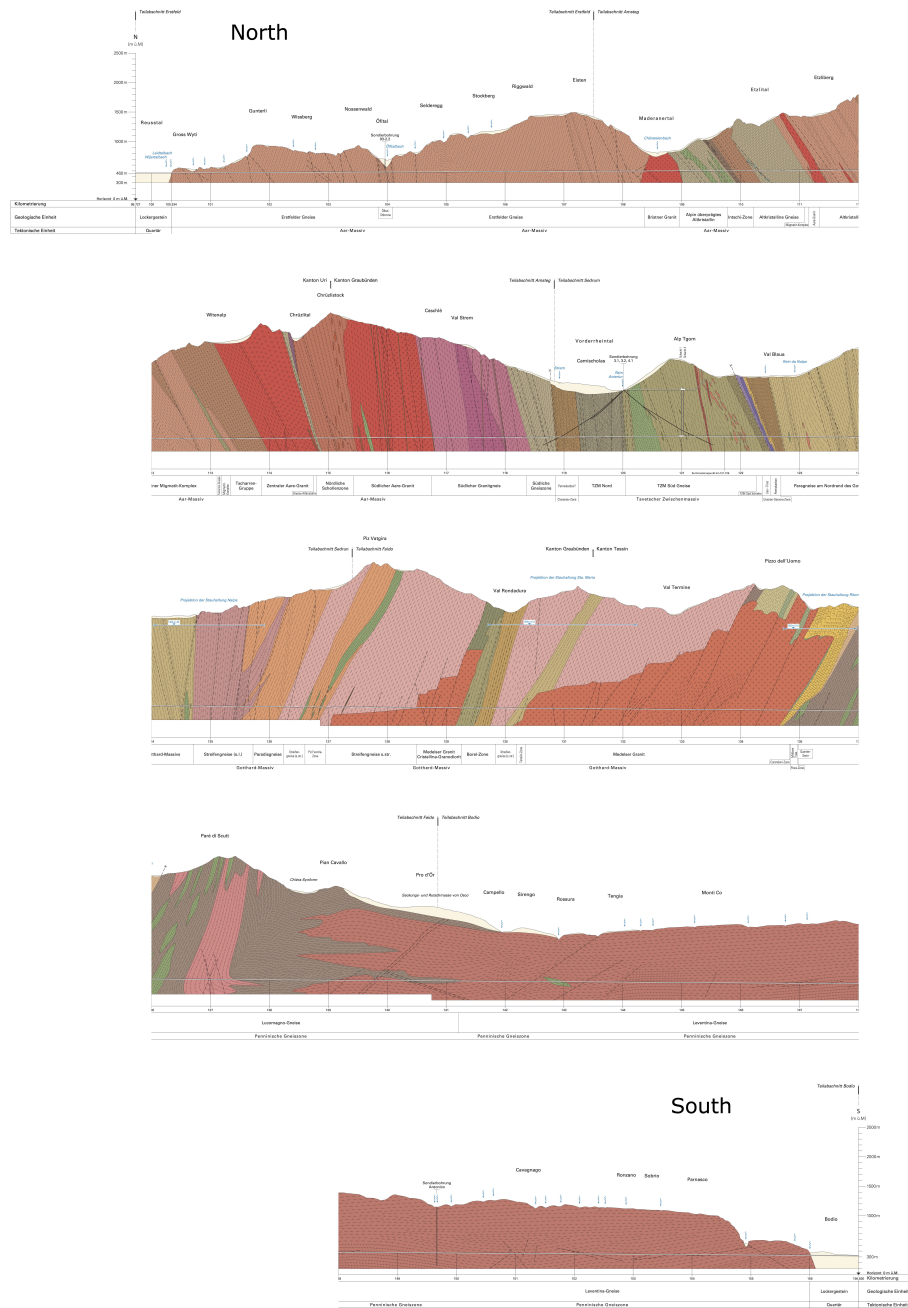
Figure 5.1 – Gotthard Base Tunnel geological profile. For sake of graphical representation, the profile has been split in five sections from North to South. The profile shown in this picture is slightly different from the digitised one, which was updated and later released (Guntli et al., 2016). The associated legend, describing all the units, is reported in Guntli et al. (2016) in paper format only.

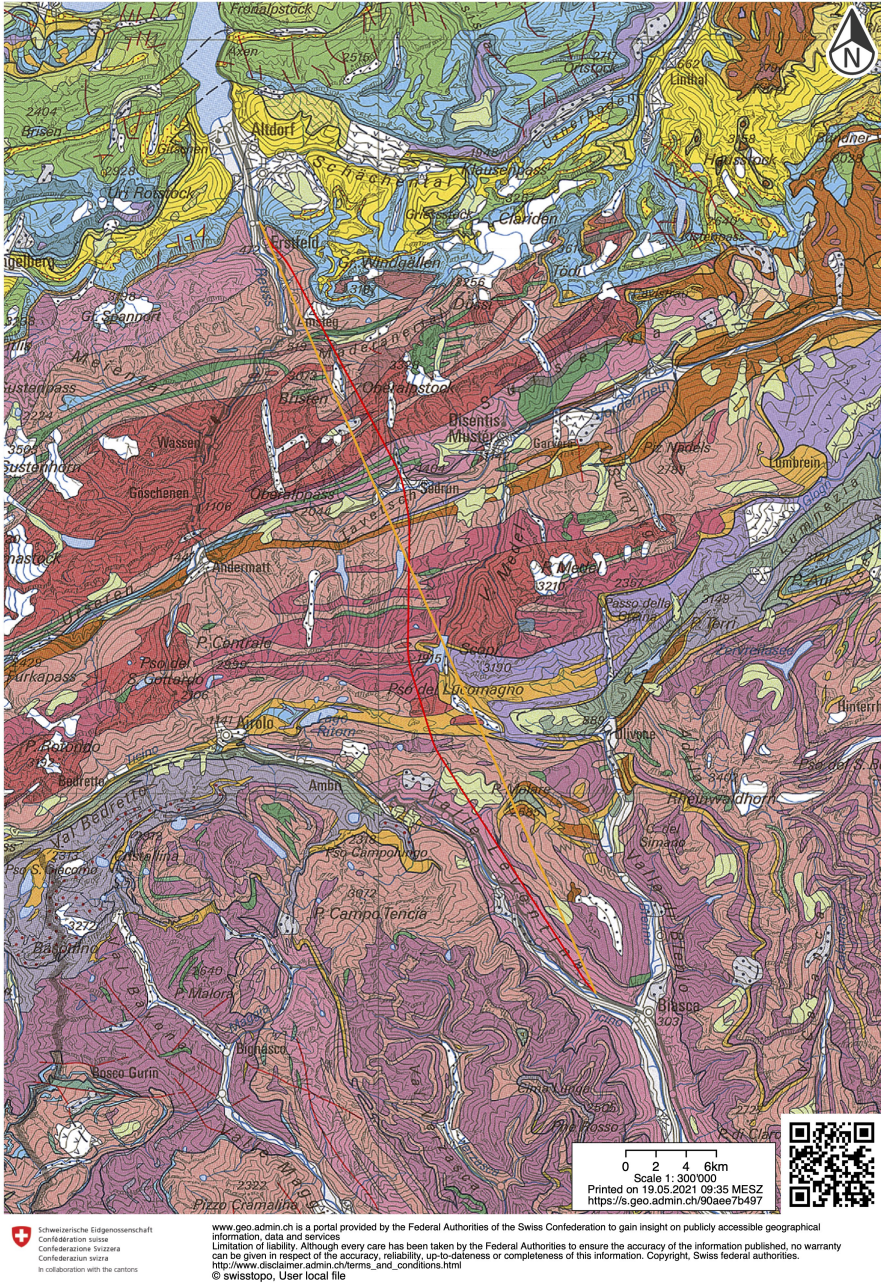Figure 5.2 – Geological map of the area surrounding the Gotthard Base Tunnel. The red line in figure indicates the Gotthard Base Tunnel track while the orange line indicates the reference straight model line, onto which geological profile and gravity measurements are projected. In color, the mapped geological units at the surface. The geological map is freely accessible online at https://map.geo.admin.ch/.

The geological profile has been kindly provided by swisstopo in .pdf format, from which I removed all the elements except for the coloured geological units and the reference frame. The reference frame has been set to 0 km horizontal distance at the norther tunnel entrance (which is at 99.727 km in the original document) and to 0 km vertical elevation at the sea-level line, as in the initial document. Some of the smallest units have been neglected or merged together. This is the case for small units which are expected to produce a negligible gravity signal and therefore not detectable (e.g. a unit less than 120 m wide and 1 km deep with a 200 $kg \cdot m^{-3}$ density contrast would produce a 1.11 mGal gravity signal). These smaller units were most likely interpreted from local observations, either at the surface or inside the tunnel only. Small lenses of little spatial extent were removed as well. With the use of the legend of the geological profile (Guntli et al., 2016), the remaining formations were labelled and assigned with a lithology. In this way, the simplified along-tunnel 2D geological profile is composed of 69 bedrock geometries, filling the area between surface and 300 m above sea-level along the Gotthard Base Tunnel.

Steps of this workflow included manual editing in AdobeIllustrator, exporting a .dxf file to be read by QGIS, exporting to .csv format to be read by Matlab, which then prepared files compatible with the subsequent 2D gravity forward modelling.

5.2.2 Density data

Every geological unit of the adapted Gotthard Base Tunnel profile has been assigned with density values, depending on the tested density models. The density is assumed to be constant and homogeneous within each unit. The main source of rock density information is from rock sample laboratory analyses as provided by the SAPHYR catalog (Zappone and Kissling, 2021). While the latter has been published just recently on the Swiss Journal of Geosciences, the first rock density information was released in 2020 on map.geo.admin.ch from the same source, providing mean density values by lithology, averaged across Switzerland's broader region.

In the scope of this project, density data for 121 rock samples in the vicinity of the Gotthard Base Tunnel was selected, and subsequently used to assign density values to each unit based on their location along the profile. SAPHYR provides ρ_{grain} and ρ_{wet} density data: the former was used for samples collected at the surface and the latter for samples collected in the tunnel. Based on the above data, six different density models have been compiled to be tested with gravity data modelling (see descriptions here below and numbers in Table 5.1).

- **Model.1** This model is based on the best guess of density values from SAPHYR point-wise data, by associating to each unit the spatially nearby samples' density values, considering the same lithology from the database and on the profile. The Quaternary units were associated with 2200 $kg \cdot m^{-3}$. The bodies for which there were no available samples were associated with average values for the same lithology from the 121 SAPHYR samples, including sub-specifications for gneiss based on number of samples and mineralogical composition: 2665 for granite, 2718 for schist, 2974 for amphibolite, 2710 for gneiss, 2664

for two-mica-gneiss, 2755 for two-mica-gneiss, 2775 for garnet-two-mica-gneiss-schist (all in $kg \cdot m^{-3}$);

- **Model.2** This model is based on the same lithology-wise averages for all the units, with sub-groups for gneiss, and further values such as: 2650 $kg \cdot m^{-3}$ for pyroclastic rocks, 2751 $kg \cdot m^{-3}$ for phyllite and 2740 $kg \cdot m^{-3}$ for paragneiss;

- **Model.3** This model is composed of single values for each lithology, without any sub-group for gneiss but using averages from the selected SAPHYR database: 7 different values are used to assign the entire model;

- **Model.4** This model is similar to model 3, but uses the average values of the entire SAPHYR database for the broader region of Switzerland;

- **Model.5, Model.6** These models are set to lower and upper reasonable density value bounds for each lithology, based on the lowest and highest SAPHYR data-points and the 5th and 95th percentile of regional density distributions per lithology.

Finally and for all the tested density models, the far field extension has been applied with a constant density value of $2670 kg \cdot m^{-3}$. Furthermore, the area between sea-level and the 300 m elevation line (which is not covered by the Gotthard Base Tunnel geological model) has been filled with a regular body of $2670 kg \cdot m^{-3}$ density as well. This last addition allows for consistency between the 2D forward modelling and the corrected gravity observations (described in paragraph 5.5.3), requiring no shift at all when comparing the synthetics with the data (paragraph 5.6).

Lithology	Model.3	Model.4	Model.5	Model.6
Amphibolite	2861	3006	2648	3180
Dolomite	2885	2540	2081	2885
Gneiss	2710	2687	2587	2790
Granite	2665	2606	2392	2722
Quaternary	2200	1776	1700	2400
Schist	2718	2715	2622	2808
Vulcanite	2650	2641	2531	2716

Table 5.1 – Densities in $kg \cdot m^{-3}$ of the main lithologies, for models from 3 to 6 as described in the text.

5.2.3 Digital elevation model

I used the *swissALTI3D* digital elevation model by swisstopo (https://www.swisstopo.admin. ch/en/geodata/height/alti3d.html) to sample the topography in the vicinity of the surface

gravity measurements and along the tunnel line. *swissALTI3D* provides elevation information on a regular grid of 10 m horizontal resolution, compiled in km^2 tiles. The tiles were merged with the open-source software QGIS, which was also used to sample the digital elevation model at the points of the processing mesh (described in paragraph 5.5.2). Similarly, the SRTM digital elevation model (Farr et al., 2007) was used to sample the topography farther away from the tunnel area and outside Switzerland's borders, as it provides topographic information at 3 arc-seconds (ca. 90 m) resolution.

5.3   Gravity data acquisition and pre-processing

I compiled a new gravity database for this study, by merging existing gravity data in the tunnel with the new gravity data I acquired in the field. The prior gravity dataset consists of measurements taken inside the Gotthard Base Tunnel at the time of its construction, while the new gravity data has been measured at the surface, as close as reasonably possible to the tunnel track (Figure 5.3). The aim at the design of the surface field campaigns was to mimic as much as possible the spatial distribution of the prior tunnel points, which is approximately 1 point every 800 meters.

This data distribution allows a consistent comparison between tunnel and surface data and also allows to model the density of the relatively smaller units mapped along the Gotthard Base Tunnel geological profile: the median unit horizontal thickness along the geological profile is 273 m with a mean of 800 m. In the following, the data collection procedure and the pre-processing practices (from raw data to absolute gravity values) are presented.

5.3.1   Compiled tunnel gravity data

The available gravity data was measured inside the Gotthard Base Tunnel track by the Swiss Federal Office of Topography (swisstopo: https://www.swisstopo.admin.ch/), at the time of the tunnel construction, and it was subsequently compiled for the work presented in this thesis. The tunnel gravity data set was kindly shared with us by U. Marti, providing absolute gravity data points together with coordinate and quality information. One point inside the tunnel was discarded as outlier with respect to the whole data set, and other 5 points were not taken into consideration as they were measured outside the tunnel portals. The final compiled dataset consists of 77 gravity data points, distributed along the tunnel with a mean spacing of 745 m and a median spacing of 933 m. Following the tunnel, the gravity data points range from ~ 315 to 550 m in elevation above sea level.

It should be noted that the final gravity data modelling is done in 2D along a linear profile connecting the two tunnel portals, and to which all the data points are projected: the final, projected tunnel data along the model line has 729 m mean spacing and 886 m median spacing, with a mean projection distance of 1389 m from its original location to the model line.

5.3.2 Field surveys and new gravity data

I carried out two gravity measurement campaigns, which required on the field ca. 10 days in June 2020 and 1 additional week in September 2020. The local topography ranges from ∼ 300 m above sea level in the valley bottoms to ∼ 3000 m at the local summits: substantial physical efforts were required to measure gravity data points at the surface while remaining as close as possible to the tunnel line, and avoiding Quaternary units as much as possible. Each gravity campaign required at least two people in the field, to share the weight of the equipment and combine driving and planning. We reached some of the points by road vehicle and the remaining on foot, with ca. 1000 m vertical elevation change on several days. On two occasions, we benefitted from a one-way helicopter lift to reach the most remote areas and realize physically feasible days. At the end of the two campaigns, we collected 80 new relative gravity points, well distributed both in terms of distance from the tunnel and in terms of spacing compared to the reference tunnel data points (Figure 5.3). The mean distance from the surface gravity measurements to the tunnel track is 258 m, while the mean spacing of the surface gravity data points after projection along the 2D model line is 694 m.
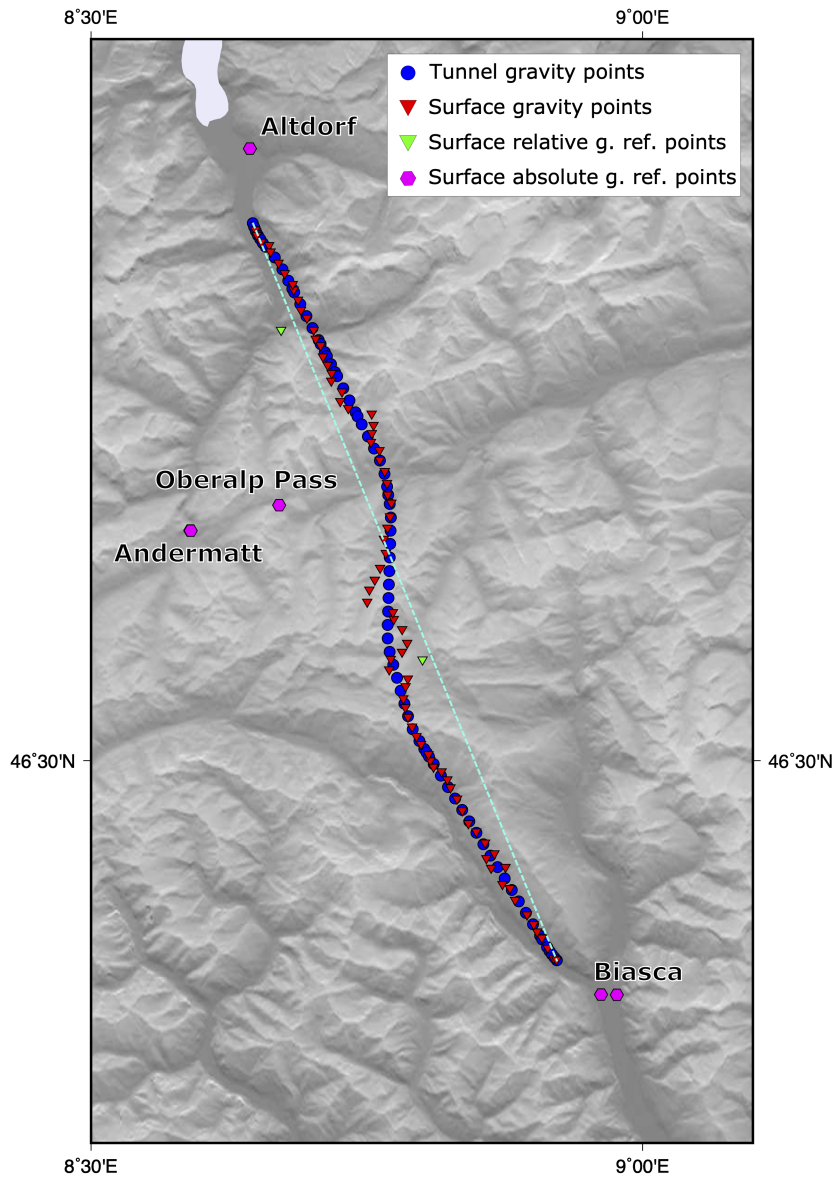
Figure 5.3 – A topographic view of the study area showing the location of the newly acquired 80 gravity points (red triangles) and the compiled tunnel gravity data points (77 points; blue circles). The green triangles represent our own established relative reference points, which we tied to earlier existing absolute gravity reference points (magenta hexagons) and used to open and close daily measurement loops during the campaigns. The cyan dashed line represents the 2D model reference line, onto which both the geological model units and the gravity measurements are projected for comparison between synthetics and observations using 2D forward modelling.

All the measurements were organised into daily loops, with each day or half-day of the field campaign always starting and finishing at a location with known absolute gravity value, and mostly the exact same location. This practice allows to estimate the inherent instrumental drift of the Scintrex CG-5 relative gravimeter, which measures the relative gravity difference between the current measuring point and the previous one. Once the instrumental drift is estimated, under the assumption of a linear-trending drift in time over a working day, all the gravity measurements of the same loop are corrected accordingly (Figure 5.4). By iterating this approach for every day of campaign, we obtain a relative gravity network, where the relative differences between each point of the network are fixed and which has to be tied to a known absolute reference point, to obtain absolute gravity values. As we connected our network of relative gravity measurements to already-established reference points maintained by swisstopo, we also defined our own local reference points in strategical areas for a convenient gravity loop organisation. These local reference points were connected to the same absolute reference points as well. The already established absolute reference points we relied on were those of Altdorf, Andermatt, Oberalp Pass and Biasca. We have installed two temporary reference points with fixed markers, one in Amsteg, one at the Lukmanier Pass. Ultimately, the entire new gravity dataset is linked to the same reference system as the points in the tunnel.
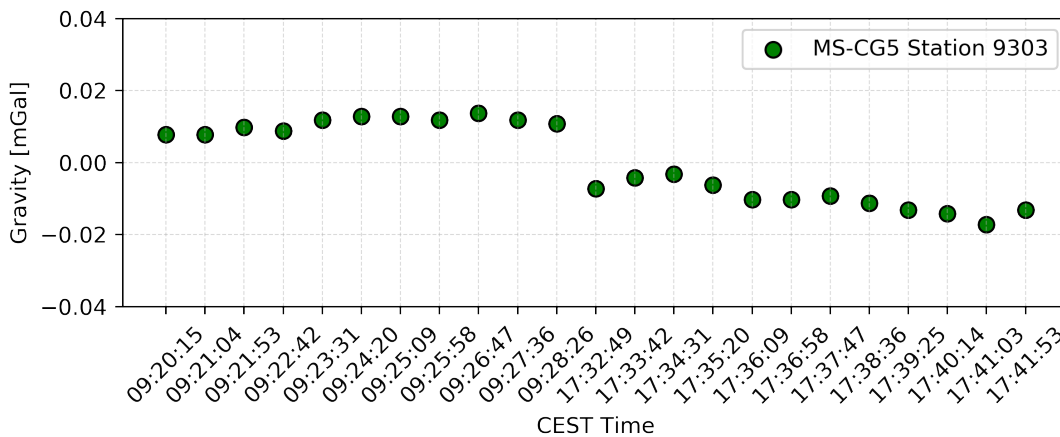

Figure 5.4 – Repeated relative gravity measurements at station 9303, which has been used to open and close a measurement loop during day of the campaign. At each visit at any of the measurement points, repeated measurements are taken. In this case, measuring both in the morning (at ~ 9.30 AM) and in the evening (at ~ 17.30 PM) allowed to estimate the instrumental drift as the systematic shift between the morning and the evening measurement series. In this case, the instrumental drift is of ~ 0.02 mGal. This value is then used to correct all the measurements of the same day assuming a linear trend of the drift with time.

5.3.3 Elevation estimate and gravity pre-processing

For each gravity point, the elevation estimate at the measurement site is of fundamental importance for the subsequent data processing and modelling, as each meter of vertical displacement in the free atmosphere corresponds to a gravity change of ~ 0.3086 mGal. As for the previous campaigns in Ivrea, a stand-alone GNSS (Global Navigation Satellite System) TopCon receiver antenna has been used to measure the elevation at each site. The satellite signal was recorded for ~ 20 minutes at 1 Hz sampling rate and the ellipsoidal height was obtained via the PPP (Precise Point Positioning) free processing tool from Natural Resources Canada (https://webapp.geod.nrcan.gc.ca/geod/tools-outils/ppp.php). The PPP processing tool provides processed coordinates in the WGS84 reference frame with ellipsoidal heights, with vertical uncertainties typically of 0.5 m for our acquisition habits (i.e., satellite signal recorded for 15 to 20 minutes at each location), hence corresponding to 0.15 mGal uncertainty on the gravity. To obtain physical heights, consistent with the local digital elevation model *swissAlti3D*, I used the online tool REFRAME from swisstopo (https://www.swisstopo.admin. ch/en/maps-data-online/calculation-services/reframe.html), which allows to convert WGS84 data to the Swiss cartesian reference system (LV95) with the physical height system (LN02). Finally, the mean difference between our final elevation measurements and the *swissAlti3D* digital elevation model at the same location is 0.73 m with 0.35 m as median.

The raw gravity data, organised into ordered daily loops, was processed with GRAVPROCESS software (Cattin et al., 2015) to obtain absolute gravity values. The software allows for proper averaging of the repeated gravity measurements at each site, and removes the time-dependent gravity effect of tides, to finally connect the relative network to the absolute reference points. The mean standard deviation associated with the gravity measurements is 0.063 mGal while the instrumental daily drift was always below 0.1 mGal. Free-air correction and latitude corrections were also computed and applied as described in paragraph 5.5.1. GRAVPROCESS also allows to compute Bouguer gravity anomalies in case one wants to investigate anomalous gravity signal generated by crustal sources, therefore removing the effect of the surrounding topography and terrain variations. As in this study I investigate the gravity effect associated with lithological structures between the surface and the sea level, I did not compute any Bouguer anomaly but I have adapted the same GRAVPROCESS routines for the direct gravity modelling as described below.

5.3.4 Projection to the 2D model profile

To consistently associate a 2D forward modelling result to the geological units digitized from the GBT profile, the digitized geological units were projected onto a straight line, defined as the connection between the tunnel's northern and southern portals. Coordinates are shown in Table 5.2. From now on, I will refer to this straight projection line as the reference **model** line, which corresponds to the cyan line in Figure 5.3.

Portal	Lon.°E	Lat.°N	Y(LV95)[m]	X(LV95)[m]
North	8.64641	46.83597	2'692'137	1'187'912
South	8.92568	46.37252	2'714'406	1'136'768

Table 5.2 – Location of the Gotthard Base Tunnel's southern and norther portals, which have been used to define the starting and ending point for the 2D model projection.

The digitized geological units have been projected perpendicularly to the reference model profile connecting the two portals. The mean projection distance is 1.486 km with median 1.413 km, while the final straight-line distance between the two tunnel portals is 55.783 km. In this phase, and important model adaptation step was implemented. The projected geological units have also been adjusted to the model topography. Consequently, the units were either truncated to adapt to the lower elevation model topography, or vertically extended along the unit boundaries up until the model topography (Figure 5.5).
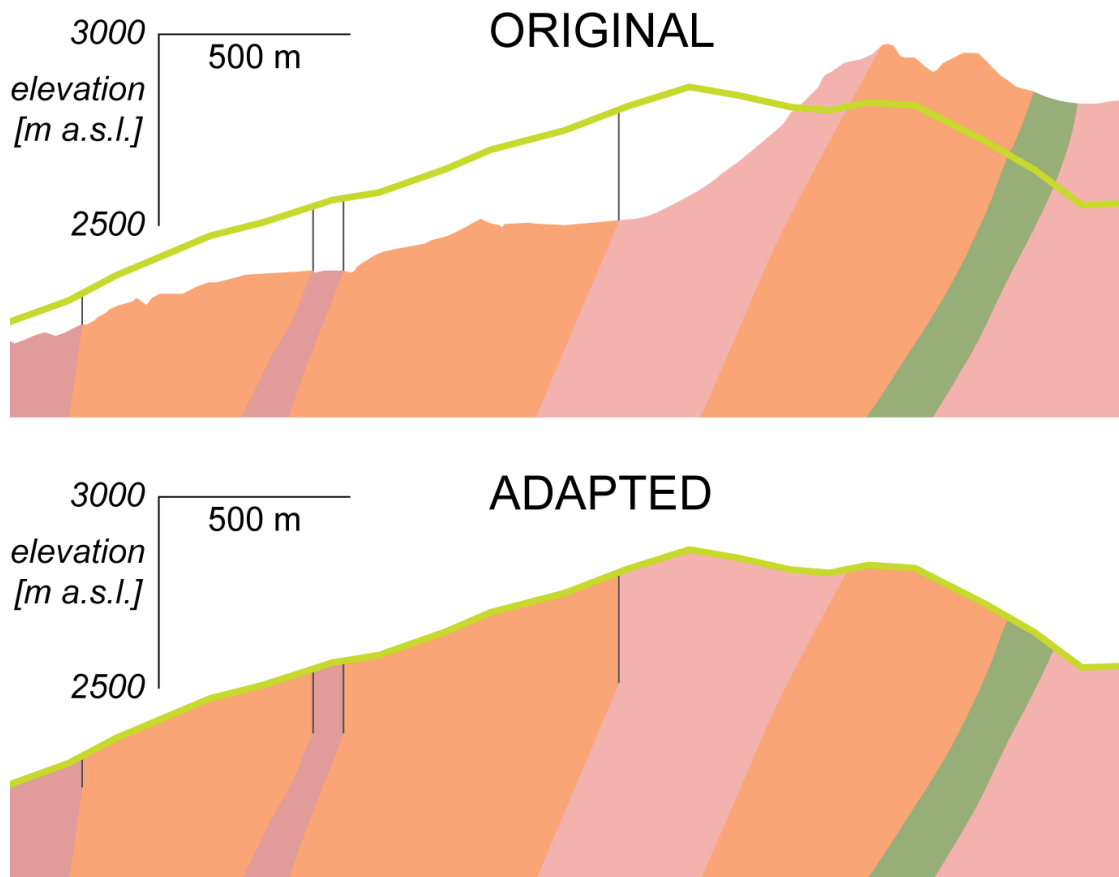
Figure 5.5 – Adaptation of the original GBT geological profile to the reference model's topography (green line). One of the following two steps is performed. If the target topography is higher than the original, lithological boundaries are vertically upward continued (thin black lines), and the geological units (coloured) extended and "filled" with the same rock (left side of the sample section). In the contrary, the units are simply truncated at the target topography (right side of the sample section). This example is shown without vertical exaggeration, above 2000 m elevation, and is located at the centre of the profile; the highest peak in the original profile is near Piz Vatgira (2982 m), the highest peak in the reference model is near the 2888-m peak west of Piz Gannaretsch.

This operation was carried out manually, to match the model's topographic profile which is subsequently modelled with gravimetry. This procedure finally produced 62 bedrock units and 2 Quaternary units in total. While these model geometry adaptations may seem to be venturesome choices, the gravity data processing follows the same logic, in order to bring all surface and tunnel gravity points onto the model profile, both horizontally and vertically (Figure 5.6). The gravity processing steps and effects due to this projection are accounted for and discussed in paragraph 5.5.3.
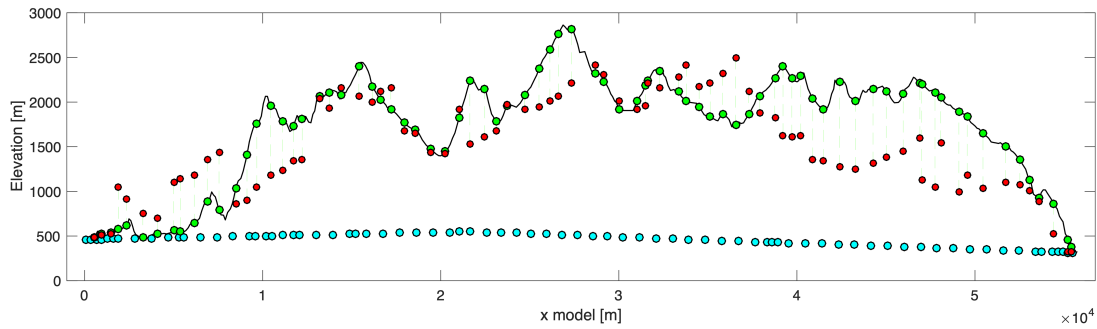
Figure 5.6 – 2D topographic profile along the reference model line (see location in cyan line in Figure 5.3 map), together with the projected tunnel gravity data points (cyan circles) and the projected surface gravity data (green circles). The surface gravity measurement points at their original measurement location are shown as red circles. Prior to comparison with synthetic values, computed at the projected locations (green circles), the gravity data points are corrected for the effects due to this projection. The procedure is explained in detail in paragraph 5.5.3.

5.4 2D gravimetric forward modelling

The forward gravity modelling consists of computing the gravity effect of a given density distribution at a certain point in space, as a function of the point's respective distance from the gravity sources. In this work, I aim at testing the gravity effect of 2D lithological units of various density, defined according to the 2D Gotthard Base Tunnel geological model. Therefore, the forward problem computation can be substantially simplified with respect to the general three-dimensional case by employing equations assuming a 2.5D structure, with the geometry extending unvaried along the third spatial coordinate (perpendicular to the profile). Under this assumption, each lithological unit can be described as a closed two-dimensional polygon of homogeneous density.

It has been shown in the literature that the gravitational attraction of a two-dimensional body can be expressed as a line integral along its perimeter (Hubbert, 1948). This was later implemented by various authors, providing explicit formulas for the computation of the horizontal and vertical gravity components due to a N sided polygon of constant density (Talwani et al., 1959; Won and Bevis, 1987). These formulas have been implemented in a home-grown MATLAB software called GRANOM (Hetényi, 2007), which allows to compute gravitational effects both outside and inside input density distributions, therefore providing in a straightforward manner the synthetic gravity data both at the surface and inside the tunnel. Eventually, the horizontal and vertical components of the gravity anomaly for a N-sided two-dimensional polygon of given density can be written as:

$$\Delta g_z = 2G\rho \sum_{i=1}^{n} Z_i \tag{5.1}$$

98

and

$$\Delta g_x = 2G\rho \sum_{i=1}^{n} X_i \tag{5.2}$$

where G is the gravitational constant, ρ the polygonal element's density, Z_i and X_i the line integrals associated with the i-th side of the polygon. The reader is referred to Won and Bevis (1987) for the explicit formulation of Z_i and X_i, which represent purely geometrical factors determined by relative location of the polygon vertices with respect to the point at which the gravitational attraction is computed. The linearity of the gravity field with respect to density, for a fixed geometry, constitutes a remarkable advantage in terms of computational resources as long as the geometries are kept fixed. In fact, it allows to compute once the gravity effect of a given body (Z_i and X_i), and then to scale it linearly with density without additional computational burden. This is true also in a general three-dimensional case, and will turn out to be a key advantage for computing the 3D density-dependent terrain corrections as described in the next section.

As the field observations only measured the vertical component of gravity, the computations of the subsequent model tests were performed for Δg_z.

5.5 Testing a density model

In this section I present the procedure I implemented and ran to test a given 2D Gotthard Base Tunnel geological model with assigned density values, by means of comparison between field gravity observations and the associated forward gravity modelling in 2D. To this purpose, two main points had to be addressed:

1. How to correct field gravity observations, which are sensitive to a complex 3D-varying topography together with subsurface structures,

2. How to account for the prescribed GBT test density model in this correction.

Paragraph 5.5.1 describes how the measured absolute gravity data is pre-processed prior to the projection from the 3D *world* to the 2D *model* for comparison with synthetics; paragraph 5.5.2 describes the numerical mesh I defined to sample the topography for the terrain correction calculations, and finally paragraph 5.5.3 describes the new terrain-correction, including translation to the 2D model topography, that I defined and applied, and call terrain-adaptation correction.

5.5.1 Classical gravity corrections

The field gravity observations can classically be corrected for a number of factors prior to be corrected for the terrain effect and compared to the synthetics obtained from a 2D model. As

the final purpose here is to test a density model distribution spanning from the surface to 300 m above sea-level, it is not in our interest to compute a Bouguer gravity anomaly (which would remove the whole effect of the topographic masses with the constant density of 2670 $kg \cdot m^{-3}$), but only to account for the difference between the 3D *real world* and the 2.5D topographic model derived from the 2D Gotthard Base Tunnel profile (already projected along the 2D model line, as explained in paragraph 5.3.4).

Therefore, the observed absolute gravity data have been corrected for the following factors:

- g_{Lat} **latitude correction**: this correction accounts for the Earth reference gravity field $g_0 \sim 9.78 m \cdot s^{-2}$, associated with the reference 0 m elevation at sea-level, especially its variation with latitude, due to the Earth ellipticity;

- g_{FA} **free-air correction**: this correction accounts for the measurement point elevation with respect to sea level and partially balances the latitude correction by taking into account elevation: for every meter of vertical upward displacement in the free atmosphere the reference gravity field decreases by 0.3086 mGal;

- $g_B A$ **regional trend correction**: this correction accounts for the regional trend of the Bouguer gravity anomaly field, available from the regional map (1:500'000 scale, 2 mGal contour line) of swisstopo. The regional field accounts for crustal changes below sea-level, and is mainly shaped by the major Moho depth change across the Europe-Adria plate boundary. For this, the regional Bouguer trends was sampled along the tunnel profile and interpolated with a 2nd order polynomial. The model profile crosses the most negative parts of the regional Bouguer anomaly map, with a flat-plate shape along the profile and relative amplitude change on the order of 10 mGal.

5.5.2 Numerical mesh for sampling topography

A proper evaluation of the gravity effect of the 3D topography is of primary importance for the subsequent density-dependent gravity corrections, required to project the field gravity measurements to the 2.5D structure defined by the 2D Gotthard Base Tunnel profile. The numerical mesh used in the computation is an ensemble of points over which the digital elevation model (either swissALTI3D or SRTM, depending on the required resolution) is interpolated. A digital elevation model is usually delivered on a regular grid, which is not directly suitable for the numerical computation of the desired gravity corrections, as it would require too much computational power. Furthermore, as the effect of gravity decreases with the square of the distance, a constant resolution is not required across the whole study area. While other authors in similar contexts defined a mesh of dynamically decreasing resolution for each processed gravity point (e.g., Cattin et al., 2015), for this application I defined one dedicated, static mesh with several zones of spatial node density (Figure 5.7). The mesh is denser around each gravity point and along the model and the tunnel track lines, while its resolution decreases with distance away from this area. Most importantly for the subsequent testing of different density models via gravity modelling, the mesh includes lines of nodes

representing the surface projections of all considered geological unit boundaries, as prescribed from the adapted Gotthard Base Tunnel geological profile. This allows to compute the effect of each 2.5D geological model unit's structure. The geometries of these units are kept unchanged until they can be proven unsatisfactory. Such a consideration of lithological units allows to evaluate the effect of various density models easily via simple linear scaling.
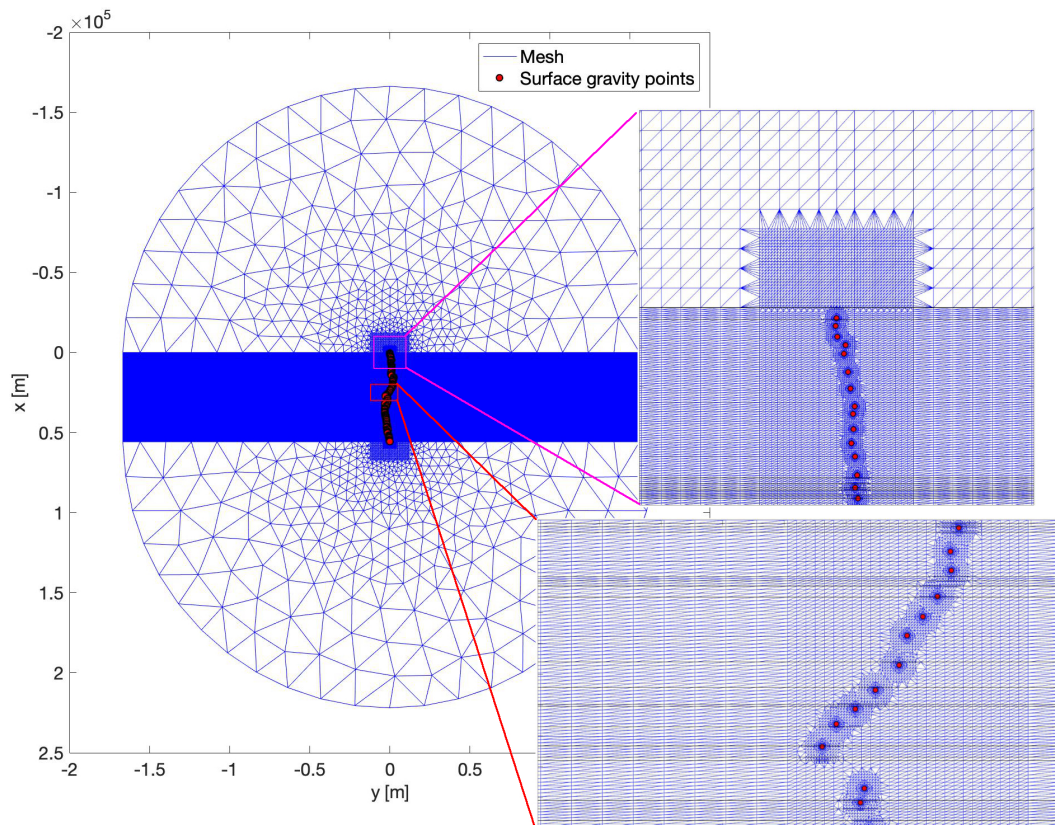

Figure 5.7 – Graphical representation of the numerical mesh used for the density-dependent gravity correction computation. The digital elevation model (either swissALTI3D or SRTM) depending on the required resolution) is sampled at each mesh node and subsequently used for the computations. The resolution of this static mesh is higher (10 m) in the vicinity of the gravity measurement points (red circles) and along the reference model line (including the original GBT track as well), while it decreases with increasing distance from this central zone. The two insets show the varying spatial resolution for two particular areas, along the reference model line and at around the northern tunnel portal. The thin horizontal black lines in the two insets mark the surface boundary between each geological unit digitised from the GBT geological profile, which were included as a line of nodes in the mesh. It is of fundamental importance that the mesh respects these boundaries, allowing for a correct and consistent density mapping from the 2D profile to the 3D structures for the computation of the terrain gravity corrections.

5.5.3 3D-to-2D density-dependent terrain-adaptation correction

The most critical and novel correction to apply is a density-dependent terrain correction and simultaneous topography-adaptation prior to comparing the observations with the synthetics obtained for the 2D GBT density model. This correction accounts for the gravity effect due to the difference between the 3D *real-world* topography, where the gravity measurements have been taken, and the 2.5D structure that the forward gravity modelling accounts for (as the synthetic gravity signals are computed along the reference model's topography, and not at the original gravity measurement points). For each gravity point, this terrain-correction is computed as a sum of unit-wise contributions, where individual 3D units have been defined by extending the 2D geological profile along the profile-perpendicular space coordinate. It should be noted that the 3D unit blocks have vertical boundaries, which match the surface expression of the 2D geological units.
Therefore, for each gravity point, the density-dependent terrain-adaptation correction (TAC) is defined as:

$$g_{TAC} = \sum_{j=1}^{N} \rho_j \cdot (CBC_{2.5D}^{f} - CBC_{3D}^{i}) \tag{5.3}$$

where N is the total number of geological units, each of which is assigned with a density value $\rho(j)$ prescribed by the 2D geological model, CBC_{3D}^{i} is the complete Bouguer correction computed for the original 3D topography at the **_i_nitial** gravity measurement point location (Figure 5.8), and $CBC_{2.5D}^{f}$ is the complete Bouguer correction computed for the 2.5D structure defined at the **_f_inal**, projected points, located along the 2D geological model's topography line (Figure 5.9). With this approach, the classical terrain correction and the translation of observations points to the model profile, including the new topography, are realized in the same step, all considering density-dependent lithological units.
The final, observed gravity product, ready for the comparison with the synthetic gravity values, is defined as follows:

$$g_{corr}^{obs} = g_{meas}^{obs} - g_{Lat} + g_{FA} - g_{BA} + g_{TAC} \tag{5.4}$$

where g_{meas}^{obs} is the absolute gravity value obtained from field measurements and classical processing (as described in paragraph 5.3), g_{Lat}, g_{FA} and g_{BA} the latitude, free-air and regional trend corrections described in paragraph 5.5.1, and g_{TAC} the density-dependent terrain-adaptation correction for the translation of surface gravity measurement to the 2D reference topographic profile. The same procedure is applied both for the surface and the tunnel gravity measurement points, with the only difference that the tunnel points are projected along the 2D model line keeping their initial elevation.
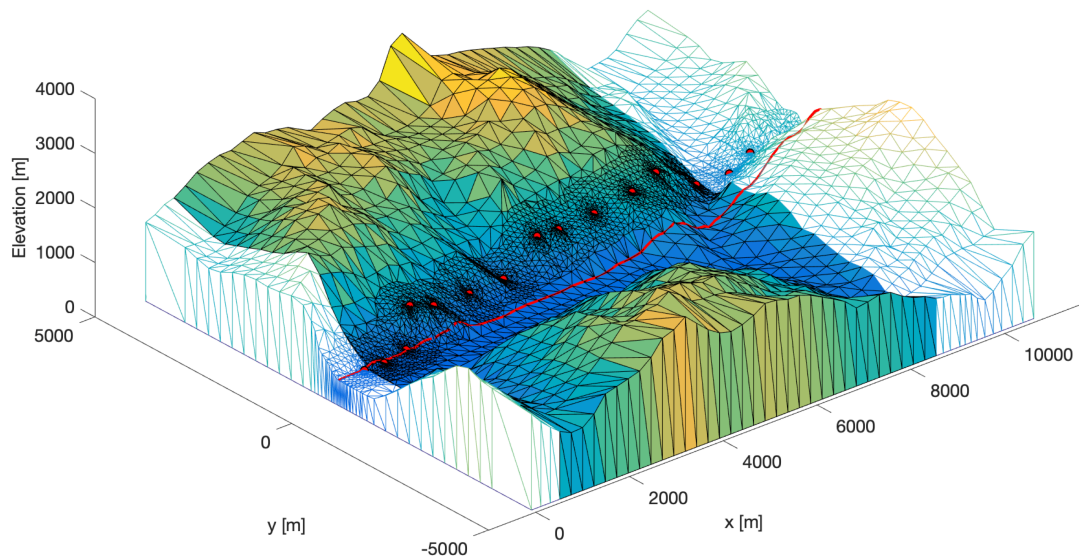
Figure 5.8 – Initial *real world* situation at the northern tunnel portal. The 3D topography is interpolated at mesh nodes from the *swissALTI3D* DEM. The coloured topographic mesh is associated with a single unit as indicated by the 2D GBT geological profile, while the neighbouring units are shown with coloured mesh edges only. The mesh resolution is higher in the vicinity of the surface gravity measurement points (red circles) and in the vicinity of the reference model line (red line), which is by definition at y = 0 m along the whole study area. The topography sampled along the model line corresponds to the reference model topographic profile, and it is the same profile to which the geological profile was adapted, and which is used for the synthetic gravity computation.
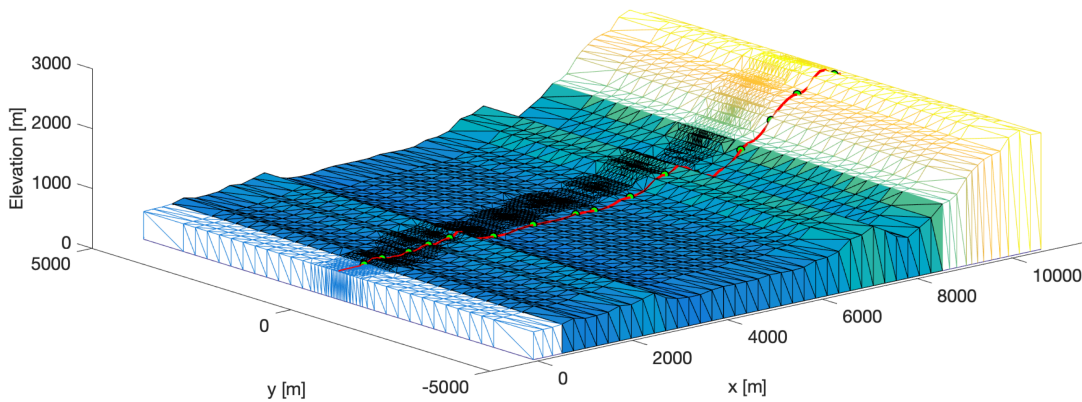
Figure 5.9 – Final, adapted *reference model* situation at the northern tunnel portal. View of the 2.5D topography as laterally continued from the 2D reference model line topographic profile (red line). Same colouring scheme as in Figure 5.8. This 2.5D structure is correctly accounted for by our forward gravity modelling routine, which neglects any topography variation along the profile-perpendicular coordinate (Won and Bevis, 1987). The red line following the topographic profile at y = 0 m represents the 2D reference model line, to which the observed gravity measurements are translated (green circles) prior to the comparison with the synthetic values.

5.6 Results

The proposed density models (paragraph 5.2.2) have been tested by comparing the associated 2D forward gravity model's signal with the gravity observations corrected using the same density models (equation 5.4). Each density model has been tested separately, for both the surface and the tunnel gravity datasets, and its performance in terms of fit of the synthetics to the observations has been quantified by computing the root-mean-square error:

$$
rms^{surf,tunnel}_{model} = \sqrt{\sum_{i=1}^{N} \frac{(syn_i^{surf,tunnel} - obs_i^{surf,tunnel})^2}{N}} \tag{5.5}
$$

where N is the number of data points running with index i, superscript *surf* and *tunnel* represent the surface and tunnel points. The obtained misfits for the tested density models are shown in Table 5.3.

Model	surface rms [mGal]	tunnel rms [mGal]	Total rms [mGal]
Model 1	2.83	3.85	3.37
Model 2	2.80	3.63	3.23
Model 3	2.76	3.81	3.31
Model 4	3.34	3.21	3.79
Model 5	8.82	8.67	8.75
Model 6	4.44	4.71	4.57
Model 7	2.66	3.93	3.35

Table 5.3 – Root-mean-square error obtained by comparing synthetic forward modelling and corrected gravity observations, for both surface and tunnel data. Model 7 is a constant density model for all units ($\rho = 2700 kg \cdot m^{-3}$).

Model 2 seems to yield the best total rms, however Models 3,7 and 1 are also very close to it. The misfit is also represented by point-wise difference between synthetic and observed gravity anomaly values, both for surface and tunnel gravity data (Figure 5.10 and Figure 5.11 respectively).
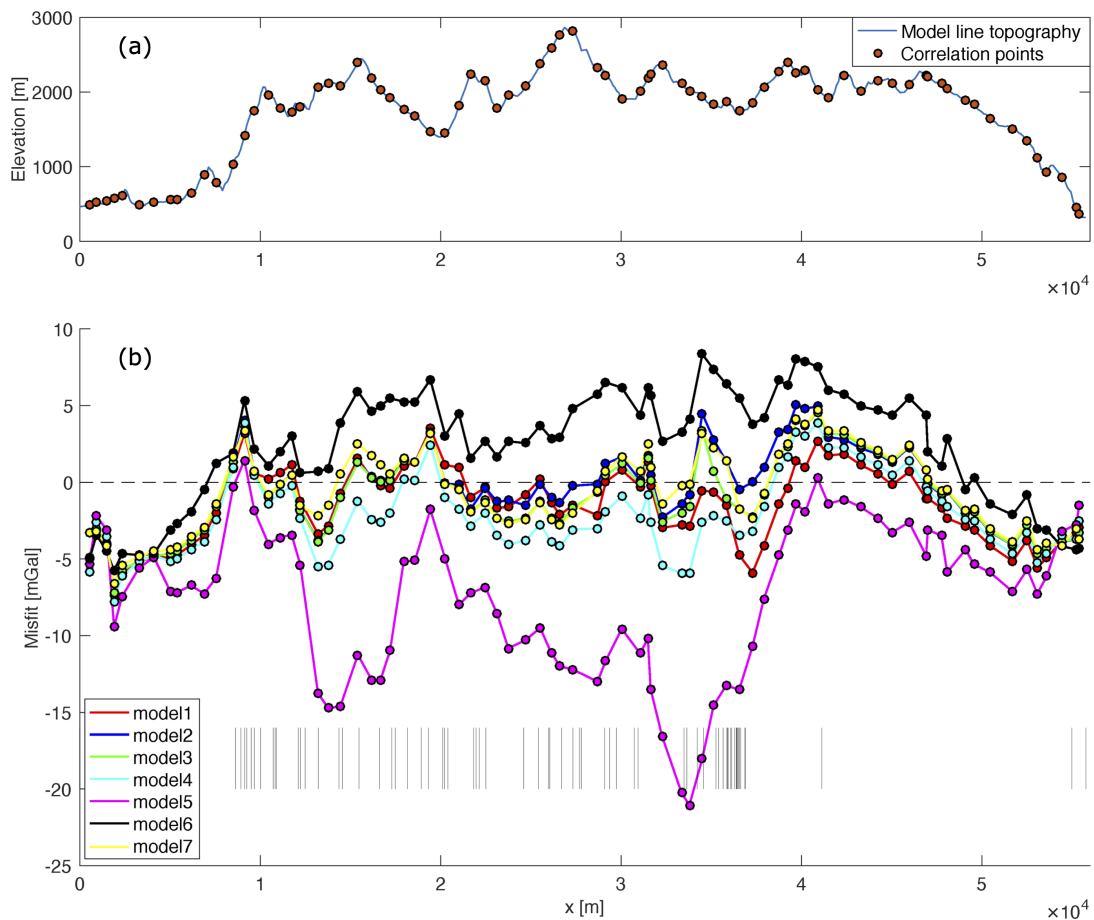
Figure 5.10 – Point-wise misfit for the **surface** gravity data points and topographic profile. (a) The topographic profile along the reference model line (blue line), together with the projected gravity data points at the surface (orange points). These points have been used to sample the topographic profile and compute the cross-correlation between topography and misfit. (b) Point-wise misfit for the surface gravity data points, for each of the tested density models (see colour legend), as described in paragraph 5.2.2. Model 7 features constant density (2700 $kg \cdot m^{-3}$) for all the geological units. Black thin lines in the lower part of the figure, indicate the location of the geological unit boundaries at the surface, along the profile. The point-wise misfit represented in the figure is defined as synthetic minus observed.
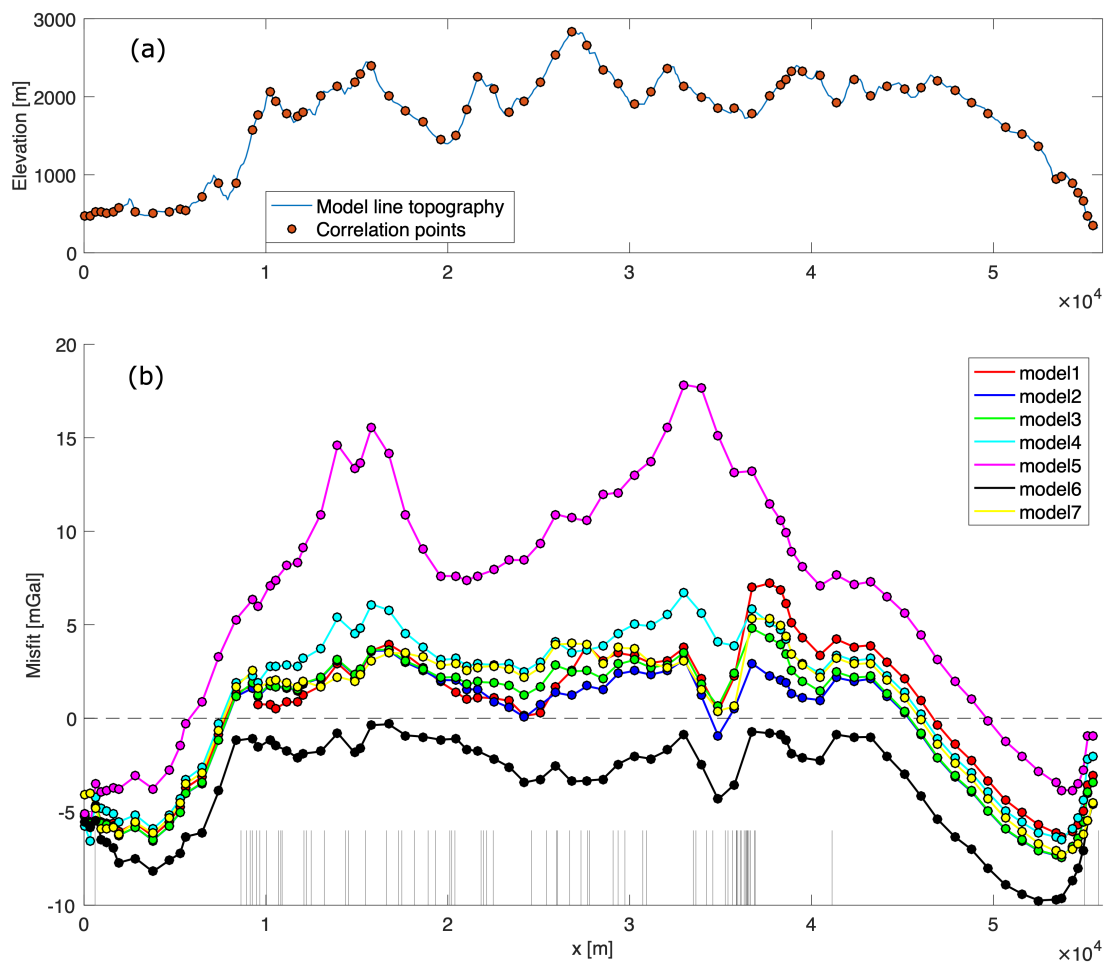
Figure 5.11 – Point-wise misfit for the **tunnel** gravity data points and topographic profile. (a) The topographic profile along the reference model line (blue line), together with the projected gravity data points at the surface (orange points). These points have been used to sample the topographic profile and compute the cross-correlation between topography and misfit. (b) Point-wise misfit for the tunnel gravity data points, for each of the tested density models (see colour legend), as described in paragraph 5.2.2. Model 7 features constant density (2700 $kg \cdot m^{-3}$) for all the geological units. Black thin lines in the lower part of the figure, indicate the location of the geological unit boundaries at the surface, along the profile. The point-wise misfit represented in the figure is defined as synthetic minus observed.

As the overall shape, long wavelength of the misfit curves (Figures 5.10b and 5.11b) seems to reflect the model topography, their correlation has been quantified. This has been computed as the zero-shift cross-correlation, according to the formula:

$$xcorr(\vec{g}, \vec{t}) = \frac{\sum_{i=1}^{N} g_i \cdot t_i}{\sqrt{(\sum_{i=1}^{N} g_i \cdot g_i) \cdot (\sum_{i=1}^{N} t_i \cdot t_i)}} \tag{5.6}$$

where $\vec{g}$ represents either the surface or the tunnel gravity misfit points and $\vec{t}$ represents the topography, sampled at the same x-coordinates as the surface respectively tunnel gravity points along the model line (see locations on Figures 5.10a and 5.11a). The results obtained from the application of Equation 5.6 are shown in Table 5.4.

Model	surface-topo xcorr	tunnel-topo xcorr
Model 1	-0.340	0.324
Model 2	0.014	0.088
Model 3	-0.142	0.197
Model 4	-0.500	0.466
Model 5	-0.844	0.842
Model 6	0.728	-0.593
Model 7	-0.019	0.292

Table 5.4 – Zero-shift cross-correlation values of the surface and the tunnel gravity misfit with topography for each density model. To compute the cross-correlation, the topography along the model line has been sampled as the same x-coordinate as the gravity data, as shown in Figures 5.10a and 5.11a.

Similarly to what is argued for Nettleton's method (Nettleton, 1939;Nettleton, 1976), that is the optimal density for near-surface structures should provide the least correlation between Bouguer anomalies and topography, these correlations (shown in Table 5.4) may be interpreted as indicators of how well the local unit densities, used for both the observation corrections and the forward gravity modelling, fit the data and in turn relate to the real world density structures. Intuitively, models showing no correlation with the topography (cross-correlation closest to 0) can be considered as best performing models, and here again Model 2 shows the top performance. However, it should be noted that while these results already provide sound information on how the tested density models fit and explain the processed gravity observations, these should be still regarded as partially preliminary and further analysis is currently ongoing. This includes systematically investigating the effect of the mesh resolution on the TAC gravity correction, and hence its effect on the gravity misfit. Nevertheless, an estimate of this effect is already provided in paragraph 5.7.1. Ultimately, a systematic inversion for the best-fit density for each unit could be set up, which is made possible due to the stored geometrical factors and straightforward scalability of gravimetric effects with changing density.

5.6.1 Sensitivity tests

The density-dependent terrain-adaptation correction (TAC, equation 5.3) is computed as a sum of unit-wise contributions, which are linearly scaled according to the tested density model. As the unit geometries are heterogeneous and highly variable along the geological model, all the terms summing up to the final TAC vary as a function of the distance from the corrected gravity point and of the density they are associated with. This is here demonstrated taking middle-size example with quite variable density values according to the different models, the Piora Dolomite. The TAC associated with a density variation of $\sim 300\ kg \cdot m^{-3}$ for this unit, which presents a ~ 600m x 400m topographic adaptation from the 3D to the 2.5D model in the vicinity of the model line (Figure 5.12a), is causing a misfit variation of up to ~ 4 mGal for the nearest gravity point, gradually tapering down to negligible ca. 2 km away from this particular unit (Figure 5.12b).
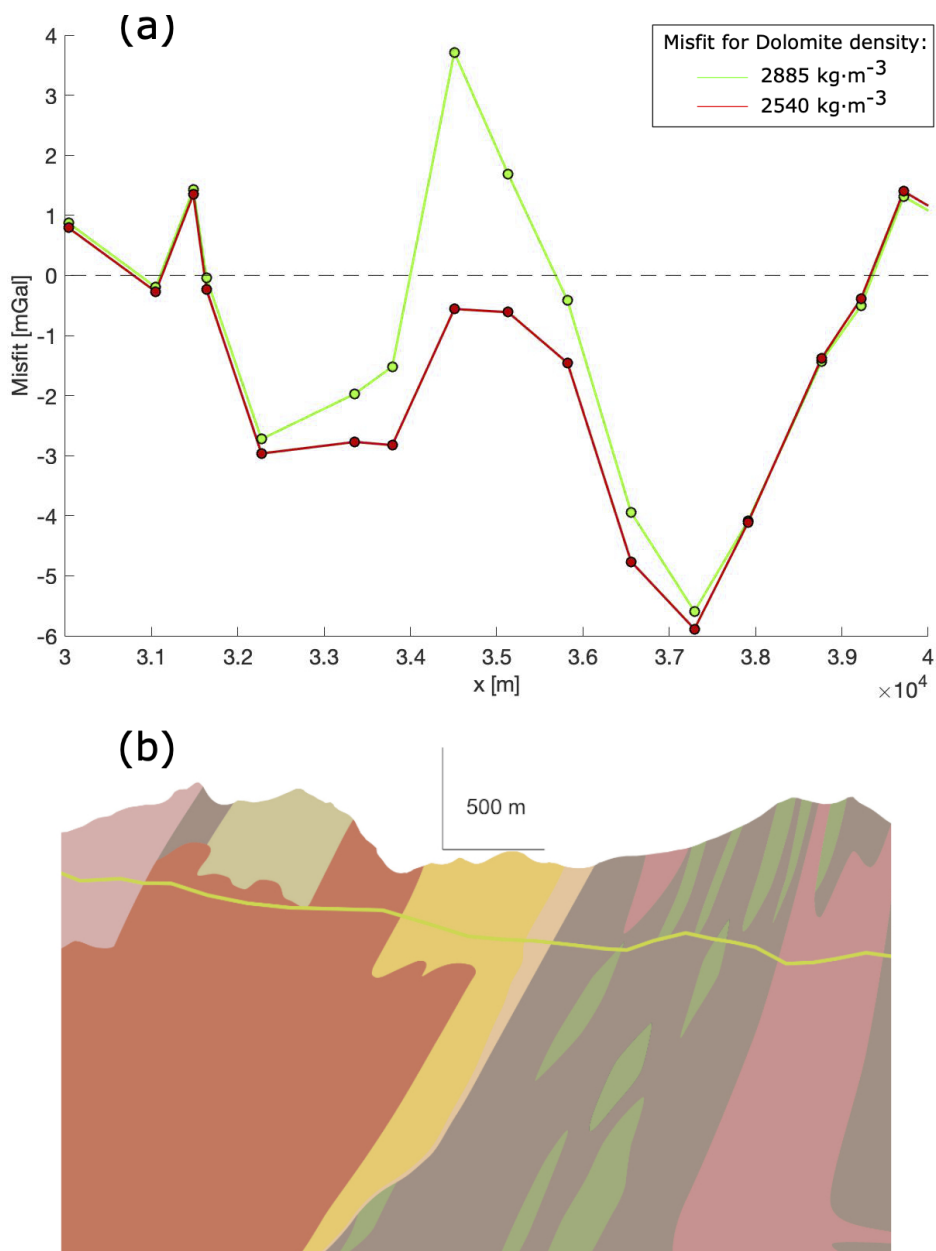
Figure 5.12 – Gravity effect due to a density variation of $\sim 300 \; kg \cdot m^{-3}$ of a middle size unit (Piora Dolomite), presenting a $\sim$ 600m x 400m topographic adaptation. (a) Gravity misfits, defined as the difference between synthetic and corrected observations, for a higher density value of 2885 $kg \cdot m^{-3}$ (green line and dots) and for a lower density value of 2540 $kg \cdot m^{-3}$ for the Dolomite unit (yellow unit in panel b). The remaining unit densities are unvaried. (b) Geological profile as projected along the straight reference model line. The green line is the reference topography, and separates the modelled geological units below and the original model that includes the parts above. The latter excess is removed and accounted for by the TAC correction in the transition from the 3D to the 2.5D model.

A more complete view of the magnitude of the TAC due to each unit and for a reference density of 1000 $kg \cdot m^{-3}$ is shown in Figure 5.13. This provides information on each unit's "geometrical" factor contributing to the TAC, which is mainly determined by the location of the projected gravity point along the 2.5D model line with respect to the surrounding original 3D topography. The widest units provide the strongest contributions, while the smaller units account for little corrections even for the nearby gravity points.
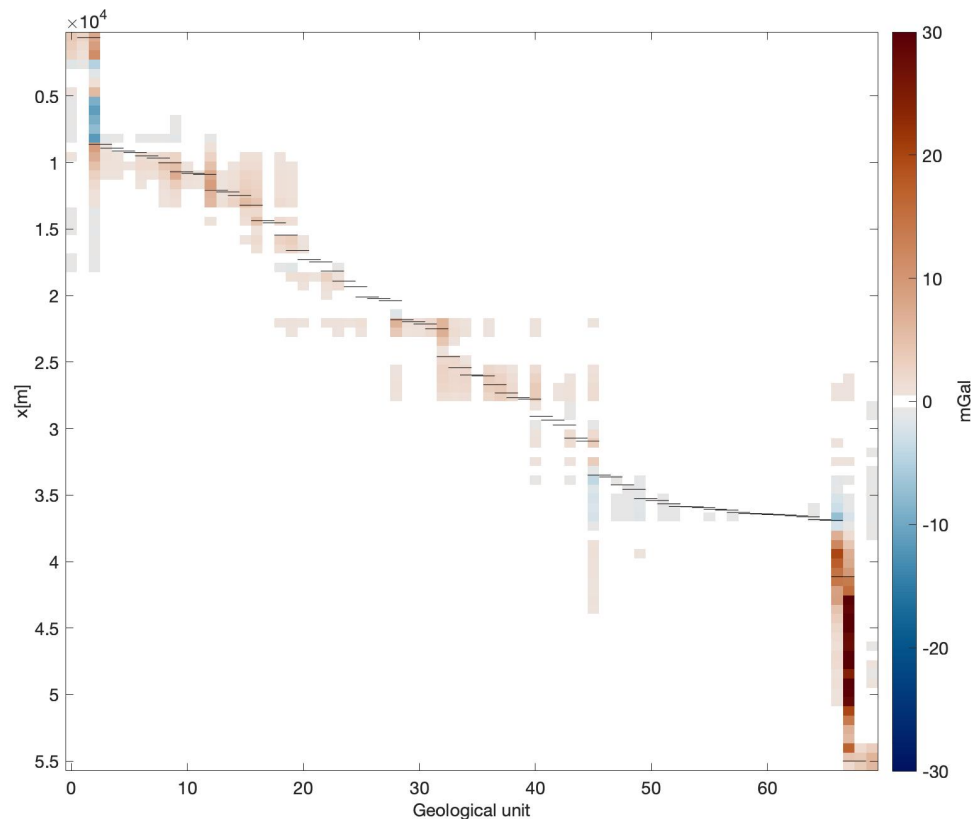

Figure 5.13 – Terrain-adaptation gravity correction due to each geological unit (ranging from North to South on the x-axis) and as a function of the selected gravity points (shown at their location along the model line on the y-axis). The gravity values shown here are for a reference density of 1000 $kg \cdot m^{-3}$. The variations depicted here depend on each unit's geometry and the distance between the unit and the selected gravity point. The mainly diagonal structure indicates that units tend to affect primarily the gravity points close by along the profile, with the exception of the widest units at the beginning and the end of the model line. For given units (i.e. along a single column) some gaps are present between non-zero values, due to the different elevation change between the unit and the gravity points. The thin horizontal lines, plotted for each unit along the y-axis indicate the northern and the sourthen boundary of the associated unit, hence showing how far beyond its own boundaries a geological unit is affecting the gravity points.

5.7 Discussion

5.7.1 Data and modelling uncertainties

In this sub-section, data and modelling uncertainties are discussed in two groups. Part of the uncertainties can be quantified via estimation of standard deviations, while other sources of uncertainties are well recognized but more difficultly estimated. Each gravity point's elevation measurement is associated with a standard deviation of 0.5m, which translates into a ∼ 0.15 mGal uncertainty on the gravity data. In addition to this, processing uncertainties are also associated with the raw-to-absolute gravity data processing. Standard deviations obtained from the GRAVPROCESS software are indicated in Table 5.5.

Mean Standard deviation	[mGal]
Absolute gravity values	0.06
Free air correction	0.016
Relative network adjustment	0.053
Absolute network adjustment	0.03

Table 5.5 – Mean standard deviations in mGal associated with the gravity data products obtained from GRAVPROCESS during the processing of the raw gravity data acquired in the field.

All the effects presented above account for a standard deviation of ∼ 0.3 mGal in total. Furthermore, a two-fold densification of the numerical mesh sampling topography provided a gravity misfit variation on the order of 1 mGal. However, further tests on the effect of the numerical mesh resolution are ongoing.

Other effects are source of uncertainty, but more difficult to quantify. First of all, the assumption of vertical geological unit boundaries for the TAC computation. While the geological model features mostly vertical to sub-vertical units, it presents unit boundaries deviating from the vertical as well, and which could not be accounted for in the numerical calculations. Moreover, the tunnel-perpendicular extension of each unit in a straight manner is a simplification. The limited vertical extension of the GBT geological model (from surface to 300 m above sea level) may also explain part of the negative misfit trend near the northern and southern tunnel portals, where the gravity points are very close to the 300 m line. A constant density of 2670 $kg \cdot m^{-3}$ was adopted for the rocks between sea-level and 300 m above sea level, in order to stick to the published model and to avoid making assumptions. The effect of light Quaternary sediments is difficult to quantify as well, as their density can be highly variable, and they surely influence the data near the tunnel portals where they exceed 100 m thickness, although only within the valley.

Overall, and considering the cumulative effect of these aspects, it seems reasonable to interpret few mGal variations, without addressing sub-mGal features, which seems to be an acceptable level for a model simplified into 2D.

5.7.2 A quest for the best model?

The results presented in paragraph 5.6 already provide a base of quantitative information on how the different tested density models compare with respect to the gravity observations. It appears clear from Tables 5.3 and 5.4 that models 5 and 6, which have been defined to represent the lower and upper bounds for each lithology's density, can really be regarded as end-member models. It is also possible to see that between models 3 and 4, which have been defined by averaging the density values for the main lithologies respectively from local and regional samples, the local data (model 3) provide better fit. Including higher density variability based on local samples (models 1 and 2) yield some gain in the fit, model 2 being numerically the best. Still, models 1 to 3 present relatively small differences in terms of rms and cross-correlation value, and their relative differences are close to the uncertainty of the data and the processing. Model 7, with a homogeneous density value of 2700 $kg \cdot m^{-3}$ for all the units, provided the best rms fit and second best no-correlation result for the surface gravity observations but performed much worse for the tunnel gravity observations.

By looking at the point-wise data misfits (Figure 5.10 and Figure 5.11), it is also possible to notice that there is no single density model providing a systematically better misfit along the whole profile. While it appears clear that density contrasts are required to fit both surface and tunnel gravity data sets and that diverse *in situ* density information (SAPHYR) provide a better fit to the data, it is not yet possible to state wether one of the tested models should be considered as the best density model for the GBT geological profile. Nevertheless, further elements can be considered to reduce the circle of the well-fitting models and to improve individual unit's best density estimates. Focusing on particular units may be of interest, for example by looking at the surface gravity misfit curve at ∼ 47 and 47.7 km distance. There, model 5 and model 6 present short-wavelengths symmetric steps (Figure 5.14), which strongly correlate with the original surface gravity point elevations acquired nearby but at different elevations. These steps do not appear in the other four, better fitting models, and making the profile as smooth as possible could be set as a target.

Further work is currently ongoing to verify both long-wavelength and short-wavelength features: the negative misfits near the tunnel portals compared to positive in the central parts, respectively the local switch in the order of the best performing models in the vicinity of the portals, in particular for the surface gravity data (Figure 5.10). This latter feature may be due to the limiting assumption of a 2.5D model and/or to the limited depth extent of the geological model. Eventually, the gravity correction presented in paragraph 5.5.3 can be implemented in an iterative inversion algorithm, where the ensemble of all the possible density models are explored and characterised, providing more information on the resolution.
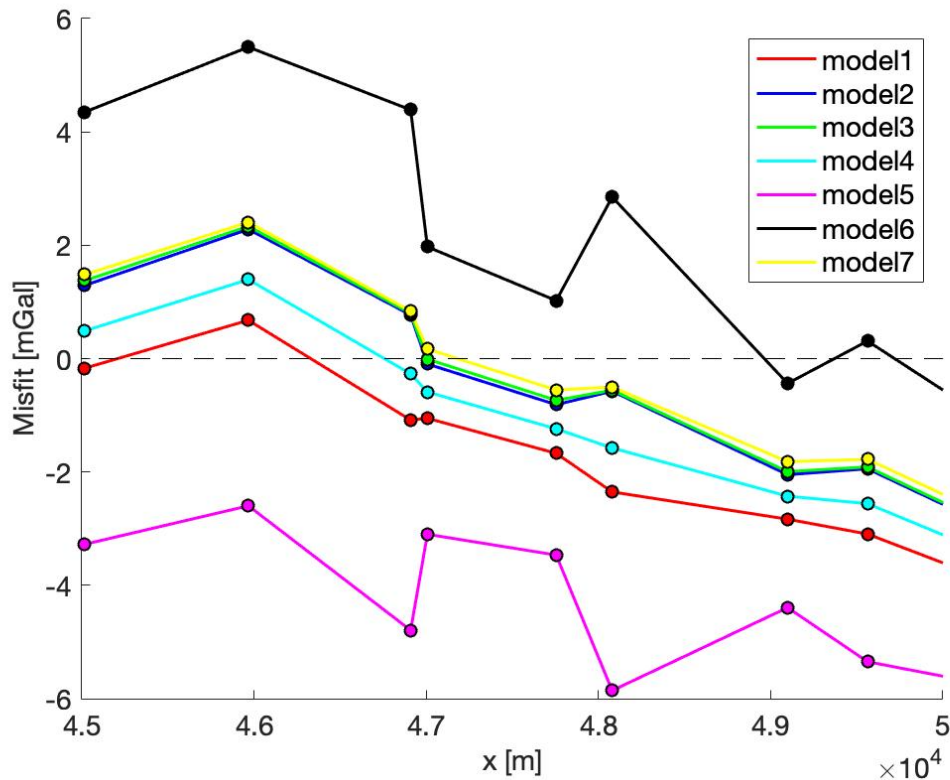
Figure 5.14 – Point-wise misfit for the surface gravity data points, with a focus on the 45 to 50 km section along the model line. Model 7 features constant density (2700 $kg \cdot m^{-3}$) for all the geological units. Models 5 and 6 present present short-wavelenghts symmetric steps, which strongly correlate with the original surface gravity point elevations acquired nearby but at different elevations, and which do not appear for the other density models. The point-wise misfit represented in figure is defined as synthetic minus observed.

5.8 Conclusions

I have collected 80 new gravity data points along the Gotthard Base Tunnel track at the surface, and combined them with 77 existing gravity data points measured inside the tunnel at the time of its construction. For the dual purpose of testing a geological profile and developing a new gravimetric processing scheme, I adapted the along-tunnel geological profile, associating each geological unit to a lithology with density data from the SAPHYR catalog, and defining a series of density models to test. Both the geological and gravimetric information have been projected and adapted onto a 2D reference model, to consistently perform forward gravity modelling and comparison to the observations. I developed a fully 3D, density-dependent terrain-adaptation correction, as part of the 2D model preparation, which is applied prior to comparison between the observations and synthetics, and whose contribution has been quantified for all the considered geological units. The analysis of the gravity data misfits indicates that density information obtained from in situ rock samples provide in general a better fit, rather than

average density values from the broader Alpine domain for the same lithologies. The best fitting model, for the ensemble of the surface and tunnel gravity points, presents also the lowest correlation with the model topographic profile. Short-wavelengths variations along the gravity misfit curves can be explained as well, and could be further exploited. Nevertheless, data and modelling uncertainties suggest not to interpret sub-mGal variations. Eventually, a more systematic exploration of possible density models can be applied, together with a better quantification of the topographical mesh resolution and related uncertainties. Overall, the geological structure proposed during the construction of the Gotthard Base Tunnel can be well fit with the density values available for most of the local lithologies.

5.9 Acknowledgements

6 Conclusions

In the frame of this thesis, I have collected and analysed new seismic and gravity data, to investigate intra-crustal geophysical anomalies and to test shallow crustal geological models by means of geophysical data. Across the target areas of the Ivrea-Verbano Zone and along the Gotthard Base Tunnel, the newly collected geophysical data provided a final coverage of unprecedented resolution compared to previous studies, bridging the resolution-gap between lithospheric geophysical investigations and sub-km-scale surface geological observations, which affected the interpretation of numerous previous studies in the Alpine domain.

In my first, published study, I collected 207 new relative gravity data points across the Ivrea-Verbano zone, to investigate the density crustal structure of the well-known Ivrea geophysical body, both at a higher resolution than before and in a novel way. In fact, I processed the gravity data to obtain the Bouguer gravity anomaly field, whose pronounced positive peak well represents the subsurface dense anomalous structure, and I defined the Niggli correction: a density-dependent gravity correction which accounts for the effect of the observed surface density variations in the area, associated with the lower to middle crustal outcrops of the Ivrea-Verbano zone. The Niggli correction extends the surface geological observations from surface to sea level and its magnitude can reach up to 30 mGal. Modelling the Niggli gravity anomaly considers the surface density information provided by previous geological studies, and therefore allows to address the crustal density structure of the Ivrea geophysical body more properly.

I modelled the body as a single, 3D density-contrast interface beneath the Ivrea-Verbano zone: the model presents an optimal density contrast of 400 $kg \cdot m^{-3}$ with respect to the background crustal structure and it supports the presence of a dense body located very close to the surface, as shallow as 0 to 2 km below the sea level. Further sensitivity tests suggest a plausible density contrast range of 300 to 500 $kg \cdot m^{-3}$ and a spatially sharp density gradient (< 4 km), with the relatively denser model presenting a narrower and slightly deeper interface with respect to the lighter one.

The interpretation of these results, in light of the geological knowledge of the area, allowed also to distinguish among possible candidate rocks for the Ivrea geophysical body composition. Considering a natural increase of densities with depth, which is a reasonable assump-

tion for the continental crust, and the metamorphic grade of the area, which presents high-temperature metamorphism in the southern Alps (to which the body structurally belongs) and high-pressure metamorphism in the western Alps, felsic and high-pressure metamorphic rocks (eclogites) were excluded as main composing rocks of the Ivrea geophysical body. Instead, mafic or ultramafic plutonic rocks are the most likely components for the lithology of the body. I brought these results directly into a more detailed petrological analysis of plausible rock types, including constraints from local earthquake tomography, which allowed me to discuss further with petrologists (Pistone et al., 2020).

For my second, published study, and in addition to the gravity data collected in the Ivrea-Verbano zone, I installed and maintained a network of 10 broadband seismic stations (*IvreaArray*, https://doi.org/10.5281/zenodo.1038209) in collaboration with colleagues from the INGV and the Czech Academy of Sciences. This array operated for 2 years and 3 months, from June 2017 to September 2019. The 10 seismic stations were installed along a West-East linear profile along Val Sesia, at 5 km inter-station spacing, starting few kilometers West of the Insubric Line, and crossing the Ivrea-Verbano zone until the Eastern side of Lago Maggiore, naturally connecting the profile to a permanent station. The main target with such an array was to image the Ivrea Geophysical Body across its presumed strike, and to exploit teleseismic sources from both the eastern and western directions.

I used and processed the new seismic and gravity data to refine and further constrain a 2D cross-section of the IGB along the Val Sesia profile. To do this, I modelled the Ivrea body as a single and common density and shear-wave velocity contrast interface, whose initial geometry was based on the structure of the recent 3D density model. I designed, implemented and ran an algorithm which executes a performance-driven random walk in the model space (i.e., the ensemble of all the possible Ivrea body models), to preferentially explore the better fitting areas of the 9D parameter space defining the model. Processing the collected gravity data together with the new seismic data as migrated P-to-S converted waves lead to new constraints on the IGB structure. A shallow and relatively sharp interface is resolved over at least 20 km horizontal distance in the western part of the seismic profile (between ~ 8.11°E and 8.43°E). The inversion results present two main groups of well-fitting model geometries, presenting different characteristics for the shallowest portion the Ivrea body: a flat and gently eastward-dipping interface between 3 and 7 km depth, and a structure with a local peak reaching as shallow as 1-3 km depth, beneath the three westernmost stations (~ 8.11° E and 8.25°E). While both groups of models agree with a western boundary associated with the steeply westward-dipping Insubric Line, the latter is more consistent with the well-known lower crustal rock complex outcropping at the western edge of the Ivrea-Verbano Zone. Further agreement with the observed geological structures at the surface is found by comparing the IGB model structure with the location of the Pogallo Fault Zone (PFZ), highlighting the role of pre-orogenic processes in shaping the IGB.

The retrieved IGB velocity and density contrasts relative to the surroundings are in general good agreement with the physical properties of the rock samples collected in the area and analysed in earlier studies. The results span a rather broad range of acceptable shear-wave velocity contrasts (0.5 to 1.2 $km \cdot s^{-1}$), providing slightly higher velocities than those from field

samples and/or trends in the literature. In terms of density, a reasonably narrow range of better-fitting density contrasts of 200 to 400 $kg \cdot m^{-3}$ is found, in agreement with the results from the earlier 3D Ivrea body modelling, which favoured a density contrast of 400 $kg \cdot m^{-3}$, and also in agreement with earlier gravity studies in the literature.

I further analysed the amplitude and the frequency content of a stack of high-quality P-to-S converted waves (receiver functions), to constrain the sharpness of the vertical velocity-gradient associated with the shallow IGB discontinuity. By comparing the stack with synthetics for different maximum frequency contents, I found thicknesses of 0.8 km to 0.4 km as reasonable higher and lower limits for the shallow velocity-gradient associated with the top of the Ivrea body discontinuity near its shallower structural position.

Further work on the Ivrea body structure and its physical properties is foreseen in the future. The collected seismic data will be processed with ambient noise tomography techniques to address the local shear-wave seismic velocity structure from a complementary perspective with respect to what is seen by receiver functions, and further seismic analysis may provide information on the anisotropic features of the Ivrea body, even though they could not be resolved via receiver function analysis. The obtained results will be also complemented and compared to the results of recent active seismic campaigns, which were carried out in Val Sesia in the framework of the continental drilling project DIVE: Drilling the Ivrea-Verbano zonE (Pistone et al., 2017), aiming at investigating the physics, the chemistry and the evolution of the very exposed outcrops in the Ivrea-Verbano Zone and the structures just beneath.

The third main part of my thesis was carried out in a different zone and context of the Alps, yet it also focused on further advancements in the geophysical investigation of km-scale crustal structures. The theme was a gravity investigation along the Gotthard Base Tunnel, currently the longest tunnel on Earth, along which I collected 80 new relative gravity data points at the surface and processed them together with 77 existing gravity data points measured in the tunnel. This work was carried out with support of the SGPK (Swiss Geophysical Commission) and in collaboration with swisstopo (Swiss Federal Office of Topography), and aimed to test the tunnel's shallow crustal geological model where Nettleton's approach would not work properly. For this purpose, I developed a novel, iterative processing scheme, which computes fully 3D, density-dependent gravity terrain corrections, to then constrain and analyse a 2D geological model structure converted into a density model. In this approach, I compute the gravity effect of a number of prescribed units with fixed geometry and unit density, and then I linearly scale their gravity effect based on a variety of tested density values. This approach reduces drastically the computation time arising from terrain correction calculations, and it thus allows to fully explore and quantify the rock density distribution along the model. This approach allowed to compare our gravity observations with assigned lithological structures for the Gotthard Base Tunnel area and to test different density profiles, ranging from reasonable end-member models to regional averages and local samples provided by the SAPHYR catalog. Results indicate that the locally sampled densities provide a better fit to the data for the considered lithologies, rather than density data averaged over a wider set of Alpine rock samples for the same lithology. Furthermore, using one homogeneous and constant density value for all the topographic corrections does not provide an optimal fit to the data, which instead

favours different density contrasts along the profile. The gravity data processing routines and the density-dependent corrections I developed for this application can be implemented into a systematic inversion scheme and, in addition to this, they represent a remarkable potential for further high-resolution intra-crustal gravity investigations in other areas. For example, in the area of the Balmuccia peridotite body in the Ivrea-Verbano Zone, for which I participated in the data collection campaign in Spring 2021 acquiring 83 new relative gravity data points.

In conclusion, the three studies I presented targeted an optimal natural laboratory for testing the higher end of resolution limits of passive seismic and gravity investigations. The obtained results provided new information on Earth subsurface structures at intra-crustal spatial scales, complementing and better linking both the earlier existing passive geophysical investigations and geological studies, and also the usually more expensive active ones. This was achieved in areas – both in the case of the Ivrea Geophysical Body and the Gotthard Base Tunnel – where the crust predominantly exposes vertical to sub-vertical structures at the surface and near subsurface, which constitutes a challenge for most if not all the geophysical imaging methods. Finally, combining these geophysical investigations with data from surface geological observations and rock sample laboratory analyses, at different stages ranging from modelling to results interpretation, was a fundamental step for providing new, solid information on the Earth subsurface and for reducing the earlier existing resolution gaps.
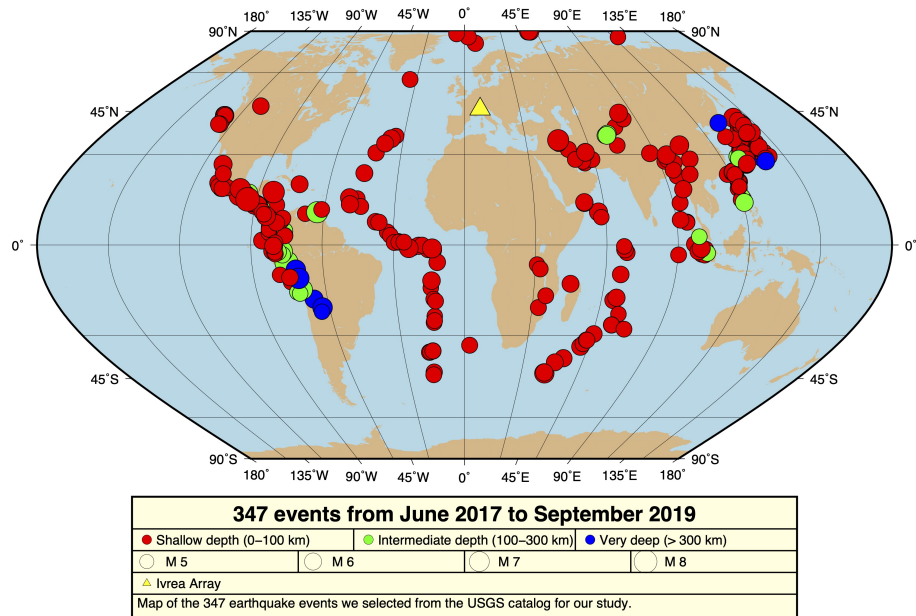
A Appendix

Figure A.1 – World map showing the 347 earthquakes selected for this study and used for the computation of seismic RFs. The events were selected according to the following criteria: minumum magnitude 5.4; minumum and maximum epicentral distances from the IvreaArray location (yellow triangle) 28° and 95°, respectively.
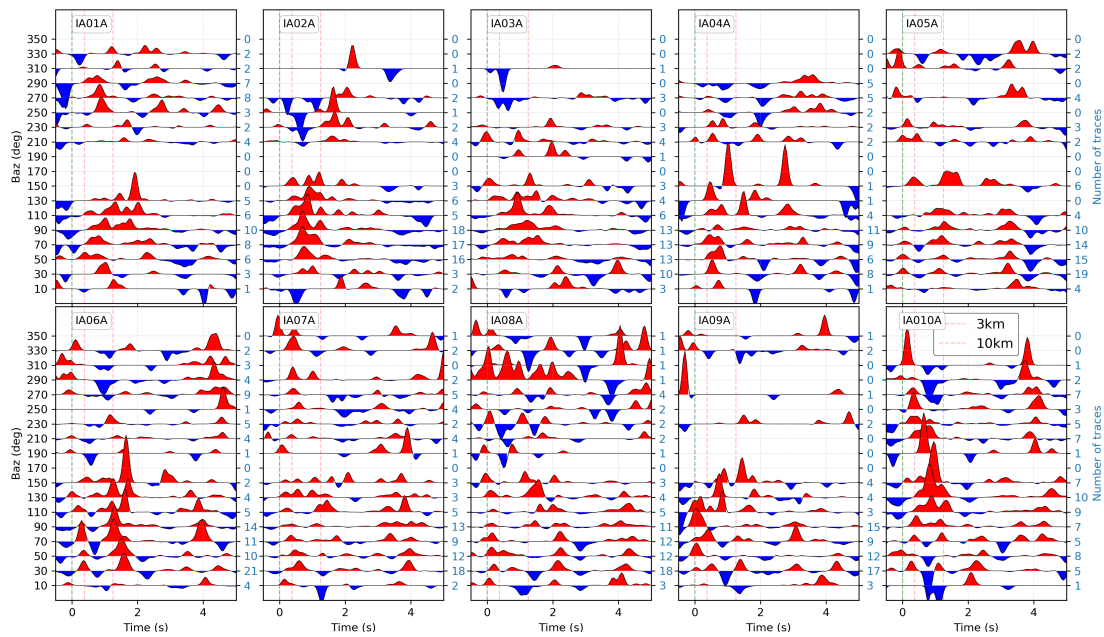
Figure A.2 – Complete RFs database (radial component) stacked by back-azimuthal direction bins for every single IvreaArray station. The dashed green line indicates the expected location of the direct P-wave signal, which act as a reference time for the RFs converted phases and is assigned at 0 s by construction. The dashed red lines indicate the expected delay time for the converted phases, produced by interfaces at 3 and 10 km depth respectively for a standard (iasp91) crustal structure, to focus on the delay time window of interest for shallow interfaces.
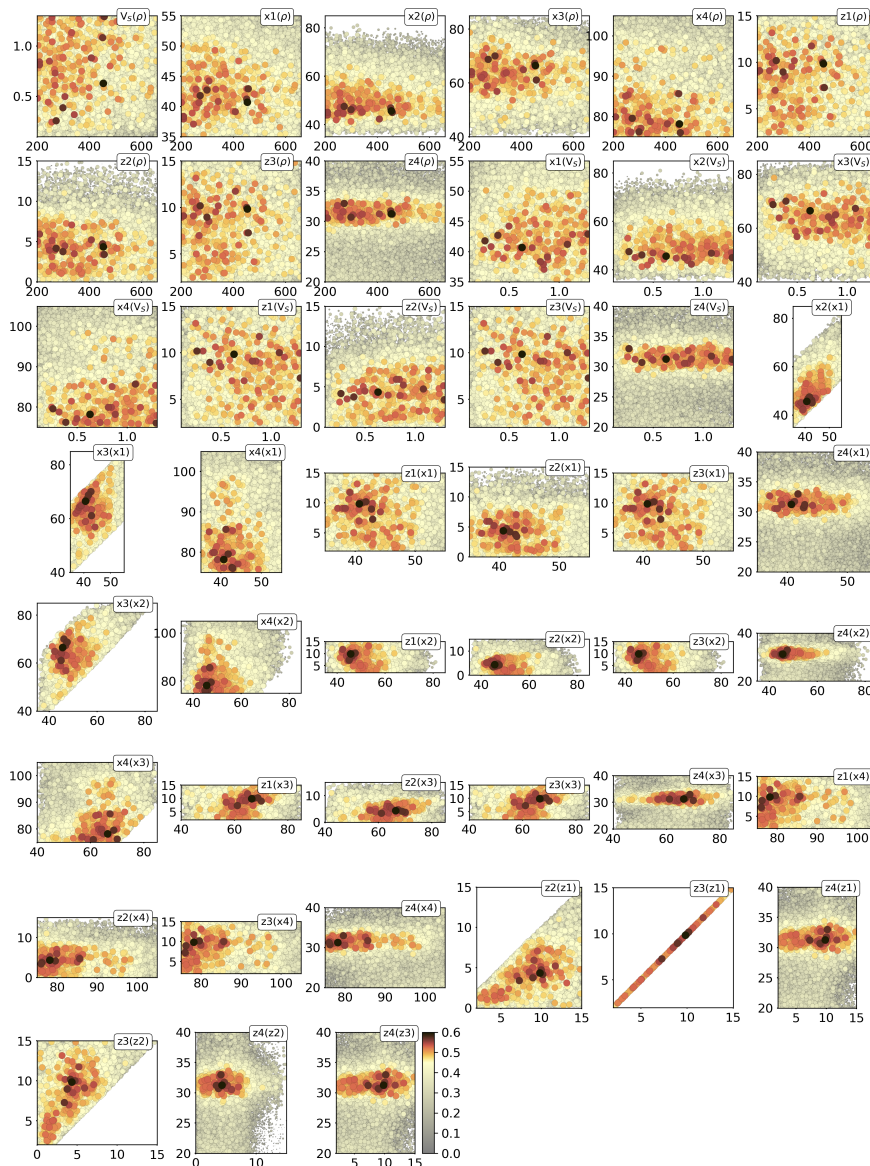
Figure A.3 – Inversion results representing the model performance for every pair of variables, labelled y(x) on the panels. All sampled and kept models are shown (in total 41'363). Each model is shown by a circle with size and colour according to the performance (colour bar on the bottom row). Each panel is scaled to the allowed range of parameter values. The coordinates of the geometry nodes are expressed in km, the velocity contrast in km/s and the density contrast in $kg \cdot m^{-3}$. The values of z3 and z1 are equal by construction.

Figure A.4 – Distribution of the model performances for all the sampled and kept models. The single seismic and gravity model performances are shown (green and blue lines respectively), together with the distribution of the final model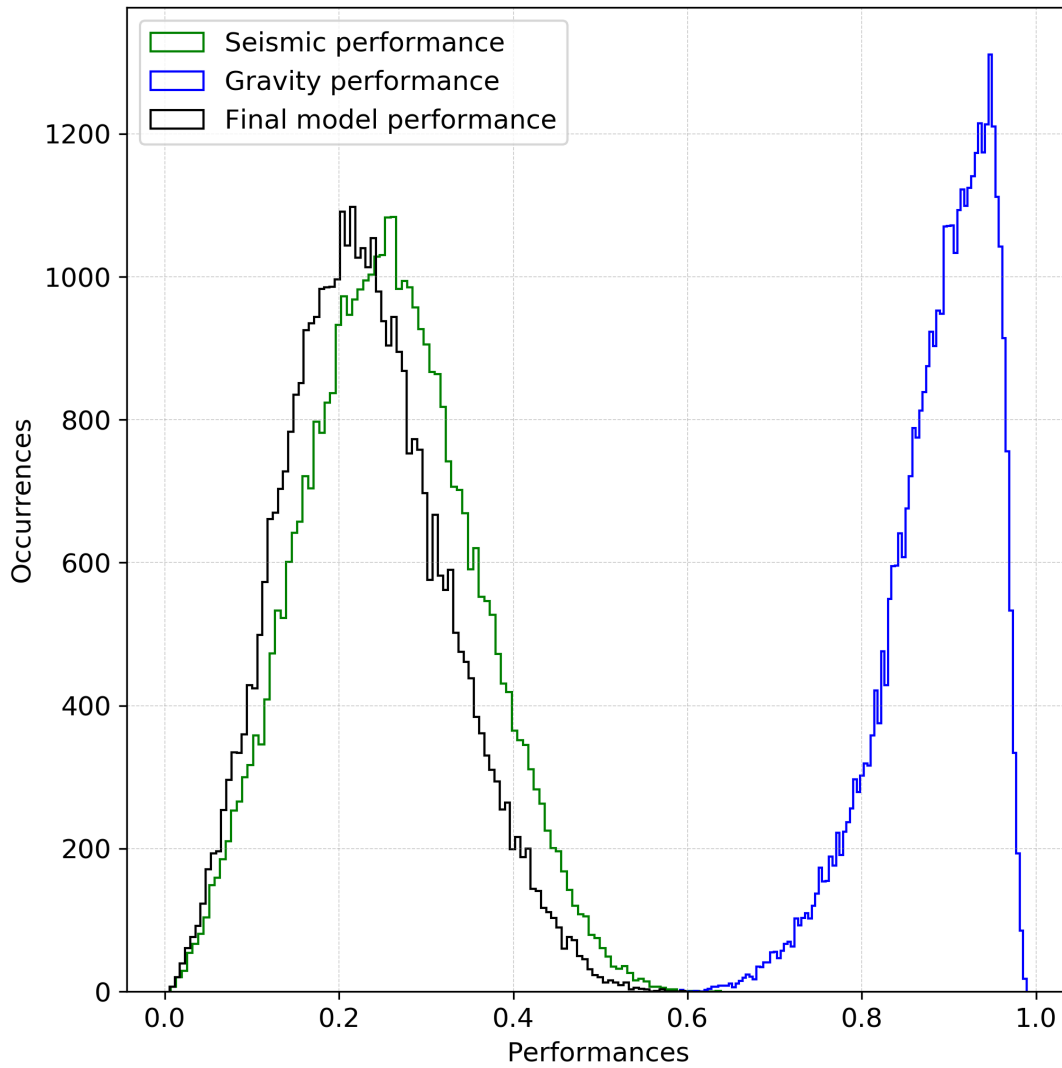 performances (black line). The final model performance is defined as the direct multiplication of the seismic and gravity ones.
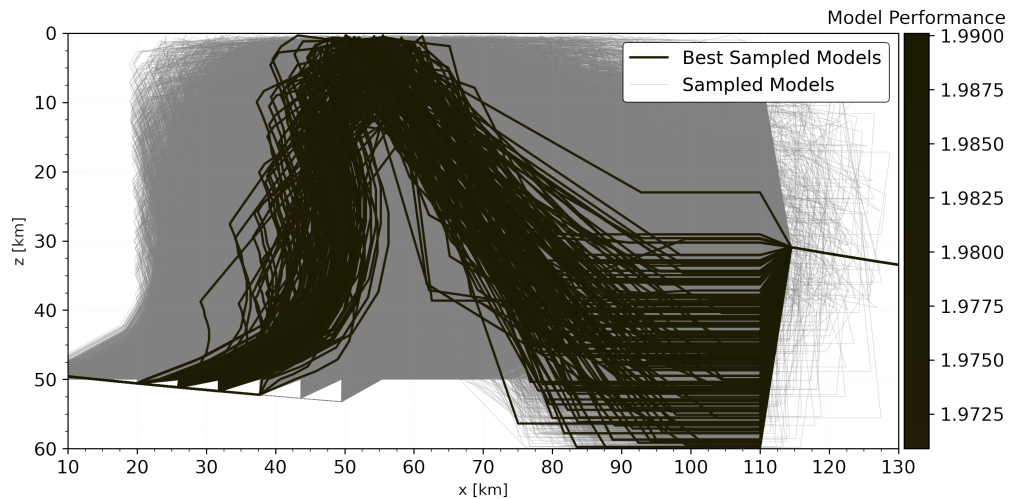
Figure A.5 – Model geometries resulting from a gravity-only inversion, using looser geometrical constraints: i.e. with a wider model space and a wider range of allowed model geometries. The 150 best performing models are shown in black, all the other sampled models in grey in the background. We shifted the gravity model performance by 1, so that 1 + Lg(m) is normalised between 0 and 2. In the joint inversion presented in the manuscript, the generally higher gravity performances stem from the fact that the starting model – and the extent of the explorable model space (based on the available a priori constraints) are defined on an already wellfitting 3D gravity model (Scarponi et al., 2020). In this case, with looser geometrical constraints, the gravity performance distribution shows bad-performing gravity models as well (ranging from ca. 1.99 to ca. 1.2), some of which were not included in the joint inversion because of the available a priori information (see manuscript). Gravity-alone points to a shallow anomalous structure as well. Nevertheless, joint inversion with seismic data is required to constrain the depth of node 4.
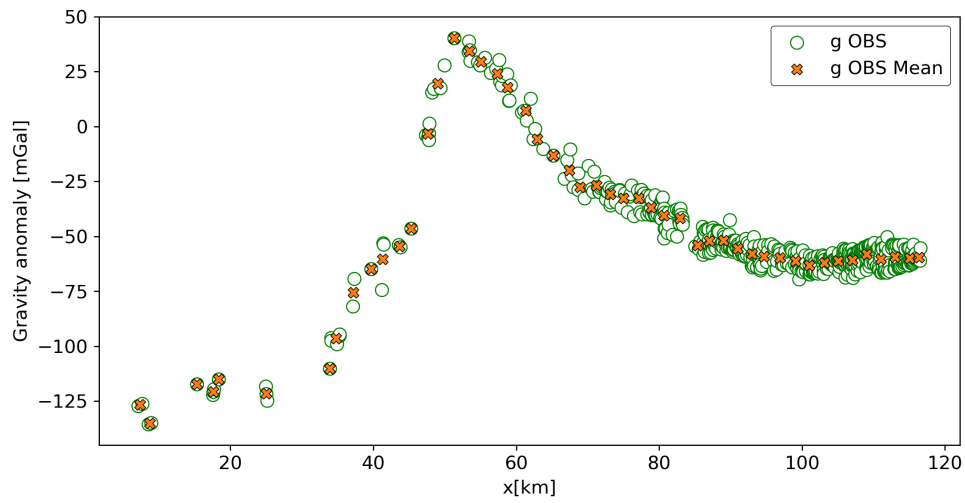
Figure A.6 – Compiled gravity anomaly observations along the seismic profile (green circles) versus the binned averaged gravity data points (orange crosses). To obtain the mean gravity dataset (orange crosses), we divided the full dataset into 2-km wide bins along the profile, and averaged the observed gravity values within each bin. The standard deviation of the original gravity data for its respective average is less than 10 mGal in any bin, with 3mGal mean and 3.3mGal median along the whole profile. The gravity data binning was done for two reasons: (1) to speed up the computation time for the gravity data modelling (0.08s instead of 1s for each model) and mainly (2) to have a more balanced weight of the gravity data along the profile.

Bibliography

Agius, M., Rychert, C. A., Harmon, N., and Laske, G. (2017). Mapping the mantle transition zone beneath hawaii from Ps receiver functions: Evidence for a hot plume and cold mantle downwellings. *Earth and Planetary Science Letters*, 474:226–236.

Ammon, C., Randall, G. E., and Zandt, G. (1990). On the nonuniqueness of receiver function inversions. *Journal of Geophysical Research: Solid Earth*, 95(B10):15303–15318.

Ansorge, J. et al. (1979). Crustal section across the zone of Ivrea-Verbano from the Valais to the Lago Maggiore.

Aoki, I. and Takahashi, E. (2004). Density of MORB eclogite in the upper mantle. *Physics of the Earth and Planetary Interiors*, 143:129–143.

Autin, J., Scheck-Wenderoth, M., Götze, H., Reichert, C., and Marchal, D. (2016). Deep structure of the Argentine margin inferred from 3D gravity and temperature modelling, Colorado Basin. *Tectonophysics*, 676:198–210.

Basuyau, C. and Tiberi, C. (2011). Imaging lithospheric interfaces and 3D structures using receiver functions, gravity, and tomography in a common inversion scheme. *Computers & geosciences*, 37(9):1381–1390.

Bauville, A. and Baumann, T. S. (2019). geomio: an open-source MATLAB toolbox to create the initial configuration of 2-D/3-D thermo-mechanical simulations from 2-D vector drawings. *Geochemistry, Geophysics, Geosystems*, 20(3):1665–1675.

Bayer, R., Carozzo, M., Lanza, R., Miletto, M., Rey, D., and Group, T. E.-C. G. (1989). Gravity modelling along the ECORS-CROP vertical seismic reflection profile through the Western Alps. *Tectonophysics*, 162(3-4):203–218.

Berckhemer, H. (1968). Topographie des "Ivrea-Körpers" abgeleitet aus seismischen und gravimetrischen Daten. *Schweiz. Mineral. Petrogr. Mitt*, 48(1):235–246.

Berger, A., Mercolli, I., Kapferer, N., and Fügenschuh, B. (2012). Single and double exhumation of fault blocks in the internal Sesia-Lanzo Zone and the Ivrea-verbano Zone (Biella, Italy). *International Journal of Earth Sciences*, 101(7):1877–1894.

Bibliography

Bigi, G. (1983). *Structural Model of Italy and Gravity Maps.* CNR.

Bodin, T., Sambridge, M., Tkalčić, H., Arroucau, P., Gallagher, K., and Rawlinson, N. (2012). Transdimensional inversion of receiver functions and surface wave dispersion. *Journal of Geophysical Research: Solid Earth*, 117(B2).

Bois, C., Pinet, B., and Roure, F. (1989). Dating lower crustal features in France and adjacent areas from deep seismic profiles. *Properties and processes of Earth's lower crust*, 51:17–31.

Boriani, A. et al. (1971). Geology of the junction between the Ivrea-Verbano and Strona-Ceneri Zones (Southern Alps). *Memorie dell'Istituto Geologico della R. Università di Padova*, 28:1–35.

Bousquet, R., Oberhansli, R., Schmid, S., Berger, A., Wiederkeher, M., Robert, C., Moller, A., Rosenberg, C., Zeilinger, G., Molli, G., et al. (2012). *Metamorphic framework of the Alps-Carte metamorphique des Alpes CCGM/CGMW.* CCGM/CGMW.

Brack, P., Ulmer, P., and Schmid, S. M. (2010). A crustal-scale magmatic system from the Earth's mantle to the Permian surface: Field trip to the area of lower valsesia and val d'ossola (massiccio dei laghi, southern alps, northern italy). *Swiss Bulletin für angewandte Geologie*, 15(2):3–21.

Brocher, T. (2005). Empirical relations between elastic wavespeeds and density in the Earth's crust. *Bulletin of the seismological Society of America*, 95(6):2081–2092.

Bürki, B. (1990). Geophysical interpretation of astrogravimetric data in the Ivrea Zone. In *Exposed Cross-Sections of the Continental Crust*, pages 545–561. Springer.

Cattin, R., Mazzotti, S., and Baratin, L.-M. (2015). GravProcess: An easy-to-use MATLAB software to process campaign gravity data and evaluate the associated uncertainties. *Computers & geosciences*, 81:20–27.

Ceriani, S., Fügenschuh, B., and Schmid, S. (2001). Multi-stage thrusting at the "Penninic Front" in the Western Alps between Mont Blanc and Pelvoux massifs. *International Journal of Earth Sciences*, 90(3):685–702.

Clayton, R. and Wiggins, R. (1976). Source shape estimation and deconvolution of teleseismic bodywaves. *Geophysical Journal International*, 47(1):151–177.

Corchete, V. (2010). The high-resolution gravimetric geoid of Italy: ITG2009. *Journal of African earth sciences*, 58(3):580–584.

Crameri, F. (2018). Scientific colour-maps. *Zenodo.* doi:10.5281/zenodo.4491293.

De Franco, R., Biella, G., Boniolo, G., Corsi, A., Demartin, M., Maistrello, M., and Morrone, A. (1997). Ivrea seismic array: a study of continental crust and upper mantle. *Geophysical Journal International*, 128(3):723–736.

Diehl, T., Husen, S., Kissling, E., and Deichmann, N. (2009). High-resolution 3-D P-wave model of the Alpine crust. *Geophysical Journal International*, 179(2):1133–1147.

Drahos, D. (2008). Determining the objective function for geophysical joint inversion. *Geophysical Transactions*, 45(3):105–121.

Druet, M., Muñoz-Martín, A., Granja-Bruña, J. L., Carbó-Gorosabel, A., Acosta, J., Llanes, P., and Ercilla, G. (2018). Crustal structure and continent-ocean boundary along the Galicia continental margin (NW Iberia): insights from combined gravity and seismic interpretation. *Tectonics*, 37(5):1576–1604.

Farr, T., Rosen, P. A., Caro, E., Crippen, R., Duren, R., Hensley, S., Kobrick, M., Paller, M., Rodriguez, E., Roth, L., et al. (2007). The shuttle radar topography mission. *Reviews of geophysics*, 45(2).

Fountain, D. (1976). The Ivrea—Verbano and Strona-Ceneri Zones, Northern Italy: a cross-section of the continental crust—new evidence from seismic velocities of rock samples. *Tectonophysics*, 33(1-2):145–165.

Fountain, D. (1989). Growth and modification of lower continental crust in extended terrains: the role of extension and magmatic underplating. *Properties and processes of Earth's lower crust*, 51:287–299.

Fountain, D. M., Percival, J., and Salisbury, M. H. (1990). Exposed cross sections of the continental crust-synopsis. In *Exposed cross-sections of the continental crust*, pages 653–662. Springer.

Frederiksen, A. and Bostock, M. (2000). Modelling teleseismic waves in dipping anisotropic structures. *Geophysical Journal International*, 141(2):401–412.

Fukao, Y., Yamamoto, A., and Nozaki, K. (1981). A method of density determination for gravity correction. *Journal of Physics of the Earth*, 29(2):163–166.

Greenwood, A., Baron, L., Merz, K., Petri, B., Orsolya Kard, A., Zanetti, A., Pistone, M., Hetényi, G., Weber, M., Müntener, O., et al. (2018). High-resolution active seismic survey across the Insubric Line. In *EGU General Assembly Conference Abstracts*, volume 19564.

Guntli, P., Keller, F., Lucchini, R., and Rust, P. (2016). Gotthard-Basistunnel. Geologie – Geotechnik – Hydrogeologie. Zusammenfassender Schlussbericht. Ber. Landesgeol. 7.

Gurrola, H., Baker, G. E., and Minster, J. B. (1995). Simultaneous time-domain deconvolution with application to the computation of receiver functions. *Geophysical Journal International*, 120(3):537–543.

Götze, H. and Lahmeyer, B. (1988). Application of three-dimensional interactive modeling in gravity and magnetics. *Geophysics*, 53(8):1096–1108.

Bibliography

Hacker, B., Kelemen, P. B., and Behn, M. D. (2015). Continental lower crust. *Annual Review of Earth and Planetary Sciences*, 43:167–205.

Handy (1987). The structure, age and kinematics of the Pogallo Fault Zone; Southern Alps, northwestern Italy. *Eclogae Geologicae Helvetiae*, 80(3):593–632.

Handy, Franz, L., Heller, F., Janott, B., and Zurbriggen, R. (1999). Multistage accretion and exhumation of the continental crust (Ivrea crustal section, Italy and Switzerland). *Tectonics*, 18(6):1154–1177.

Handy, Schmid, S. M., Bousquet, R., Kissling, E., and Bernoulli, D. (2010). Reconciling plate-tectonic reconstructions of Alpine Tethys with the geological–geophysical record of spreading and subduction in the Alps. *Earth-Science Reviews*, 102(3-4):121–158.

Handy, Ustaszewski, K., and Kissling, E. (2015). Reconstructing the Alps–Carpathians–Dinarides as a key to understanding switches in subduction polarity, slab gaps and surface motion. *International Journal of Earth Sciences*, 104(1):1–26.

Hetényi, G., Plomerová, J., Bianchi, I., Exnerová, H. K., Bokelmann, G., Handy, M. R., Babuška, V., Group, A.-E. W., et al. (2018). From mountain summits to roots: Crustal structure of the Eastern Alps and Bohemian Massif along longitude 13.3 E. *Tectonophysics*, 744:239–255.

Hetényi, G. (2007). *Evolution of deformation of the Himalayan prism: from imaging to modelling*. PhD thesis, École Normale Supérieure–Université Paris-Sud XI.

Hetényi, G., Cattin, R., Brunet, F., Bollinger, L., Vergne, J., Nábêlek, J. L., and Diament, M. (2007). Density distribution of the India plate beneath the Tibetan plateau: Geophysical and petrological constraints on the kinetics of lower-crustal eclogitization. *Earth and Planetary Science Letters*, 264(1-2):226–244.

Hetényi, G., Molinari, I., Clinton, J., Bokelmann, G., Bondár, I., Crawford, W. C., Dessa, J.-X., Doubre, C., Friederich, W., Fuchs, F., et al. (2018). The Alparray seismic network: a large-scale European experiment to image the Alpine orogen. *Surveys in geophysics*, 39(5):1009–1033.

Hetényi, G., Plomerová, J., Solarino, S., Scarponi, M., Vecsey, L., Munzarová, H., Babuška, V., Jedlička, P., Kotek, J., and Colavitti, L. (2017). IvreaArray - an AlpArray Complementary Experiment. doi:10.5281/zenodo.1038209.

Hetényi, G., Ren, Y., Dando, B., Stuart, G. W., Hegedűs, E., Kovács, A. C., and Houseman, G. A. (2015). Crustal structure of the Pannonian basin: the AlCaPa and Tisza Terrains and the Mid-Hungarian zone. *Tectonophysics*, 646:106–116.

Hinze, W. (2003). Bouguer reduction density, why 2.67? *Geophysics*, 68(5):1559–1560.

Holliger, K., Levander, A., Carbonell, R., and Hobbs, R. (1994). Some attributes of wavefields scattered from Ivrea-type lower crust. *Tectonophysics*, 232(1-4):267–279.

Holliger, K., Levander, A. R., and Goff, J. A. (1993). Stochastic modeling of the reflective lower crust: Petrophysical and geological evidence from the Ivrea Zone (northern Italy). *Journal of Geophysical Research: Solid Earth*, 98(B7):11967–11980.

Hubbert, M. (1948). A line-integral method of computing the gravimetric effects of two-dimensional masses. *Geophysics*, 13(2):215–225.

James, D., Niu, F., and Rokosky, J. (2003). Crustal structure of the Kaapvaal craton and its significance for early crustal evolution. *Lithos*, 71(2-4):413–429.

Julia, J., Ammon, C., Herrmann, R., and Correig, A. M. (2000). Joint inversion of receiver function and surface wave dispersion observations. *Geophysical Journal International*, 143(1):99–112.

Karakas, O., Wotzlaw, J.-F., Guillong, M., Ulmer, P., Brack, P., Economos, R., Bergantz, G. W., Sinigoi, S., and Bachmann, O. (2019). The pace of crustal-scale magma accretion and differentiation beneath silicic caldera volcanoes. *Geology*, 47(8):719–723.

Kennett, B. and Engdahl, E. (1991). Traveltimes for global earthquake location and phase identification. *Geophysical Journal International*, 105(2):429–465.

Khazanehdari, J., Rutter, E., and Brodie, K. (2000). High-pressure-high-temperature seismic velocity structure of the midcrustal and lower crustal rocks of the Ivrea-Verbano zone and Serie dei Laghi, NW Italy. *Journal of Geophysical Research: Solid Earth*, 105(B6):13843–13858.

Kissling, E. (1993). Deep structure of the Alps—what do we really know? *Physics of the Earth and Planetary Interiors*, 79(1-2):87–112.

Kissling, E., Schmid, S. M., Lippitsch, R., Ansorge, J., and Fügenschuh, B. (2006). Lithosphere structure and tectonic evolution of the Alpine arc: new evidence from high-resolution teleseismic tomography. *Geological Society, London, Memoirs*, 32(1):129–145.

Kissling, E., Wagner, J., and Mueller, S. (1984). Three-dimensional gravity model of the northern Ivrea-Verbano Zone. *Wagner, J.-J., St. Müller (Eds.), Geomagnetic and Gravimetric Studies of the Ivrea Zone: Matér. Géol. Suisse. Géophys*, 21:55–61.

Köther, N., Götze, H.-J., Gutknecht, B. D., Jahr, T., Jentzsch, G., Lücke, O., Mahatsente, R., Sharma, R., and Zeumann, S. (2012). The seismically active Andean and Central American margins: Can satellite gravity map lithospheric structures? *Journal of Geodynamics*, 59:207–218.

Langston, C. (1979). Structure under Mount Rainier, Washington, inferred from teleseismic body waves. *Journal of Geophysical Research: Solid Earth*, 84(B9):4749–4762.

Lanza, R. (1982). Models for interpretation of the magnetic anomaly of the Ivrea body. *Geologie Alpine*, 58:85–94.

Bibliography

Le Breton, E., Handy, M. R., Molli, G., and Ustaszewski, K. (2017). Post-20 Ma motion of the Adriatic Plate: New constraints from surrounding orogens and implications for crust-mantle decoupling. *Tectonics*, 36(12):3135–3154.

Levin, V. and Park, J. (1997). Crustal anisotropy in the Ural mountains foredeep from teleseismic receiver functions. *Geophysical Research Letters*, 24(11):1283–1286.

Licciardi, A., Agostinetti, N. P., Lebedev, S., Schaeffer, A., Readman, P., and Horan, C. (2014). Moho depth and Vp/Vs in Ireland from teleseismic receiver functions analysis. *Geophysical Journal International*, 199(1):561–579.

Ligorría, J. and Ammon, C. J. (1999). Iterative deconvolution and receiver-function estimation. *Bulletin of the seismological Society of America*, 89(5):1395–1400.

Lippitsch, R., Kissling, E., and Ansorge, J. (2003). Upper mantle structure beneath the Alpine orogen from high-resolution teleseismic tomography. *Journal of Geophysical Research: Solid Earth*, 108(B8).

Lombardi, D., Braunmiller, J., Kissling, E., and Giardini, D. (2008). Moho depth and Poisson's ratio in the Western-Central Alps from receiver functions. *Geophysical Journal International*, 173(1):249–264.

Lu, Y., Stehly, L., Paul, A., and Group, A. W. (2018). High-resolution surface wave tomography of the European crust and uppermost mantle from ambient seismic noise. *Geophysical Journal International*, 214(2):1136–1150.

Löw, S., Lützenkirchen, V., Hansmann, J., Ryf, A., and Guntli, P. (2015). Transient surface deformations caused by the Gotthard Base Tunnel. *International Journal of Rock Mechanics and Mining Sciences*, 75:82–101.

Manzotti, P., Ballevre, M., Zucali, M., Robyr, M., and Engi, M. (2014). The tectonometamorphic evolution of the Sesia–Dent Blanche nappes (internal Western Alps): review and synthesis. *Swiss Journal of Geosciences*, 107(2):309–336.

Marson, I., Orlando, L., and Stoka, M. (1994). Gravity model on the CROP profile. In *Proceedings of Symposium CROP Alpi centrali. Quaderni di Geodinamica Alpina e Quaternaria*, volume 2, pages 161–169.

Masson, F., Verdun, J., Bayer, R., and Debeglia, N. (1999). Une nouvelle carte gravimétrique des Alpes occidentales et ses conséquences structurales et tectoniques. *Comptes Rendus de l'Académie des Sciences-Series IIA-Earth and Planetary Science*, 329(12):865–871.

Miller, H. (1976). A lithospheric seismic profile along the axis of the Alps, 1975. *Pure and Applied Geophysics*, 114(6):1109–1130.

Moorkamp, M., Jones, A., and Fishwick, S. (2010). Joint inversion of receiver functions, surface wave dispersion, and magnetotelluric data. *Journal of Geophysical Research: Solid Earth*, 115(B4).

Müntener, O. and Ulmer, P. (2006). Experimentally derived high-pressure cumulates from hydrous arc magmas and consequences for the seismic velocity structure of lower arc crust. *Geophysical Research Letters*, 33(21). doi:10.1029/2006GL027629.

Nábělek, J., Hetényi, G., Vergne, J., Sapkota, S., Kafle, B., Jiang, M., Su, H., Chen, J., Huang, B.-S., et al. (2009). Underplating in the Himalaya-Tibet collision zone revealed by the Hi-CLIMB experiment. *Science*, 325(5946):1371–1374.

Nettleton, L. (1939). Determination of density for reduction of gravimeter observations. *Geophysics*, 4(3):176–183.

Nettleton, L. (1976). *Gravity and magnetics in oil prospecting*. McGraw-Hill Companies.

Nicolas, A., Hirn, A., Nicolich, R., and Polino, R. (1990). Lithospheric wedging in the western Alps inferred from the ECORS-CROP traverse. *Geology*, 18(7):587–590.

Niggli, E. (1946). *Über den Zusammenhang zwischen der positiven Schwereanomalie am Südfuß der Westalpen und der Gesteinszone von Ivrea*.

Oldenburg, D. (1981). A comprehensive solution to the linear deconvolution problem. *Geophysical Journal International*, 65(2):331–357.

Parasnis, D. (1952). A study of rock densities in the English Midlands. *Geophysical Supplements to the Monthly Notices of the Royal Astronomical Society*, 6(5):252–271.

Petri, B., Duretz, T., Mohn, G., Schmalholz, S. M., Karner, G. D., and Müntener, O. (2019). Thinning mechanisms of heterogeneous continental lithosphere. *Earth and Planetary Science Letters*, 512:147–162.

Petri, B., Mohn, G., Skrzypek, E., Mateeva, T., Galster, F., and Manatschal, G. (2017). U–Pb geochronology of the sondalo gabbroic complex (Central Alps) and its position within the Permian post-Variscan extension. *International Journal of Earth Sciences*, 106(8):2873–2893.

Piana Agostinetti, N. and Amato, A. (2009). Moho depth and Vp/Vs ratio in peninsular Italy from teleseismic receiver functions. *Journal of Geophysical Research: Solid Earth*, 114(B6).

Piromallo, C. and Faccenna, C. (2004). How deep can we find the traces of Alpine subduction? *Geophysical Research Letters*, 31(6).

Pistone, M., Müntener, O., Ziberna, L., Hetényi, G., and Zanetti, A. (2017). Report on the ICDP workshop DIVE (Drilling the Ivrea–Verbano zonE). *Scientific Drilling*, 23:47–56.

Pistone, M., Ziberna, L., Hetényi, G., Scarponi, M., Zanetti, A., and Müntener, O. (2020). Joint Geophysical-Petrological Modeling on the Ivrea Geophysical Body Beneath Valsesia, Italy: Constraints on the Continental Lower Crust. *Geochemistry, Geophysics, Geosystems*, 21(12):e2020GC009397.

Quick, J. and Denlinger, R. P. (1993). Ductile deformation and the origin of layered gabbro in ophiolites. *Journal of Geophysical Research: Solid Earth*, 98(B8):14015–14027.

Quick, J., Sinigoi, S., and Mayer, A. (1994). Emplacement dynamics of a large mafic intrusion in the lower crust, Ivrea-Verbano Zone, northern Italy. *Journal of Geophysical Research: Solid Earth*, 99(B11):21559–21573.

Quick, J., Sinigoi, S., and Mayer, A. (1995). Emplacement of mantle peridotite in the lower continental crust, Ivrea-Verbano zone, northwest Italy. *Geology*, 23(8):739–742.

Quick, J., Sinigoi, S., Peressini, G., Demarchi, G., Wooden, J., and Sbisà, A. (2009). Magmatic plumbing of a large permian caldera exposed to a depth of 25 km. *Geology*, 37(7):603–606.

Quick, J., Sinigoi, S., Snoke, A. W., Kalakay, T. J., Mayer, A., and Peressini, G. (2003). Geologic map of the southern Ivrea-Verbano Zone, northwestern Italy. *US Geological Survey*.

Rawlinson, N., Pozgay, S., and Fishwick, S. (2010). Seismic tomography: a window into deep Earth. *Physics of the Earth and Planetary Interiors*, 178(3-4):101–135.

Rey, Quarta, T., Mouge, P., Miletto, M., and Lanza, R. (1990). Gravity and aeromagnetic maps of the western alps: contribution to the knowledge of the deep structures along the ECORS-CROP seismic profile. *Mémoires de la Société géologique de France (1833)*, 156:107–121.

Rey, P. (1993). Seismic and tectono-metamorphic characters of the lower continental crust in Phanerozoic areas: A consequence of post-thickening extension. *Tectonics*, 12(2):580–590.

Rivalenti, G., Mazzucchelli, M., Vannucci, R., Hofmann, A. W., Ottolini, L., Bottazzi, P., and Obermiller, W. (1995). The relationship between websterite and peridotite in the balmuccia peridotite massif (NW Italy) as revealed by trace element variations in clinopyroxene. *Contributions to Mineralogy and Petrology*, 121(3):275–288.

Sambridge, M. (1999). Geophysical inversion with a neighbourhood algorithm—I. searching a parameter space. *Geophysical journal international*, 138(2):479–494.

Sambridge, M. and Mosegaard, K. (2002). Monte Carlo methods in geophysical inverse problems. *Reviews of Geophysics*, 40(3):3–1.

Scarponi, M., Hetényi, G., Berthet, T., Baron, L., Manzotti, P., Petri, B., Pistone, M., and Müntener, O. (2020). New gravity data and 3-D density model constraints on the Ivrea Geophysical Body (Western Alps). *Geophysical Journal International*, 222(3):1977–1991.

Schmid, S., Aebli, H., Heller, F., and Zingg, A. (1989). The role of the Periadriatic Line in the tectonic evolution of the Alps. *Geological Society, London, Special Publications*, 45(1):153–171.

Schmid, S., Bernoulli, D., Fügenschuh, B., Matenco, L., Schefer, S., Schuster, R., Tischler, M., and Ustaszewski, K. (2008). The Alpine-Carpathian-Dinaridic orogenic system: correlation and evolution of tectonic units. *Swiss Journal of Geosciences*, 101(1):139–183.

Schmid, S., Fügenschuh, B., Kissling, E., and Schuster, R. (2004). Tectonic map and overall architecture of the alpine orogen. *Eclogae Geologicae Helvetiae*, 97(1):93–117.

Schmid, S. and Kissling, E. (2000). The arc of the western Alps in the light of geophysical data on deep crustal structure. *Tectonics*, 19(1):62–85.

Schmid, S., Kissling, E., Diehl, T., van Hinsbergen, D. J., and Molli, G. (2017). Ivrea mantle wedge, arc of the Western Alps, and kinematic evolution of the Alps–Apennines orogenic system. *Swiss Journal of Geosciences*, 110(2):581–612.

Schmid, S., Pfiffner, O.-A., Froitzheim, N., Schönborn, G., and Kissling, E. (1996). Geophysical-geological transect and tectonic evolution of the Swiss-Italian Alps. *Tectonics*, 15(5):1036–1064.

Schmid, S., Zingg, A., and Handy, M. (1987). The kinematics of movements along the Insubric Line and the emplacement of the Ivrea Zone. *Tectonophysics*, 135(1-3):47–66.

Schmidt, S., Götze, H.-J., Fichler, C., and Alver, M. (2010). IGMAS+ a new 3D Gravity, FTG and Magnetic Modeling Software. In *Geoinformatik*, pages 57–63.

Sheehan, A. F., Abers, G. A., Jones, C. H., and Lerner-Lam, A. L. (1995). Crustal thickness variations across the Colorado Rocky Mountains from teleseismic receiver functions. *Journal of Geophysical Research: Solid Earth*, 100(B10):20391–20404.

Shibutani, T., Sambridge, M., and Kennett, B. (1996). Genetic algorithm inversion for receiver functions with application to crust and uppermost mantle structure beneath eastern Australia. *Geophysical Research Letters*, 23(14):1829–1832.

Siegesmund, S., Layer, P., Dunkl, I., Vollbrecht, A., Steenken, A., Wemmer, K., and Ahrendt, H. (2008). Exhumation and deformation history of the lower crustal section of the Valstrona di Omegna in the Ivrea Zone, southern Alps. *Geological Society, London, Special Publications*, 298(1):45–68.

Sinigoi, S., Quick, J., Demarchi, G., and Klötzli, U. (2011). The role of crustal fertility in the generation of large silicic magmatic systems triggered by intrusion of mantle magma in the deep crust. *Contributions to Mineralogy and Petrology*, 162(4):691–707.

Snoke, A., Kalakay, T. J., Quick, J. E., and Sinigoi, S. (1999). Development of a deep-crustal shear zone in response to syntectonic intrusion of mafic magma into the lower crust, Ivrea–Verbano zone, Italy. *Earth and Planetary Science Letters*, 166(1-2):31–45.

Solarino, S., Malusà, M. G., Eva, E., Guillot, S., Paul, A., Schwartz, S., Zhao, L., Aubert, C., Dumont, T., Pondrelli, S., et al. (2018). Mantle wedge exhumation beneath the Dora-Maira (U) HP dome unravelled by local earthquake tomography (Western Alps). *Lithos*, 296:623–636.

Bibliography

Spada, M., Bianchi, I., Kissling, E., Agostinetti, N. P., and Wiemer, S. (2013). Combining controlled-source seismology and receiver function information to derive 3-D moho topography for Italy. *Geophysical Journal International*, 194(2):1050–1068.

Stampfli, G., Borel, G., Cavazza, W., Mosar, J., and Ziegler, P. (2001). Palaeotectonic and palaeogeographic evolution of the western Tethys and Peritethyan domain (IGCP Project 369). In *Episodes*, page 222.

Subedi, S., Hetényi, G., Vergne, J., Bollinger, L., Lyon-Caen, H., Farra, V., Adhikari, L. B., and Gupta, R. M. (2018). Imaging the Moho and the Main Himalayan Thrust in Western Nepal with receiver functions. *Geophysical Research Letters*, 45(24):13222–13230.

Syracuse, E., Maceira, M., Prieto, G. A., Zhang, H., and Ammon, C. J. (2016). Multiple plates subducting beneath Colombia, as illuminated by seismicity and velocity from the joint inversion of seismic and gravity data. *Earth and Planetary Science Letters*, 444:139–149.

Talwani, M., Worzel, J. L., and Landisman, M. (1959). Rapid gravity computations for two-dimensional bodies with application to the mendocino submarine fracture zone. *Journal of geophysical research*, 64(1):49–59.

Thouvenot, F., Paul, A., Senechal, G., Hirn, A., and Nicolich, R. (1990). ECORS-CROP wide-angle reflection seismics: constraints on deep interfaces beneath the Alps. *Mém. Soc. Géol. France*, 156:97–106.

Tiberti, M., Orlando, L., Di Bucci, D., Bernabini, M., and Parotto, M. (2005). Regional gravity anomaly map and crustal model of the Central–Southern Apennines (Italy). *Journal of Geodynamics*, 40(1):73–91.

Turcotte, D. L. and Schubert, G. (2002). *Geodynamics*. Cambridge university press.

Vecchia, O. (1968). La zone Cuneo-Ivrea-Locarno, élément fondamental des Alpes. Géophysique et géologie. *Schweizerische Mineralogische Petrographische Mitteilungen*, 48:215–226.

Vinnik, L., Reigber, C., Aleshin, I. M., Kosarev, G. L., Kaban, M. K., Oreshin, S. I., and Roecker, S. W. (2004). Receiver function tomography of the central Tien shan. *Earth and Planetary Science Letters*, 225(1-2):131–146.

Won, I. and Bevis, M. (1987). Computing the gravitational and magnetic anomalies due to a polygon: Algorithms and Fortran subroutines. *Geophysics*, 52(2):232–238.

Zahorec, P., Papčo, J., Pašteka, R., Bielik, M., Bonvalot, S., Braitenberg, C., Ebbing, J., Gabriel, G., Gosar, A., Grand, A., Götze, H.-J., Hetényi, G., Holzrichter, N., Kissling, E., Marti, U., Meurers, B., Mrlina, J., Nogová, E., Pastorutti, A., Salaun, C., Scarponi, M., Sebera, J., Seoane, L., Skiba, P., Szűcs, E., and Varga, M. (2021). The first pan-Alpine surface-gravity database, a modern compilation that crosses frontiers. *Earth System Science Data*, 13(5):2165–2209. 10.5194/essd-13-2165-2021.

Zappone, A. and Kissling, E. (2021). SAPHYR: Swiss Atlas of Physical Properties of Rocks: the continental crust in a database. *Swiss Journal of Geosciences*, 114(1):1–27.

Zhu, L. (2000). Crustal structure across the San Andreas Fault, southern California from teleseismic converted waves. *Earth and Planetary Science Letters*, 179(1):183–190.

Zhu, L. and Kanamori, H. (2000). Moho depth variation in southern California from teleseismic receiver functions. *Journal of Geophysical Research: Solid Earth*, 105(B2):2969–2980.

Zingg, A. (1983). The Ivrea and Strona-Ceneri zones (Southern Alps, Ticino and N-Italy)—a review. *Schweizerische mineralogische und petrographische Mitteilungen*, 63(2-3):361–392.

Zingg, A., Handy, M., Hunziker, J., and Schmid, S. (1990). Tectonometamorphic history of the Ivrea Zone and its relationship to the crustal evolution of the Southern Alps. *Tectonophysics*, 182(1-2):169–192.